UNIVERSIDAD AUTÓNOMA DE MADRID
DOCTORAL THESIS

New Nanofabrication Routes to Tailor the Electronic Properties of MoS_2 devices: From Field Effect Transistors to Lateral Homo-structures

Author:

Fernando Jiménez Urbanos

Supervisor:

Dr. Daniel Granados Ruiz

Facultad de Ciencias

Departamento de Física de la Materia Condensada

Madrid, Junio de 2019

Resumen

Desde que se consiguió aislar por primera vez una monocapa de grafeno, hace más de diez años, muchos materiales bidimensionales han aparecido. Todos estos materiales pueden formar una nueva librería que abre paso a la nueva generación tecnológica libre de silicio. Las propiedades de estos materiales (grafeno, dicalcogenuros metálicos de transición, etc.) han sido profundamente estudiadas por una amplia y multidisciplinar rama de la comunidad científica. Dichas propiedades dependen, en gran medida, del número de capas y tamaño del que estén formados.

Muchas aplicaciones podrían surgir si, una vez fabricado un dispositivo, se pudiera modificar, pero desde el punto de vista tecnológico y en procesos de micro o nano-fabricación; una vez que el dispositivo de interés está fabricado es muy difícil y costoso cambiar su estructura o geometría para poder cambiar sus propiedades intrínsecas. Por esto, el tema principal de esta tesis será desarrollar un método que permita cambiar las geometrías de dispositivos que ya estén fabricados de la forma más directa y menos invasiva posible.

Debido a la gran cantidad de materiales presentes, en esta tesis doctoral se ha elegido uno en concreto, debido a sus excelentes propiedades electrónicas y ópticas. Dicho material es el disulfuro de molibdeno, perteneciente a la familia de los dicalcogenuros metálicos de transición. Los dispositivos fabricados poseen una geometría de transistor de efecto campo y se realizan mediante fotolitografía de alto rendimiento. El desarrollo de todos los procesos de fabricación es el primer resultado de esta tesis y que en gran medida; ha permitido la producción de dispositivos de alta calidad.

Una vez optimizada la fabricación de los dispositivos, se empezó a explorar los posibles métodos para poder cambiar las geometrías y, por tanto, intentar cambiar las propiedades de dichos dispositivos ya fabricados. Para ello se utilizó una técnica que combina un haz de electrones focalizado y pulsado con un gas reactivo (en nuestro caso XeF_2). El segundo resultado de esta tesis es el estudio de esta técnica y la formación de nuevas estructuras con ella. Como principal resultado, se obtuvieron nuevos dispositivos donde el dopaje original sufría un cambio de tipo N a P mediado, posiblemente, por un proceso de vacantes de azufre. Este cambio en el dopaje se corroboró con distintas técnicas de caracterización como: micro-Raman, micro-fotoluminiscencia y medidas eléctricas.

Posteriormente se aprovechó el cambio en dopaje de la parte atacada para fabricar homo-uniones laterales de tipo NP. Esta fabricación forma parte de la tercera parte de la tesis doctoral. La caracterización de estos dispositivos NP revelan un comportamiento de diodo, con una fuerte foto-respuesta a la luz.

Abstract

Since the first isolation of a graphene monolayer ten years ago, many bidimensional materials have appeared. These materials can form a new library as an alternative to silicon electronics. The properties of the materials (graphene, transition metal dichalcogenides, etc.) have been studied by a large and multidisciplinary branch of the scientific community. These properties strongly depend on the number of layers and thickness present in the material under study.

Once a device is fabricated, a lot of different properties can emerge if it will be tailored. But from a technological point of view, it is quite difficult and expensive to modify the structure or geometry of the device to alter its intrinsic properties. For that reason, the main topic of this thesis would be the development of a method that allows to tailor the geometries of fabricated devices in a directly and non-aggressive way.

Due to the variety of materials present in the nature, this thesis will only focus in one type. This material is molybdenum disulfide, which belongs to the family of transition metal dichalcogenides and shows outstanding electrical and optical properties. The devices have a field effect transistor geometry and are fabricated with maskless optical lithography. The development of all the fabrication processes is the first result of this thesis allowing the production of high quality devices.

Once the device fabrication has been optimized, new methods to modify device's geometries were explored. For that purpose, a new technique was developed using a pulsed focused electron beam combined with an etchant gas (in our case XeF_2) The second result of this thesis is the study of this technique and the formation of new structures. As main result, new devices were obtained with a change in the doping going from N type to P type. This change in the doping is

mediated by a sulfur vacancy process when the etching was done. This doping change was corroborated using different characterization techniques as: micro-Raman, micro-Photoluminescence and electric measurements.

After that, NP lateral homo-junctions were fabricated taking advantage of the doping change. This fabrication corresponds with the third part of this thesis. The characterization of the NP lateral homo-junctions reveals a diode type behavior with a strong photoresponse under light illumination, and an improvement in the photoresponsivity.

Agradecimientos

En primer lugar quiero dar las gracias a mis padres, por darme ánimos en todo momento. Me habéis dado todo lo que estaba en vuestras manos. Ha habido situaciones difíciles, pero siempre habéis estado ahí para apoyarme en mis decisiones. Me enseñasteis lo que es constancia y trabajo y que, con esfuerzo, todo se puede alcanzar.

También me gustaría dedicarle especial atención a mi compañera de viaje, a Jessica. Sin ti nada de esto hubiera sido posible. Has aguantado mis frustraciones, mis cabreos, mis malos días… ¿Qué puedo decirte? Sólo puedo darte las gracias por estar ahí en todos esos días. También ha habido momentos espectaculares a tu lado: risas, viajes, paseos, cenas e innumerables alegrías. Este viaje que nos espera juntos no ha hecho nada más que comenzar. Después de esta tesis nos quedan muchas cosas por vivir y disfrutar juntos.

Profesionalmente me gustaría agradecer en primer lugar a Amadeo. Gracias por fijarte en ese chaval de segundo de carrera y haberle dado la oportunidad de estar en IMDEA. A Daniel Granados, mi director de tesis. Me has dado una gran oportunidad que, sin duda alguna, he disfrutado de manera colosal. Ha habido momentos buenos y no tan buenos, pero siempre he contado con tu apoyo. Creo que has sabido sacar lo mejor de mí en todo momento y gracias a ello esta tesis ha podido salir adelante.

Gracias también a mis compañeros de IMDEA. Químicos, físicos… ¿Qué más da? A Ramón, por empezar con él esta etapa en el laboratorio. Me enseñaste mucho. Siempre me quedaré con tu frase más celebre (que se pueda contar): “todo se explica con la ecuación del oscilador armónico”. A Sofi, por haber compartido una parte de mi estancia en este centro. Hemos tenido buenas conversaciones y he disfrutado mucho trabajando contigo, aunque fuera poco tiempo. A María, Diego, Yurena y Héctor por haber compartido los desayunos por las mañanas

en esta última etapa. Esos cafés nos han ayudado a desahogarnos a todos. A parte de esos momentos, también quería agradecer individualmente a María por su paso por sala blanca. Gracias por ayudarme con esas muestras, aun estando con mil tareas. Sin duda alguna ha ayudado a que esta tesis alcance un gran nivel. También quería agradecer al Comando Terror. Hemos pasado muy buenos momentos fuera de las puertas de IMDEA, aunque no nos acordemos de todos. A Víctor y Amjad, con los que he coincidido poco tiempo, pero ha sido un gusto trabajar. A Jorge, con quién he compartido también algunos congresos, cafés y charlas en esta última parte. He disfrutado mucho de esos momentos. A Ali por saber cómo sacar de quicio a la gente y aun así, seguir apreciándola. Con tus "TOC" en las presentaciones me has ayudado mucho. A Marina por las discusiones científicas y los buenos momentos en los congresos.

Me gustaría especialmente dedicar unas palabras a Andrés. Monos de laboratorio, nos decíamos. Todos estos años que he podido compartir contigo me han servido de gran ayuda. Nos hemos podido desahogar juntos y he compartido experiencias muy buenas contigo. Me has enseñado mucho, tanto personal como profesionalmente y has tenido que aguantarme demasiado… Muchas gracias por estar ahí en todos esos momentos. Sin ti esta tesis no tendría cabida.

Contents

List of Acronyms

2D	Two-Dimensional
AFM	Atomic Force Microscopy
ALD	Atomic Layer Deposition
BSE	Backscattered Electrons
CVD	Chemical Vapor Deposition
DNQ	DiazoNaphtho-Quinone
EDX	Energy-Dispersive X-ray Spectroscopy
FET	Field Effect Transistor
FWHM	Full Width at Half Maximum
GIS	Gas Injection System
HDR	High Dynamic Range
LED	Light Emitting Diode
ML	Monolayer
NA	Numerical Aperture
NMP	N-Methyl-2-Pyrrolidone
PDMS	Polydimethylsiloxane
PFEBIE	Pulsed Focused Electron Beam Induced Etching
PL	Photoluminescence
PPD	Peak Position Difference

RT	Room Temperature
SEM	Scanning Electron Microscopy
SMU	Source Measuring Unit
TMDCs	Transition Metal Dichalcogenides

Description of Contents

Chapter 1 reviews the state of the art in the fabrication of new devices based on 2D materials, in particular based on MoS_2. The second section relays on the MoS_2 atomic and band structure, which give rise to MoS_2 remarkable optoelectronic properties. The chapter concludes with a overview of MoS_2 FET.

Chapter 2 is focused on the methods and experimental setups used in this thesis, along with the most important characterization techniques. It begins with an explanation of mechanical exfoliation. This chapter describes the deterministic transfer method, which allows depositing flakes in desired positions. The following section corresponds with the fabrication methods, in particular lithographical techniques. The third section describes characterization techniques, including electrical transport at both, RT and cryogenic conditions, spectroscopic techniques (Raman and PL) and microscopic techniques (AFM and SEM).

Chapter 3 covers the study of a method that allows fabricating MoS_2 structures. This method is called Pulsed Focused Electron Beam Induced Etching (PFEBIE) and is based on the combination of a -beam and an etchant gas (XeF_2). First of all, the main conditions and the necessary equipment is presented. Secondly, the parameter space is studied. The last part of the chapter shows how PFEBIE is used to fabricate MoS2 concept devices. It also shows how

PFEBIE is exploited to alter the conduction channel of thickness-variable MoS_2 FETs and fix one of the problems of exfoliation.

Chapter 4 introduces PFEBIE as a patterning tool that allows tailoring the conduction channel of MoS_2 based FETs. In this chapter, the consequences that this technique has over the optoelectronic properties of MoS_2 devices are studied. The first section details the modification of the conduction channel. The second section studies the composition of the devices before and after the patterning via EDX characterization and BSE imaging. The following section relies on the modification of the electric properties after the patterning. The last section of this chapter addresses an optical study of the devices before and after PFEBIE.

Chapter 5 describes how PFEBIE can be used to fabricate lateral MoS_2 homo-junctions. This chapter is focused mainly on the electric properties, but first and second sections give an overview on the new channel fabrication and the Raman spectroscopy respectively. The third section of this chapter studies the electrical properties before and after the fabrication of the diodes. First, the study is carried out at ambient conditions. Secondly, this study is extended to cryogenic temperatures. This chapter shows how the etching parameters can affect the performance of the device. In addition, measurements under different wavelengths are also performed to compare the photoresponse and photocurrent before and after patterning. A variable laser source is used. Additional

optoelectronic measurements under white light were performed, showing that the detecting performance of the device is better after the patterning, increasing its photoresponsivity.

Chapter 1: Introduction

This chapter describes the state of the art in the fabrication of new devices for electronic applications. It is also focused on the main properties of molybdenum disulfide (MoS_2). MoS_2 atomic structure is discussed. After that, a short introduction to the different production methods is presented, including different exfoliation techniques and chemical vapor deposition. A brief summary to MoS_2 band structure is given, showing its semiconductor character. The optical properties are studied focusing on the excitonic transitions present in this material. Finally, a discussion of the electrical properties is presented.

1.1 State of the Art

Graphene was isolated in 2004 through the mechanical cleavage of graphite [1]. The resulting flakes were deposited onto a highly doped silicon (Si) wafer capped with an insulating silicon dioxide (SiO_2) film and contacted with gold electrodes in a multiterminal Hall bar geometry. These samples resulted in the first field effect transistor measurements [1, 2]. After that, a lot of van der Waals (vdW) like materials have appeared. These materials can be mechanically exfoliated due to the weak interaction between adjacent layers. One example of these vdW materials correspond with transition metal dichalcogenides (TMDCs), that can be found easily in nature. These flakes exhibit distinctive thickness-dependent variations in their physical properties [3-5].

This thesis will focus on TMDCs. They have an MX_2 structure. M belongs to the family of transition metals (W, Mo, etc.), which have a partially filled d sub-shell, or which can give rise to cations with an incomplete d sub-shell. X corresponds with a chalcogen atom (Se, Te or S). One layer of M atoms is sandwiched between two layers of X atoms.

TMDCs can be classified like variable band-gap semiconductors depending on their thickness. For example, MoS_2 goes from a 1.2 eV

indirect bandgap in bulk to a 1.8 eV direct bandgap in the monolayer. This property can be exploited in optoelectronic devices, such as transistors or detectors [6-8].

The work on TMDCs is an emerging field since the discovery of potential applications, such as flexible electronics [9], GHz detection [10],or integrated circuits [11]. For example, TDMCs are combined with other 2D materials like graphene to fabricate new van der Waals heterostructures. Recent studies have shown the capability of fabricating P-N heterojunctions using different approaches like material stacking or chemical doping [8, 12, 13]. The burden of these structures appears when involving fabrication steps like resist deposition, chemical manipulation and aligning/lithography procedures that increase the cost and the damage probability of the device's properties.

For that reason, during this thesis, I have developed a method that allows modifying the geometry of the channel of field effect transistors based on MoS_2 by combining an etchant gas and an electron beam. This method is named Pulsed Focused eBeam Induced Etching, PFEBIE. First of all, this method will be studied on individual flakes and will cover chapter 3. Then, the devices will be modified with PFEBIE and the effects will be described in chapter 4. To finish this work, the fabrication of lateral MoS_2 homo-junctions will cover chapter 5

1.2 MoS_2 Atomic Structure

In this thesis, MoS_2 is the material under study. In bulk, it can be found as stacked layers bound by weak van der Waals interactions. The monolayer is formed by a sulfur-molybdenum-sulfur (S-Mo-S) tri-layer whose thickness is 0.69 nm. This monolayer is mostly founded in nature in a hexagonal symmetry, known as 2H-MoS_2 [14]. In this 2H configuration, the monolayer is made of a honeycomb sheet of molybdenum atoms covalently sandwiched between two honeycomb sheets of sulfur atoms in a trigonal prismatic arrangement as illustrated in Figure 1.1a. Apart from this 2H structure, there are two more configurations. 3R-MoS_2 can be found in a rhombohedral structure [15, 16]. A metastable phase can be also present by

intercalating 2H-MoS_2 with alkali metals [17-19]. This phase is known as 1T-MoS_2 and has a tetragonal symmetry. The 2H phase is the most commonly found in nature and it has a semiconducting behavior. In the other hand, 3R and 1T phases are not stable. For that reason, it is difficult to produce devices based on 1T/3R MoS2 phases. The 1T phase has a metallic behavior and is used in the fabrication of metallic-semiconducting junctions or proof of concept devices [20, 21].

Like graphene, MoS_2 can be obtained by mechanical exfoliation, that is the preferred method for obtaining the highest electrical and optical quality flakes. This method, however, is not scalable. Liquid phase exfoliation has proven to be a high yield and quality production method. Nonetheless, this method produces very small flakes, commonly below 100 nm. Taking an industrial point of view, the most promising method for large area and homogeneous MoS_2 films is via chemical vapor deposition (CVD) [22]. However, this method is not straightforward because it requires expensive CVD equipment and optimization of the growth process that can be time-consuming. In this thesis, mechanical exfoliation is chosen due to its easy accessibility, relatively low price, and good properties and it will be covered in greater detail in the Experiments and Methods chapter.

1.3 MoS_2 Band Structure

MoS_2 band structure strongly depends on the thickness [23-25]. The conduction band valley is located at the six corners of the Brillouin zone (K points) and at the midpoint along high symmetry lines Γ-K and M-K as shown in Figure 1.1c. The same figure also shows that the valence band hills are located at the Γ point as well as at the K point where the band is split due to spin-orbit coupling [26-29]. In single layers, the conduction band minimum and valence band maximum coinciding at the K point, making it a direct gap semiconductor as shown in Figure 1.1c. This band structure makes MoS_2 a tunable band-gap material depending on the thickness, suffering a transition from 1.29 eV (961 nm) in bulk to 1.84 eV (673 nm) in monolayer as is illustrated in Figure 1.1d.

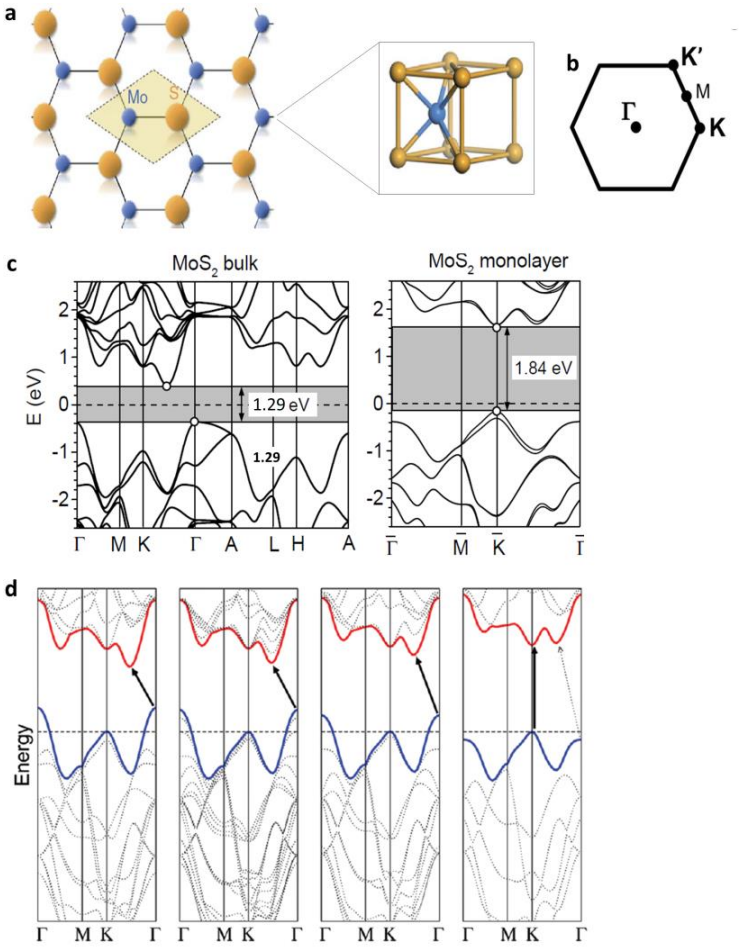

Figure 1.1: a MoS_2 monolayer crystal lattice, consisting of a honeycomb arrangement. Dashed zone corresponds to one primitive cell. The inset shows the surrounding environment of a Mo atom in a trigonal prismatic arrangement. Adapted from [30]. **b** MoS_2 Brillouin zone with some of the high symmetry directions. Adapted from [29]. **c** MoS_2 band structure depending on the thickness. The bulk band structure is shown in the left image. The indirect band-gap is present between the Γ-K symmetry direction. The right image corresponds with the monolayer band structure, where the direct band-gap can be observed along the K symmetry direction. Adapted from [23]. **d** Evolution of the band-gap depending on the thickness going from bulk to monolayer from left to right respectively. Adapted from [25].

Figure 1.2a shows two clear resonances that can be identified in the photoluminescence (PL) spectrum of MoS_2. These two resonances are established to be the direct excitonic transitions at the Brillouin zone K point. Their energy difference is due to the spin-orbit splitting of the valence band [26-29], and these resonances are known as A and B excitons seen in Figure 1.2a. As an indirect band-gap material, PL in bulk MoS2 is a weak phonon-assisted process. When the number of layers is reduced, appreciable PL is observed, and high-intensity PL is detected in monolayer samples as observed in Figure 1.2b.

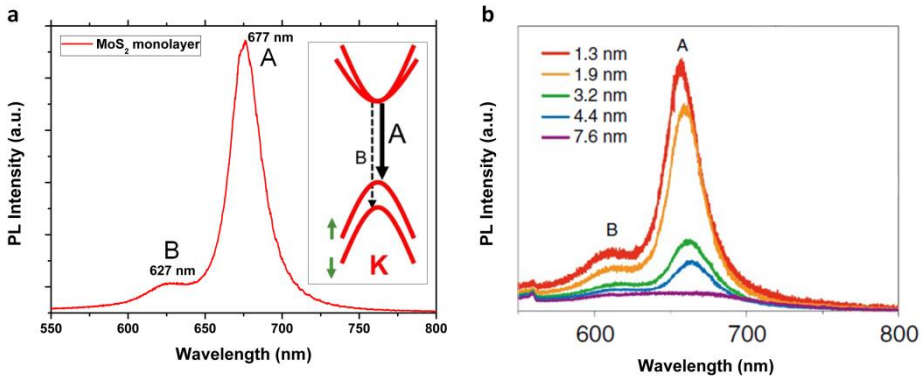

Figure 1.2: a PL spectrum of monolayer MoS2 showing two characteristic resonances. Inset shows the A and B excitonic transitions due to the spin-orbital splitting of the valence band. Inset is adapted from [29]. **b** PL spectra as a function of the number of layers. PL intensity is reduced when the thickness increases. Adapted from [31].

1.4 MoS_2 Electrical Properties

MoS_2 is intrinsic when its Fermi level is located exactly in the middle of the gap. When adding different dopants (N or P dopants), this level can be moved (above or below the middle of the band-gap respectively). Many situations can affect the MoS_2 doping: ambient contaminants such us water or adsorbents, lattice defects, contamination during transfer and fabrication processes, the substrate the MoS_2 sits upon, etc. Chemical dopants [12, 32], ion etching[33, 34], implantation of new species [35], are also different methods that

can vary the doping of MoS_2 and they will be discussed in the next chapter.

The Fermi level of MoS_2 can also be modulated in a field effect transistor (FET) configuration (Figure 1.3a) by applying a gate voltage as Figure 1.3b reveals. FET devices are semiconductor devices in which only one type of carrier predominantly participates in the conduction process. These devices offer many attractive features for high-speed integrated circuits because they can be made from a semiconductor with relatively high electron mobilities [11]. In principle, because FETs are unipolar devices, they do not suffer from carrier storage effects and consequently have higher switching speeds and higher cutoff frequencies than bipolar devices [36]. Further, from a technological point of view, it is necessary to take into account different parameters when a FET device is fabricated. Mobility (μ), ON/OFF ratio (the ratio between the maximum and the minimum conductivity), threshold voltage (the voltage in which the current goes from the minimum to the linear region), subthreshold swing (the change in gate voltage which must be applied in order to create a one decade increase in the output current) are those parameters that can determine the quality of a device and they will be studied in detail in the next chapter (FET device fabrication and characterization details will be also discussed in greater detail in the next chapter).

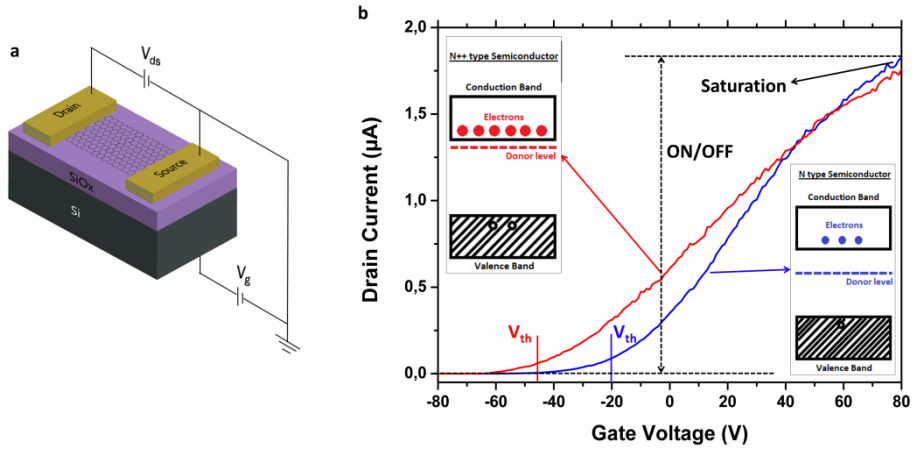

Figure 1.3: a Back gated FET geometry. **b** Transfer IV FET curve for different devices. Each curve corresponds with different doping. The devices were fabricated by optical lithography followed by metal deposition of Cr and Au and a liftoff process.

Bibliography

[1] K. S. Novoselov *et al.*, "Electric Field Effect in Atomically Thin Carbon Films" *Science,* vol. 306, no. 5696, p. 666, 2004.

[2] K. S. Novoselov *et al.*, "Two-dimensional atomic crystals" *Proceedings of the National Academy of Sciences of the United States of America,* vol. 102, no. 30, p. 10451, 2005.

[3] J. Choi, H. Zhang, and J. H. Choi, "Modulating Optoelectronic Properties of Two-Dimensional Transition Metal Dichalcogenide Semiconductors by Photoinduced Charge Transfer" *ACS Nano,* vol. 10, no. 1, pp. 1671-1680, 2016.

[4] X. Huang, Z. Zeng, and H. Zhang, "Metal dichalcogenide nanosheets: preparation, properties and applications" *Chemical Society Reviews,* vol. 42, no. 5, pp. 1934-1946, 2013.

[5] S. Najmaei *et al.*, "Electrical Transport Properties of Polycrystalline Monolayer Molybdenum Disulfide" *ACS Nano,* vol. 8, no. 8, pp. 7930-7937, 2014.

[6] O. Lopez-Sanchez, D. Lembke, M. Kayci, A. Radenovic, and A. Kis, "Ultrasensitive photodetectors based on monolayer MoS2" Nature Nanotechnology, vol. 8, p. 497, 2013.

[7] C. Gong *et al.*, "Electronic and Optoelectronic Applications Based on 2D Novel Anisotropic Transition Metal Dichalcogenides" *Advanced Science,* vol. 4, no. 12, p. 1700231,

[8] J. Y. Lim *et al.*, "Van der Waals junction field effect transistors with both n- and p-channel transition metal dichalcogenides" npj 2D Materials and Applications, vol. 2, no. 1, p. 37, 2018.

[9] J. Pu, Y. Yomogida, K.-K. Liu, L.-J. Li, Y. Iwasa, and T. Takenobu, "Highly Flexible MoS2 Thin-Film Transistors with Ion Gel Dielectrics" *Nano Letters,* vol. 12, no. 8, pp. 4013-4017, 2012.

[10] D. Krasnozhon, D. Lembke, C. Nyffeler, Y. Leblebici, and A. Kis, "MoS2 Transistors Operating at Gigahertz Frequencies" *Nano Letters,* vol. 14, no. 10, pp. 5905-5911, 2014.

[11] H. Wang *et al.*, "Integrated Circuits Based on Bilayer MoS2 Transistors" *Nano Letters,* vol. 12, no. 9, pp. 4674-4680, 2012.

[12] M. S. Choi *et al.*, "Lateral MoS2 p–n Junction Formed by Chemical Doping for Use in High-Performance Optoelectronics" *ACS Nano,* vol. 8, no. 9, pp. 9332-9340, 2014.

[13] R. Frisenda, A. J. Molina-Mendoza, T. Mueller, A. Castellanos-Gomez, and H. S. J. van der Zant, "Atomically thin p–n junctions based on two-dimensional materials" *Chemical Society Reviews,* vol. 47, no. 9, pp. 3339-3358, 2018.

[14] D. R. Edmondson, "Electronic band structure of the layer-type crystal 2H · MoS2" Solid State Communications, vol. 10, no. 11, pp. 1085-1088, 1972.

[15] R. J. Toh, Z. Sofer, J. Luxa, D. Sedmidubský, and M. Pumera, "3R phase of MoS2 and WS2 outperforms the corresponding 2H phase for hydrogen evolution" *Chemical Communications,* vol. 53, no. 21, pp. 3054-3057, 2017.

[16] J. Shi *et al.*, "3R MoS2 with Broken Inversion Symmetry: A Promising Ultrathin Nonlinear Optical Device" *Advanced Materials,* vol. 29, no. 30, p. 1701486,

[17] F. Wypych and R. Schöllhorn, "1T-MoS2, a new metallic modification of molybdenum disulfide" *Journal of the Chemical Society, Chemical Communications,* no. 19, pp. 1386-1388, 1992.

[18] K. C. Knirsch *et al.*, "Basal-Plane Functionalization of Chemically Exfoliated Molybdenum Disulfide by Diazonium Salts" *ACS Nano,* vol. 9, no. 6, pp. 6018-6030, 2015.

[19] X. Fan *et al.*, "Fast and Efficient Preparation of Exfoliated 2H MoS2 Nanosheets by Sonication-Assisted Lithium Intercalation and Infrared Laser-Induced 1T to 2H Phase Reversion" *Nano Letters,* vol. 15, no. 9, pp. 5956-5960, 2015.

[20] M. Acerce, D. Voiry, and M. Chhowalla, "Metallic 1T phase MoS2 nanosheets as supercapacitor electrode materials" Nature Nanotechnology, vol. 10, p. 313, 2015.

[21] X. Guo, G. Yang, J. Zhang, and X. Xu, "Structural, mechanical and electronic properties of in-plane 1T/2H phase interface of MoS2 heterostructures" *AIP Advances,* vol. 5, no. 9, p. 097174, 2019/03/15 2015.

[22] A. Zobel, A. Boson, P. M. Wilson, D. S. Muratov, D. V. Kuznetsov, and A. Sinitskii, "Chemical vapour deposition and characterization of uniform bilayer and trilayer MoS2 crystals" *Journal of Materials Chemistry C,* vol. 4, no. 47, pp. 11081-11087, 2016.

[23] N. I. Yakovkin, "Dirac Cones in Graphene, Interlayer Interaction in Layered Materials, and the Band Gap in MoS2" *Crystals,* vol. 6, no. 11, 2016.

[24] K. F. Mak, C. Lee, J. Hone, J. Shan, and T. F. Heinz, "Atomically Thin MoS2: A New Direct-Gap Semiconductor" *Physical Review Letters,* vol. 105, no. 13, p. 136805, 2010.

[25] A. Splendiani *et al.*, "Emerging Photoluminescence in Monolayer MoS2" *Nano Letters,* vol. 10, no. 4, pp. 1271-1275, 2010.

[26] R. Coehoorn, C. Haas, J. Dijkstra, C. J. F. Flipse, R. A. de Groot, and A. Wold, "Electronic structure of MoSe2, MoS2, and WSe2. I. Band-structure calculations and photoelectron spectroscopy" *Physical Review B,* vol. 35, no. 12, pp. 6195-6202, 1987.

[27] R. Coehoorn, C. Haas, and R. A. de Groot, "Electronic structure of MoSe2, MoS2, and WSe2. II. The nature of the optical band gaps" *Physical Review B,* vol. 35, no. 12, pp. 6203-6206, 1987.

[28] K. F. Mak *et al.*, "Tightly bound trions in monolayer MoS2" Nature Materials, vol. 12, p. 207, 2012.

[29] G. Kioseoglou, A. T. Hanbicki, M. Currie, A. L. Friedman, and B. T. Jonker, "Optical polarization and intervalley scattering in single layers of MoS2 and MoSe2" Scientific Reports, vol. 6, p. 25041, 2016.

[30] T. Cao *et al.*, "Valley-selective circular dichroism of monolayer molybdenum disulphide" Nature Communications, vol. 3, p. 887, 2012.

[31] Y. Jung, J. Shen, and J. J. Cha, "Surface effects on electronic transport of 2D chalcogenide thin films and nanostructures" Nano convergence, vol. 1, no. 1, p. 18, 2014.

[32] D. M. Sim *et al.*, "Controlled Doping of Vacancy-Containing Few-Layer MoS2 via Highly Stable Thiol-Based Molecular Chemisorption" *ACS Nano,* vol. 9, no. 12, pp. 12115-12123, 2015.

[33] E. S. a. A. V. K. Mahdi Ghorbani-Asl and Silvan Kretschmer and Douglas, "Two-dimensional MoS 2 under ion irradiation: from controlled defect production to electronic structure engineering" *2D Materials,* vol. 4, no. 2, p. 025078, 2017.

[34] D. S. Fox *et al.*, "Nanopatterning and Electrical Tuning of MoS2 Layers with a Subnanometer Helium Ion Beam" *Nano Letters,* vol. 15, no. 8, pp. 5307-5313, 2015.

[35] A. Nipane, D. Karmakar, N. Kaushik, S. Karande, and S. Lodha, "Few-Layer MoS2 p-Type Devices Enabled by Selective Doping Using Low Energy Phosphorus Implantation" *ACS Nano,* vol. 10, no. 2, pp. 2128-2137, 2016.

[36] M. F. a. A. Srivastava "A Graphene Switching Transistor for Vertical Circuit Design" ECS J. Solid State Sci. Technol., vol. 5, 3, pp. M13-M21, 2016.

Chapter 2: Experiments and Methods

This chapter concentrates on the processes, equipment and experimental techniques used during this thesis to fabricate and characterize MoS_2 FET devices. Mechanical exfoliation over pre-patterned Si/SiO_2 substrates through a deterministic method is introduced. Secondly, the fabrication of FET devices is described, including tools, lithographic processes, and frequently used techniques to characterize the samples. Finally, different used characterization techniques are subsequently explained, including electrical transport, microscopic characterization techniques, optical measurements, and Raman spectroscopy.

2.1 Mechanical Exfoliation

As mentioned in Chapter 1, different methods can be used to obtain 2D materials. CVD is a method that produces large area and homogeneous 2D films, with a high number of defects and reduced charge carrier mobility. Flakes obtained with liquid phase exfoliation are very small, in the nm scale. In the other hand, mechanical exfoliation is a technique that is in between the other ones, producing flakes of μm^2 areas. For that reason, the production of devices from CVD or liquid phase exfoliated samples require a lot of fabrication steps (transference of the films, wet/dry etching, aligning, etc.). In the other hand, the fabrication process is relatively easy to use when producing devices from mechanically exfoliated flakes. Apart from that, flakes are much purer than the films obtained with CVD, having better electrical and optical properties. These reasons together with inexpensive costs; make mechanical exfoliation the technique that is used in this thesis.

2.1.1 Transfer Method

This method is based on the mechanical cleavage method used for graphene in 2004 [1]. The main difference is that this deterministic-like technique allows localizing the flake in the exactly desire position. This technique was improved by Andrés Castellanos et al. [2].

Figure 2.1 shows the used materials in the exfoliation procedure. From left to right: bulk mineral MoS_2, SPV 224 Nitto tape acquire from Nitto[1], and polydimethylsiloxane (PDMS) with a protective polymeric layer acquire from the company TELTEC[2].

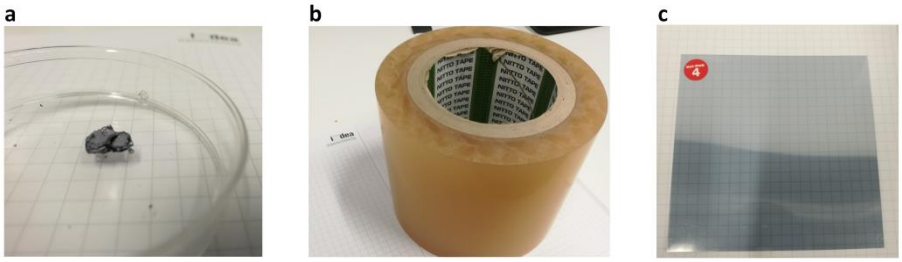

Figure 2.1: Necessary materials for the preparation of devices via mechanical exfoliation. **a** Bulk mineral MoS_2. **b** SPV 224 Nitto tape roll. **c** A 10x10 cm^2 PDMS foil. A 0.5x0.5 cm^2 pice is used in each exfoliation process.

Figure 2.2 shows the entire exfoliation process. The MoS_2 rock is stick to the Nitto tape. After that, the MoS_2 is peeled off several times. The thickest flakes are deposited onto this Nitto tape, which is named mother sample. This process is subsequently repeated until the material is observed much thinner. A piece of PDMS is cut and the protective layer is removed. After that, PDMS is stick to the second or third exfoliated Nitto tape (to obtain thinner material). The pressure is applied to ensure that the PDMS nicely adheres to the material and

[1] https://www.nitto.com/eu/es/products/group/surface/spv_metal/017/
[2] https://www.gelpak.com/gel-film/wf-film/

after that, it is rapidly removed from the Nitto tape. The PDMS has now flakes with different thicknesses. The surface of the PDMS is explored with an optical microscope in order to select the thinnest flakes. As the PDMS is transparent, the contrast is higher if the transmission mode is used.

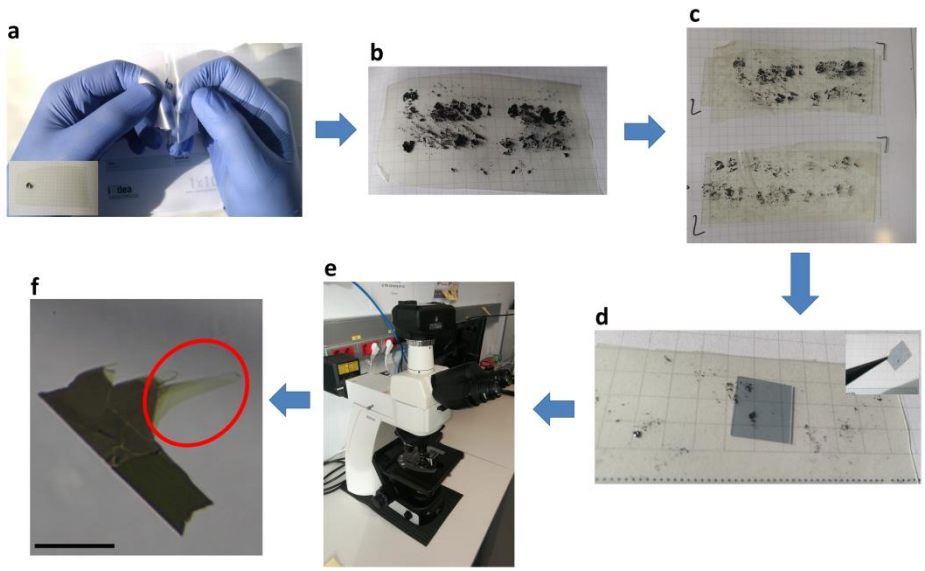

Figure 2.2: Sequence of the whole exfoliation process. **a** Preparation of the mother sample by peeling off several times bulk MoS_2. **b** Aspect of the mother sample once it has been exfoliated. **c** Successive exfoliation samples. Thinner material is observed. **d** A piece of PDMS (grey square) onto the fourth exfoliated Nitto sample. **e** Nikon Microscope used to observe the resulting exfoliated flakes. **f** Typical image obtained in transmission mode. Red circle corresponds with the thinner flake observed in the image. Scale bar is 50 µm

The transfer set up is used once the flakes have been successfully identified. Figure 2.3a shows the setup, which consists of different parts. An XYZ micromanipulator stage acquired from the company Thorlabs[3] is mounted on a magnetic base. This micrometric stage is

[3] https://www.thorlabs.com/thorproduct.cfm?partnumber=RB13M/M

used to mount the PDMS. The sample is placed with double sided tape onto a stage with rotational and XY adjustment bought from the company Thorlabs[4]. The optical part consists of a DSLR camera acquired from the company Canon[5] adjust to a 12x zoom lens and an HDMI TV.

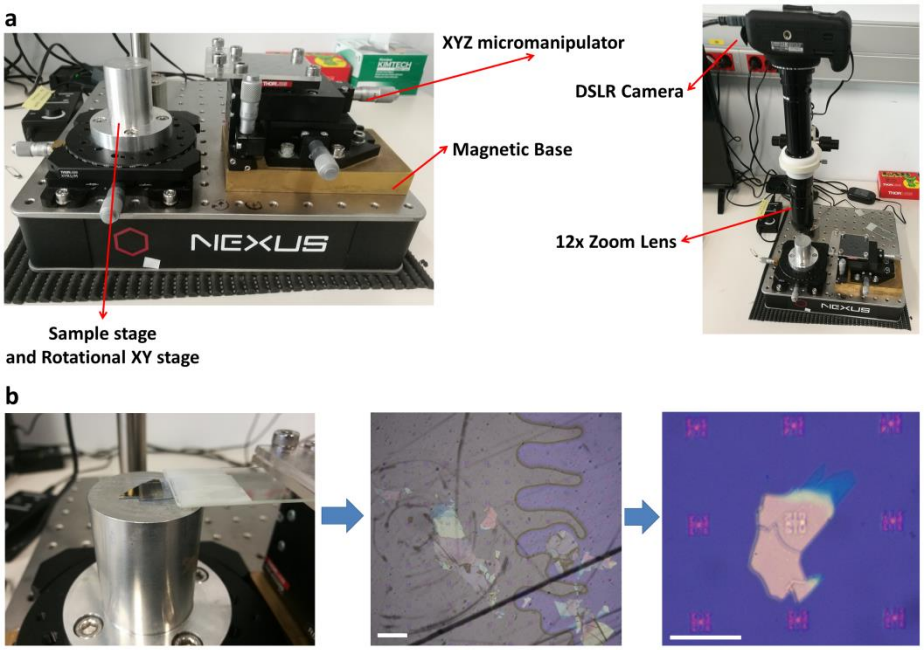

Figure 2.3: a Transfer set up showing the most relevant features. **b** Main steps of the transfer process. From left to right: PDMS positioned and adjusted over the sample. TV image of the PDMS been slowly peeled off, where the wavefront is clearly observed (scale bar is 60 µm). The final image of the transferred flake onto the pattern (scale bar is 60 µm).

Figure 2.3b shows the main steps of the transfer process. A pre-patterned sample (to localize later the flakes) is placed on the sample stage, ensuring flatness. The patterning was done with optical lithography, which will be introduced later in this chapter. The sample

[4] https://www.thorlabs.com/thorproduct.cfm?partnumber=XYR1/M
[5] https://www.canon.es/for_home/product_finder/cameras/digital_slr/eos_1300d/

is imaged with the lens system and is clearly seen in the HDMI TV. The PDMS is mounted on the XYZ stage and is positioned over the sample. The chosen flake is pointed out in the field of view of the camera. Afterward, the desired pattern is focalized. The PDMS is then carefully lowered and adjusted with the micromanipulator making the pattern and the flake to be aligned. When the PDMS is almost touching the sample, both pattern and flake focuses are the same. When the PDMS is touching the sample, it is pressed very carefully against the sample surface. In order to transfer the desires flake, the PDMS is slowly peeled off, releasing the flakes and adhering them to the pre-patterned sample. The working principle of this technique is based on the viscoelasticity of the PDMS. Macroscopically and at short time scales, it behaves as a solid, but microscopically and at very long time scales, it slowly flows over the contact surface [3].

2.2 Micro and Nano-fabrication

2.2.1 Optical Lithography

Optical lithography, also known as photolithography, is a microfabrication technique in which light is used to transfer a pattern onto a substrate via a light-sensitive polymer, known as photoresist. The pattern is created, either directly or with a projected image using an optical mask. By selectively exposing parts of the photoresist, windows can be opened in the underlying substrate to make subsequently microfabrication processes, such as film deposition dry/wet etching.

2.2.1.1 Instrumentation and Optics

In this thesis, a direct optical method is used, in which the laser directly writes the pattern onto the photoresist. In this thesis, a Heidelberg DWL 66FS equipment is used, shown in Figure 2.4a, with a laser excitation wavelength of 405 nm. The sample is placed in the

interferometric stage, observed in Figure 2.4b. The laser is turned on and off while the interferometric stage is moved. The laser focus can be controlled via a PID sensor in optical or pneumatic mode, depending on the sample size (pneumatic mode can only be used for high area samples, more than 2 cm^2).

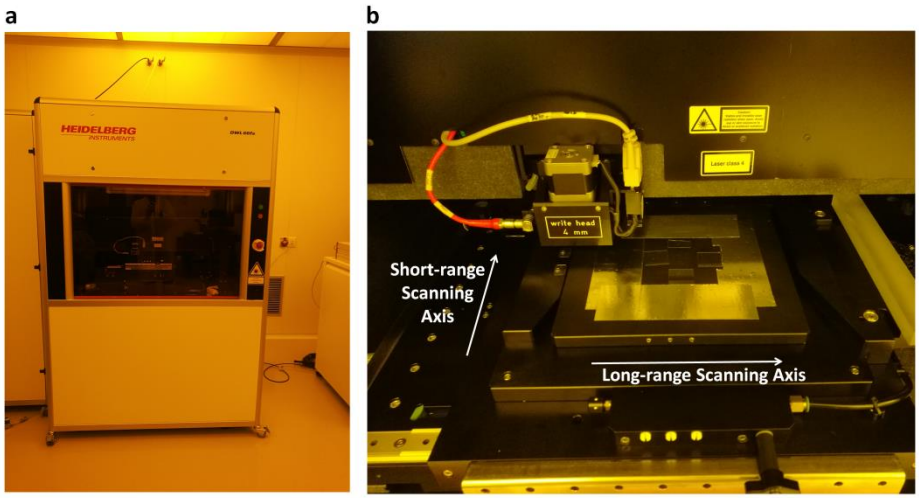

Figure 2.4: a Maskless optical laser writer equipment. Heidelberg DWL 66FS model. **b** XY Interferometric stage showing the movement directions.

A general view of a photolithography optic system is observed in Figure 2.5a. The universally accepted definition of resolution of an optical system [4] is that the maxima generated by one point must not be closer than the first minima of the second point (Figure 2.5b). Using this definition, the smallest feature that can be projected is given by

$$R = \frac{1{,}22 \cdot f \cdot \lambda}{d} \qquad \textbf{(2.1)}$$

where f is the distance from the focusing lens to the resist on the image plane, d is the diameter of the focusing lens and λ is the excitation wavelength. The resolution can also be expressed as

$$R = \frac{K_1 \cdot \lambda}{NA} \tag{2.2}$$

where K_1 is an experimental parameter that depends on the lithography system and NA is the numerical aperture of the objective lens used to focus the laser [5]. The NA is a function of the angle and is expressed as

$$NA = n \cdot sin\theta \tag{2.3}$$

where n is the refraction index (n=1 for air).

The commonly accepted restriction is that the difference in path length of two rays can be no more than λ/4 [4]. This restriction has an effect on Equation 2.2. If the resolution limit wants to be decreased, the lens has to be very large with a high numerical aperture. This is not possible because Rayleigh criteria for the depth of focus would be violated. The depth of focus is the distance over which the image will be on focus from the image plane. The larger the lens, the smaller the depth of focus. The Rayleigh criterion requires that

$$\frac{\lambda}{4} = \Delta z - \Delta z \cdot cos\theta \tag{2.4}$$

Assuming small angles, we can use that

$$\frac{\lambda}{4} \cong \Delta z \left[1 - \left(1 - \frac{\theta^2}{2}\right)\right] = \Delta z \frac{\theta^2}{2} \tag{2.5}$$

$$\Delta z = \frac{\lambda}{2 \cdot \theta^2} \tag{2.6}$$

$$\theta \cong sin\theta = \frac{NA}{n} \tag{2.7}$$

Combining equations 2.6 and 2.7 we obtain that the depth of focus is

$$\Delta z = \frac{n \cdot \lambda}{2 \cdot (NA)^2} \tag{2.8}$$

An increase in the numerical aperture will improve the resolution as seen in equation 2.2, but it will reduce the depth of focus. A reduction in the excitation wavelength also causes a better resolution, reducing the depth of focus and making the process sensitive to experimental parameters, such as variations in the photoresist thickness. A decrease in the focus could also increase the resolution (equation 2.1).

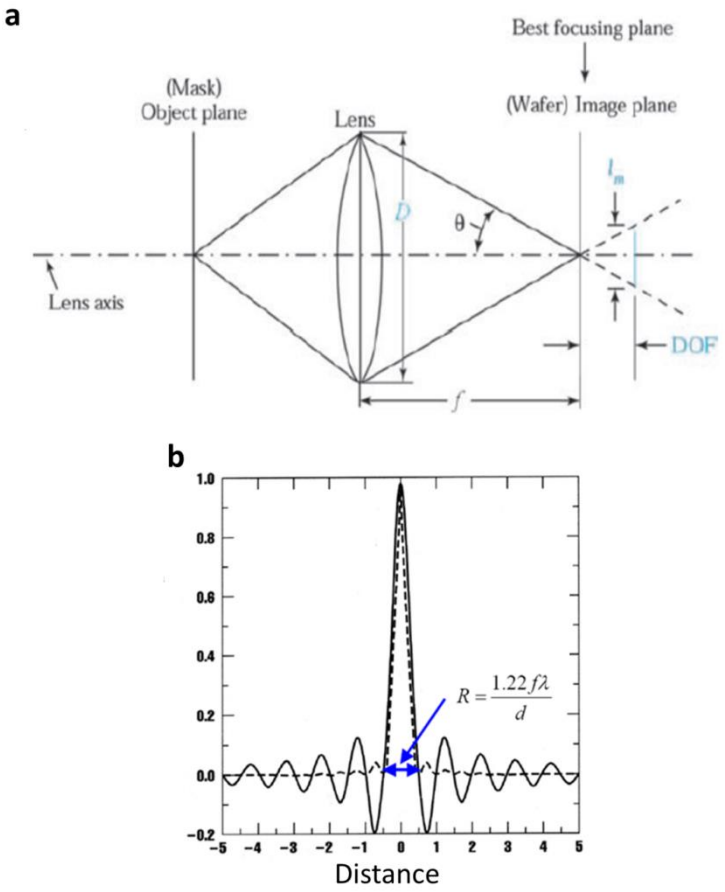

Figure 2.5: a Scheme of an optical system for a focusing laser beam. Adapted from [6] **b** Fraunhofer resolution limit. Adapted from [4].

2.2.1.2 Photoresists

A photoresist is a light-sensitive material composed by a polymer whose molecular weight and chain length are crucial for its solubility in certain solvents, known as developers. The photoresist has a photoactive compound, which, when exposed to a dose of light higher than a threshold value, produces a variation in the chain length, changing its solubility. For negative photoresist, exposure above the threshold value causes the bonding of chains, increasing the molecular weight and reducing the solubility. Positive photoresists work in the

opposite way: exposure of UV light above the threshold value causes chain shortening, reducing the molecular weight and increasing the solubility.

In this thesis, the used resists are AZ1505 and AZ1512HS positive photoresist acquired from the company MicroChemicals[6]. They are deposited onto substrates by spin coating at 4000 rpm (see Figure 2.6a for thickness vs. speed curves), followed by heating at 90 °C during 60 seconds in order to evaporate the organic solvents. The photoactive compound is diazonaphthoquinone (DNQ) (seen in Figure 2.6b), and the polymer is a phenol polymer commonly known as Novolak (Figure 2.6c). Upon UV exposure, the DNQ undergoes a Wolff rearrangement to form a ketene (Figure 2.6d) [7], which reacts with ambient water to form a base soluble carboxylic acid, inducing chain scission in the Novolak, and increasing the solubility in alkaline developer solutions. After UV exposure, the photoresist is developed in AZ351B developer acquired from the company MicroChemicals for 60 seconds. Figure 2.7a shows a scheme of the entire process for a positive photoresist.

Taking into account the discussion of the previous sections, the minimum feature size at an excitation wavelength of 405 nm is around 500 nm for the AZ1505 resist and 1 µm for the AZ1512HS resist.

The contrast describes the ability of the resist to distinguish between light and dark. Figure 2.7b shows the contrast curve for a positive resist. This curve represents the proportion of developed resist as a function of the exposure dose in a logarithmic scale. The contrast is defined as

$$\gamma = \frac{1}{\log(\frac{D_f}{D_0})} \qquad \textbf{(2.9)}$$

[6] https://www.microchemicals.com/products/photoresists/az_1505.html

where D_0 is the exposure dose at which the resist first begins to dissolve (can be calculated where the tangent of the curve at D_f intercepts 1) and D_f is the exposure dose at which the resist is completely dissolved.

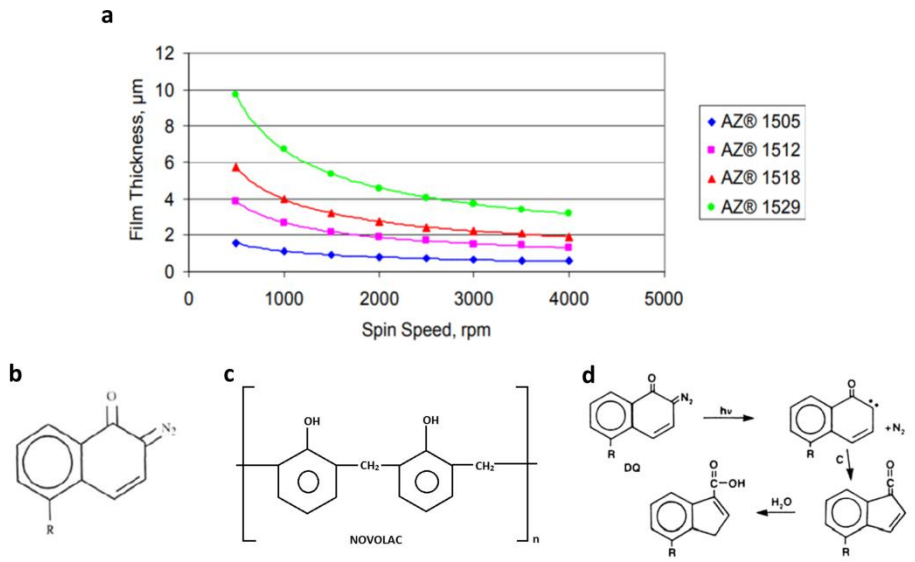

Figure 2.6: a Characteristic film thickness (µm) vs. angular velocity (rpm) curve for different resists. AZ1505 and AZ1512 are the resists that have been used in this thesis, with a film thickness of 0.5 µm and 1.2 µm respectively. Adapted from [8]. **b** Structure of DNQ molecule. Adapted from [9]. **c** Structure of Novolak polymer. Adapted from [10]. **d** Scheme of a Wolff rearrangement process mediated by light exposure. Adapted from [9].

The tendency of a resist to deviate from a perfectly vertical wall is characterized by its contrast. For high contrast resists such as the ones used along with this thesis, erosion is still present (depending on the laser intensity, focus and resist conditions), causing a tilted sidewall as the one is observed for positive resist in Figure 2.7c. When the photoresist is removed using different solvents in a process known as liftoff, the tilted sidewall can be a problem because the accumulation of metal and resist in the sidewalls. N-Methyl-2-Pyrrolidone (NMP) is

the best solvent to remove the resist and the metal present in the sidewalls due to its low vapor pressure and high flash point (at 80-90 °C).

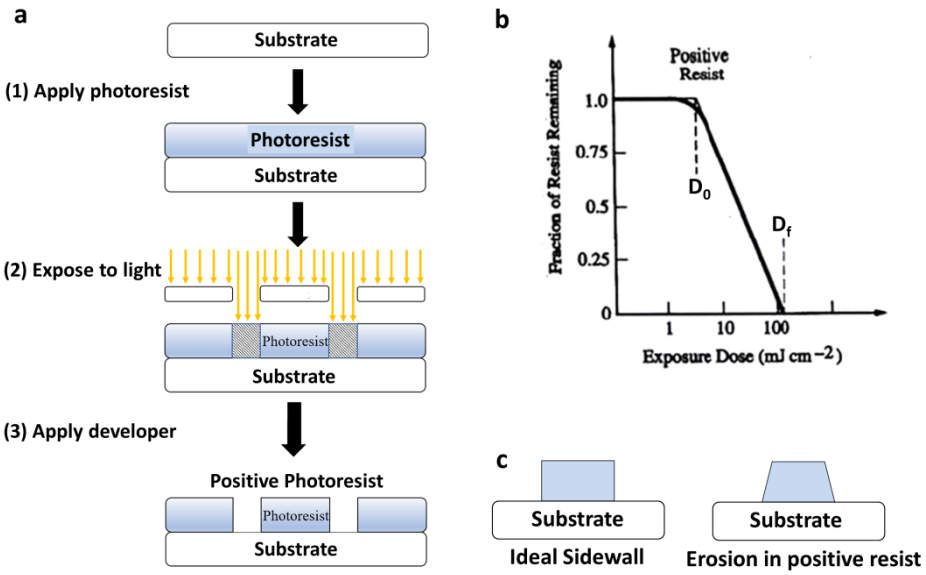

Figure 2.7: a Scheme of the main steps for positive resist. Adapted from [11]. **b** Portion of remain resist as a function of the exposure dose. D_0 and D_f are the characteristics to calculate the contrast. Adapted from [9]. **c** Left: ideal vertical sidewall. Right: eroded sidewall corresponding with a positive photoresist.

2.2.1.3 Correlative Maskless Laser Optical Lithography

In this thesis, a method has been developed to make photolithography a more efficient process. The patterned substrate used to exfoliate the material is employed to identify where the exfoliated flakes are. The pattern consists of a square matrix indicating the number of row and column (see Figure 2.8a). Each element of the matrix has a coordinate (given by the geometry created with Elphy Multibeam software[7]).

[7] https://www.raith.com/products/elphy-multibeam.html

When the flakes are localized via optical microscopy, a photo is taken. After that, it is necessary to correct the image (angle and size) via software manipulation (SVG Marks[8]). With this software correction, it is possible to define the same coordinate system for flakes and matrix as seen in Figure 2.8b. Subsequently, the device geometry is created with the Elphy Multibeam software as seen in Figure 2.8c.

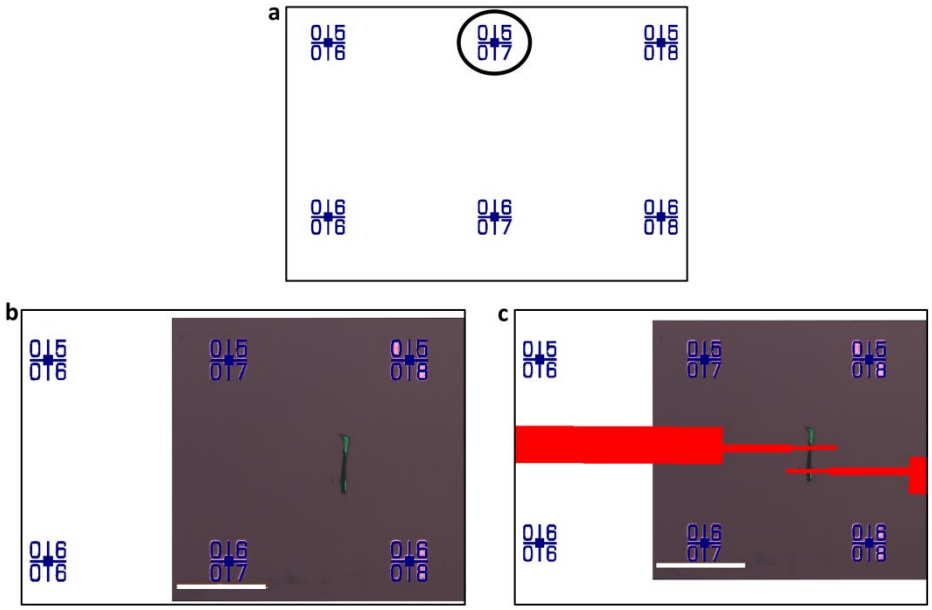

Figure 2.8: a Matrix indicating the row and the column. The circle shows an example of the pattern (indicating row number 5 and column number 7) **b** Corrected image taken with a 75X objective. Scale bar is 50 µm. The correction allows the image and the geometry to have the same coordinate system. **c** Electric contacts drawn with the lithographical software. Scale bar is 50 µm.

Once the geometry has been created, it is transferred to the DWL66FS Heidelberg equipment. By aligning the sample and indicating which the matrix coordinates are, the lithography is launched. After that, the photoresist is developed in AZ351B developer for 60 seconds. Then the metal deposition is performed in a thermal evaporator. After that,

[8] http://lness.como.polimi.it/svgmarks.php#svgmarksdownload

a liftoff process in acetone is carried out overnight, followed by an NMP and IPA rinse during 10 minutes. Figure 2.9a shows an example of the entire correlative optical lithography process. The first image corresponds with the exfoliated flake. The second one coincides with the optical lithography step. The final image reveals a totally fabricated device, with the evaporated electrodes. This method allows contacting as many flakes as desired as seen in Figure 2.9b, where 12 devices were exposed in less than 10 minutes.

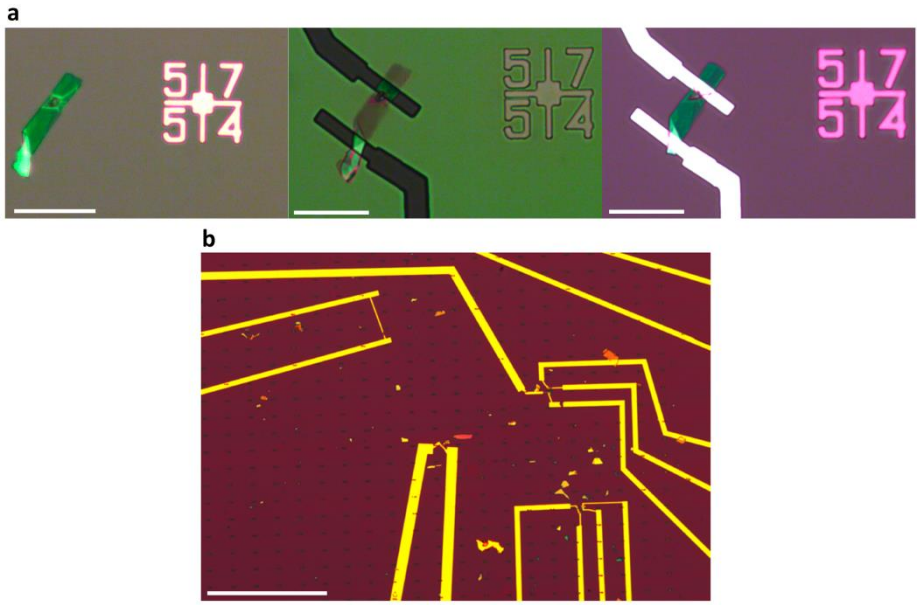

Figure 2.9: a Sequence of the correlative maskless optical lithography. From left to right: microscope image of the exfoliated flake. Optical image of the resulting lithography. Metal deposition and liftoff. Scale bars are 20 µm **b** Example of a sample containing 12 devices. Scale bar is 500 µm.

The following table shows a resume of all the fabrication steps in the production of a sample.

Step #	Description
1º	Fabrication of the pre-patterned substrate with AZ1512HS resist
2º	Exfoliation and optical imaging
3º	Software correction and geometry
4º	Resist spinning and optical lithography with AZ1505
5º	Developing in AZ351B for 60 seconds
6º	Cr and Au deposition in a thermal evaporator
7º	Liftoff in acetone overnight and NMP/IPA rinse during 10 minutes

Table 1: Description of the whole fabrication process

2.2.2 Gas Injection System

Once a device has been fabricated it is difficult to modify its geometry or thickness. For that reason, in this thesis, a new tailoring method is studied to modify the geometry of a fabricated device and produce specific structures (covered in chapter 3). For that porpoise, a gas injection system (GIS) is employed.

Figure 2.10 shows the GIS mounted inside the chamber of a FIB-SEM Auriga Ultra High Definition Scanning Electron Microscope (UHD-SEM)

acquired from Carl Zeiss[9]. It consists of a reservoir where the chemical substance is present at a certain temperature. It also has a microneedle system as will be explained in chapter 3.

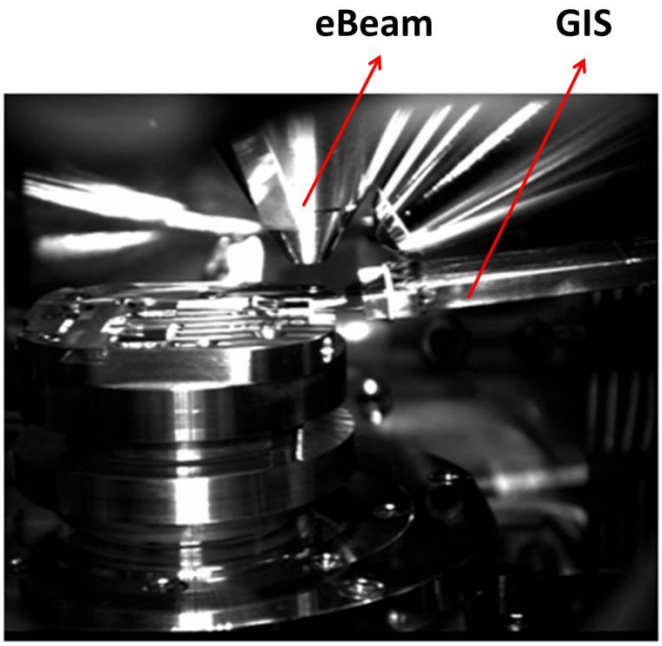

Figure 2.10: Photography took inside the UHD-SEM chamber.

2.3 Characterization Techniques

2.3.1 Electrical Transport

2.3.1.1 Instrumentation

Electrical characterization was done via transport measurements under both, ambient and vacuum conditions. Figure 2.11 shows the set up for electrical measurements carried out in vacuum conditions.

[9] https://www.zeiss.com/microscopy/int/products/fib-sem-instruments.html

Taking that into account, a Keithley 2614B unit is used[10]. This system has been wired directly to a cryostat (Optistat DN buy from the company Oxford Instruments[11]) that allows working at different temperatures (from liquid nitrogen temperature (77 K) to 500 K).

Figure 2.11a shows the entire set up. The sample is mounted with insulating varnish in a chip carrier, as shown in Figure 2.11b. The sample must be smaller than 0.5x0.5 cm^2. It is necessary to perform wire bonding from the sample electrodes to the chip carrier in order to ensure the electrical contact. The wires are made of gold. It is recommended to bond at least two wires per electrode because the junction between wire and electrode is weak.

Figure 2.11c shows the cryostat optical window which allows performing optoelectronic measurements in vacuum conditions. As described in chapter 5, the generated photocurrent of the MoS_2 devices will be studied as a function of different wavelengths. To perform these measurements, a coupled optical set up is necessary, as Figure 2.11d and 2.11e reveal. The optical path and components are shown in Figure 2.11e. A white LED is used to obtain an optical image of the sample inside the cryostat. A variable wavelength laser (Fianium Superchrome) is coupled to a cage system to excite the sample and perform the photoresponse measurements. The cage system is coupled to a spectrometer, in which the signals are collected by a fiber coupler.

The Keithley 2614B has two source measure unit (SMU). The SMU is commonly used for applications requiring high accuracy and measurement flexibility Its four-quadrant design allows it to simultaneously source and measure both current and voltage. To simplify the wiring, all devices measured in vacuum conditions have one common grounded electrode.

[10] https://www.tek.com/keithley-source-measure-units/smu-2600b-series-sourcemeter
[11] https://nanoscience.oxinst.com/products/cryostats-for-spectroscopy/optistatdn

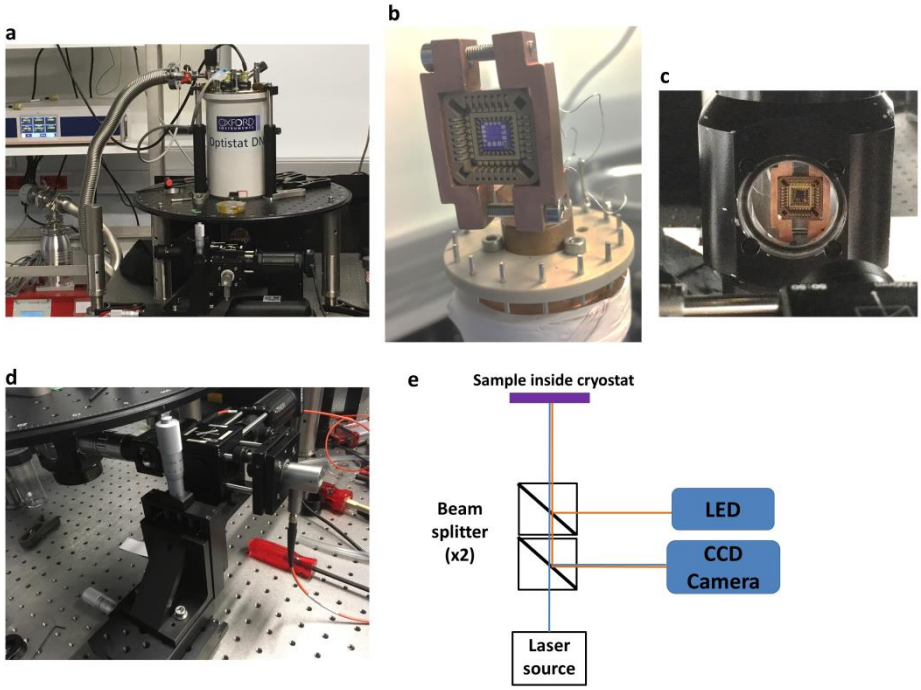

Figure 2.11: a Cryostat set up **b** Sample mounted on a chip carrier **c** Optical window **d** Coupled optical setup **e** Schematic of the optical path

Ambient measurements were carried out using a Keithley 4200-SCS probe station with four SMU. Four probes can be simultaneously connected, and each of them is able to produce current or voltage and measure current and voltage at the same time. Figure 2.12a shows the probe station system. This system has a moveable stereo zoom optical microscope to observe the sample, which is mounted on an XYZ stage. Back-gated field effect transistor measurements were carried out using two probes contacted to the device's electrodes, and another needle for the gate electrode. When doing electrical measurements under light illumination, an extra set up is added to the probe station as Figure 2.12b shows. A white light emitting diode (LED) is sat in the back part of the probe station (red circle of Figure 2.12c). The LED is connected to a pulse generator (TG310 3Hz Pulse Generator buy from

TTI[12]) and allows performing photoresponse measurements under different duty cycle excitation.

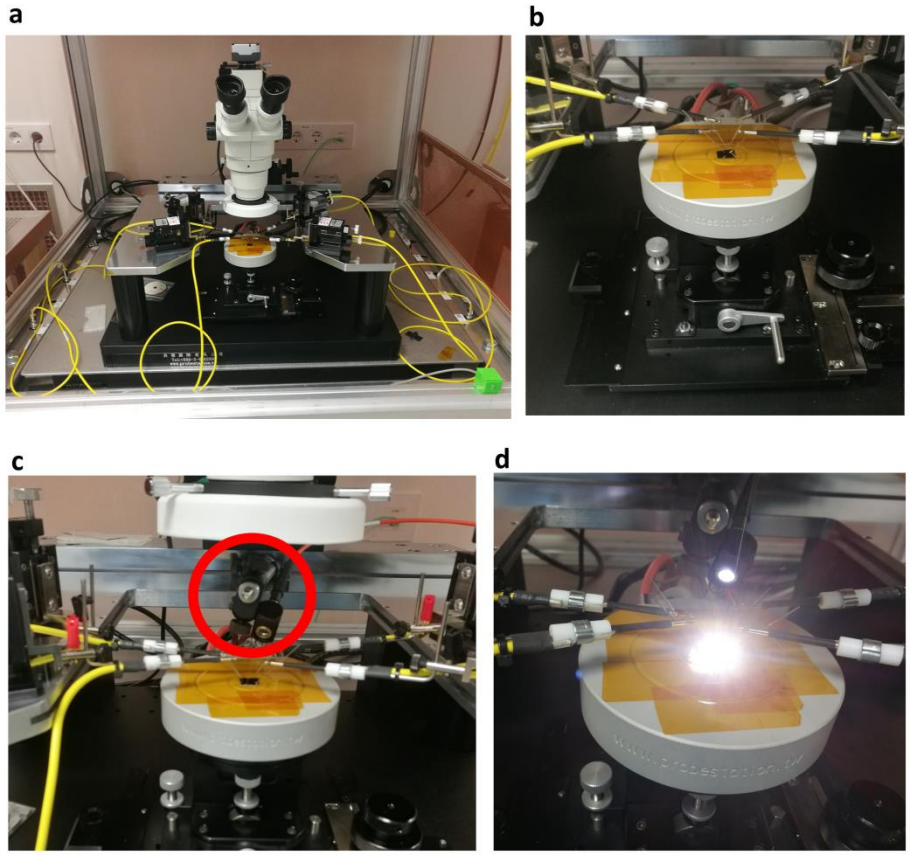

Figure 2.12: a Image of the probe station. **b** Zoom of the XYZ stage. **c** Image of the stage where the LED is observed (red circle). **d** Zoom of the probe station when the LED is emitting.

2.3.1.2 Field Effect Transistors

A field effect transistor (FET) is a device that works controlling the current between its terminals by applying an electric field (controlled with the gate). A FET can be described as a parallel plate capacitor, where one capacitor plate is the gate and the other plate is the MoS_2

[12] https://www.aimtti.com/product-category/legacy-products/aim-tg310

device channel. Although a top gated configuration is the most common way of fabrication in FET devices, the measurements in this thesis have a back-gated configuration to simplify fabrication processes and to allow optical characterization. The MoS_2 flake is separated by a 285 nm SiO_2 film from the degenerately doped silicon gate (the employed silicon has a metallic behavior because its doping makes the Fermi level energy to be really close to the valence or conduction band).

Figure 2.13a shows the drain to source current (I_{ds}) vs. drain to source voltage (V_{ds}) characteristic curve of a FET as a function of different gate voltages. At drain to source voltages much less than the gate to source voltages, changing the gate voltage will change the channel resistance. In this situation, the FET operates like a resistor and it is said to be in the linear region. If the drain to source voltage is highly increased, the channel changes asymmetrically and the FET is said to be in saturation mode.

The carrier density in a FET channel induced by a gate voltage can be expressed as

$$n = \frac{C_{ox}}{q}\left(V_{th} - V_g\right) \tag{2.10}$$

where q is the elementary electron charge, V_{th} is the threshold voltage (an indirect measurement of the doping of the FET conduction channel), and C_{ox} is the oxide capacitance and is given by

$$C_{ox} = \frac{\varepsilon_0 \varepsilon_r}{d} \tag{2.11}$$

where ε_0 is the vacuum permittivity and ε_r is the relative permittivity of the oxide(ε_r=3.9 for SiO_2), and d is the oxide thickness (285 nm) [5]. For that reason, changing the charge density (changing the gate

voltage) is equivalent to modulate the Fermi level energy. By setting V_g at zero the doping concentration of the channel follows

$$n_0 = \frac{C_{ox}}{q} V_{th} \tag{2.12}$$

With that in mind, for $V_{th} < 0$, $n_o < 0$ and the device will be N-doped. For $V_{th} > 0$, $n_o > 0$ the device will be P-doped. For voltages between the threshold voltage and the inversion mode, the device is in depletion mode (the mobile charge carriers are diffused by an electric field), and it would have practically no current flowing [5].

The conductivity of the 2D channel is given by

$$\sigma = \frac{1}{\rho} = n \cdot q \cdot \mu \tag{2.12}$$

where ρ is the resistivity of the channel and μ the mobility.

Taking into account the definition of resistivity equation 2.12 can be expressed as

$$\sigma = \frac{L}{W} \cdot \frac{I_{ds}}{V_{ds}} = n \cdot q \cdot \mu \tag{2.13}$$

where L and W are the device length and width, respectively. Substituting equation 2.10 into 2.13

$$\sigma = \frac{L}{W} \cdot \frac{I_{ds}}{V_{ds}} = \frac{C_{ox}}{q} \cdot V_g \cdot q \cdot \mu \tag{2.14}$$

Isolating I_d and deriving with respect to V_g, the mobility is described as

$$\mu = \frac{L}{W \cdot C_{ox} \cdot V_{ds}} \cdot \frac{dI_{ds}}{dV_g} \qquad \textbf{(2.15)}$$

A I_{ds} vs. V_g transfer curve at RT conditions as the observed in Figure 2.13b can be used to calculate the mobility (equation 2.15) and the threshold voltage, using the extrapolation in the linear region method for dI_{ds}/dV_g [12]. For this device, the resulting mobility is 10.5 $cm^2V^{-1}s^{-1}$ and V_{th} is -35 V.

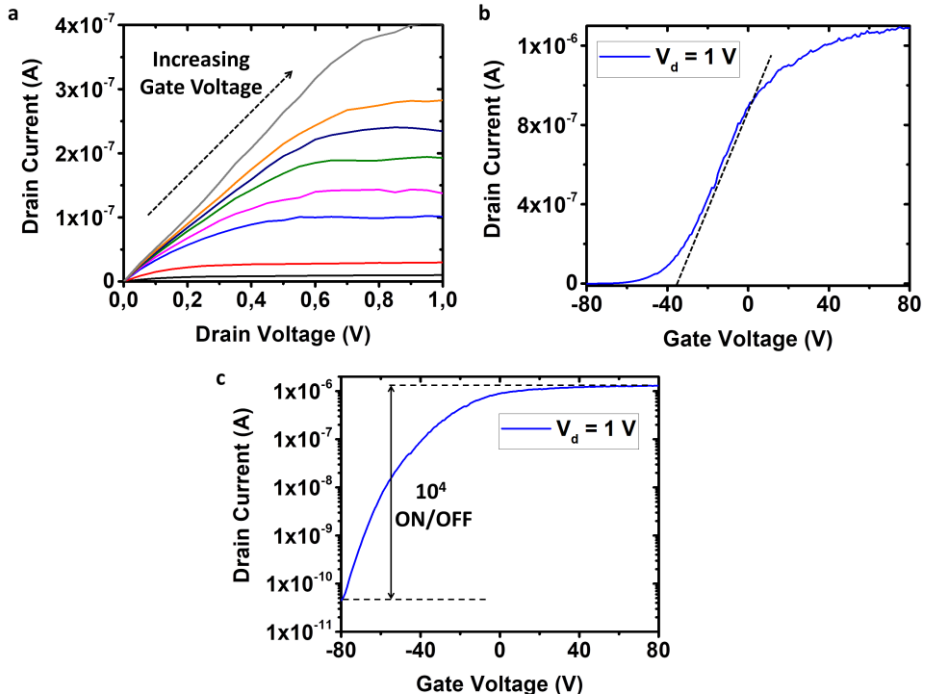

Figure 2.13: Transfer characteristic of a fabricated MoS_2 FET at room temperature. **a** I_d vs. V_d curve as a function of the gate voltage bias. Both, linear and saturation regions are observed. **b** I_d vs. V_g curve for a V_d bias of 1 V. Mobility is calculated by the extrapolation in the linear region method (using the slope in the linear region calculated with the black dashed line). **c** Logarithmic plot of the curve shown in Figure 2.12b. ON/OFF ratio results on 10^4.

Figure 2.13c shows the same curve in the logarithm scale. It is also possible to calculate the ON/OFF, which indicates the ability of a device to shut down and not consuming current despite the applied V_d. This ON/OFF ratio can be obtained as the ratio between the currents in the saturation state and in the depletion state.

Electrical characterization was also performed at vacuum and low temperature conditions in the set up shown in Figure 2.11. IV transfer characteristics were carried out from 77 K to 300 K at a pressure of $1x10^{-6}$ mbar. Figures 2.14 and 2.15 show an example of the electrical characterization of a device under cryogenic conditions. Figure 2.14a shows the characteristic behavior of a transistor. The same behavior than Figure 2.13a is observed by varying the gate voltage. Figure 2.14b shows the transistor behavior under gate sweeping from -100 V to 100 V at different temperatures. By decreasing temperature, the threshold voltage increases, indicating that this parameter strongly depends on temperature. This behavior is also shown in Figure 2.15c, where the threshold voltage value has an exponential dependence with temperature. Using an electro-thermal model [13], similar to the Arrhenius equation, the threshold voltage V_{th} can be expressed as:

$$V_{th} = A \cdot \exp\left(\frac{-E_a}{K_B T}\right) \quad \textbf{(2.17a)}$$

where A is an exponential factor, K_B is the Boltzmann constant, T is the temperature and E_a is the threshold voltage activation energy.

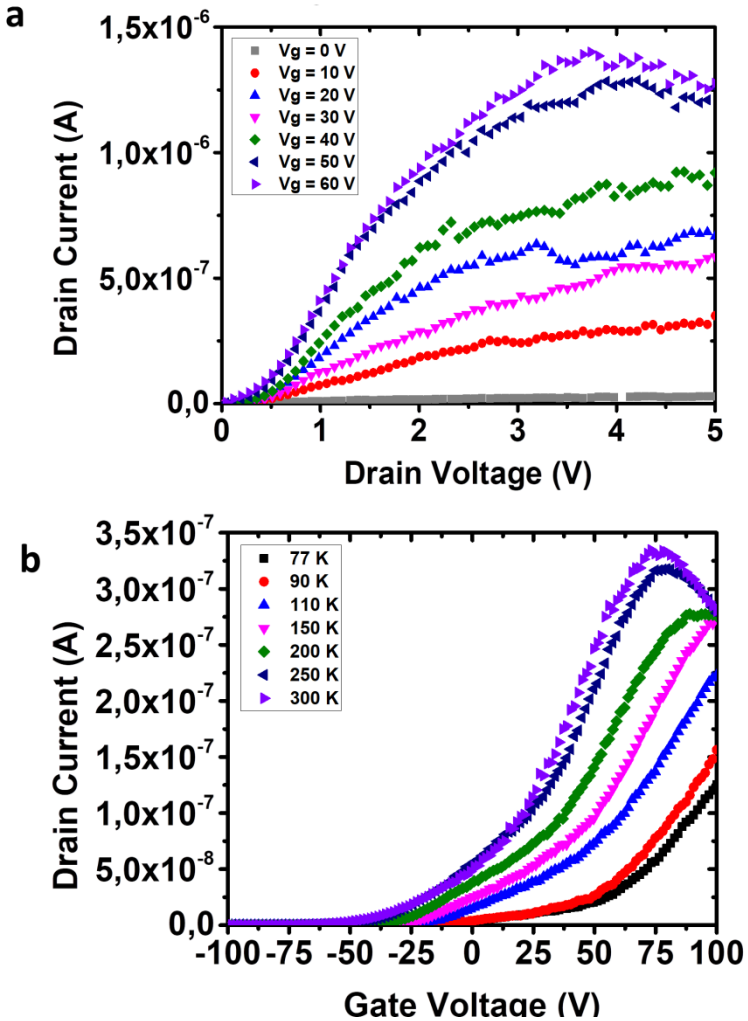

Figure 2.14: Characterization of a fabricated MoS_2 FET at cryogenic conditions. **a** I_d vs. V_d curve as a function of the gate voltage bias at 300 K and $1x10^{-6}$ mbar. **b** I_d vs. V_g curve for a V_d bias of 500 mV at different temperatures. Threshold voltage depends on the temperature.

Figure 2.15c shows that the exponential decay proposed in equation 2.17 is in good agreement with the experimental data. The Activation energy results on 26 meV. This energy can be also calculated from the Arrhenius plot shown in Figure 2.15d. The Arrhenius equation can be expressed as:

$$\ln(I_{SD}) = \ln(B) - \frac{E_a{}'}{K_B} \cdot \frac{1}{T} \quad \textbf{(2.18)}$$

Where B is an exponential factor; I_{SD} is the drain current, E_a' is the activation energy; K_B is the Boltzmann constant and T the temperature. In this case, the activation energy is 22 meV. The ratio E_a/E_a' is 1.18, showing that the energies calculated by different methods are in good agreement. This energies also agrees with previously reported studies [14, 15].

Figure 2.15b reveals that mobility also depends on temperature. It decreases when decreasing temperature. In a semiconductor, the mobility is temperature dependent. There are two types of scattering mechanisms that can influence the mobility of the device: lattice scattering and impurity scattering. Lattice vibrations cause mobility to decrease when increasing temperature. Nonetheless, the mobility of carriers in a semiconductor is also influenced by charged impurities. The mechanism underneath is totally opposite to the lattice scattering mechanism: at low temperatures, carriers move more slowly and there is more time for them to interact with these impurities. As a consequence, when temperature decreases, impurity scattering increases and thus, the mobility decreases. The mobility dependence with temperature due to impurity scattering is $T^{+3/2}$, while the temperature dependence due to lattice scattering is $T^{-3/2}$ [16]. That is the reason why in Figure 2.15b mobility increases with temperature.

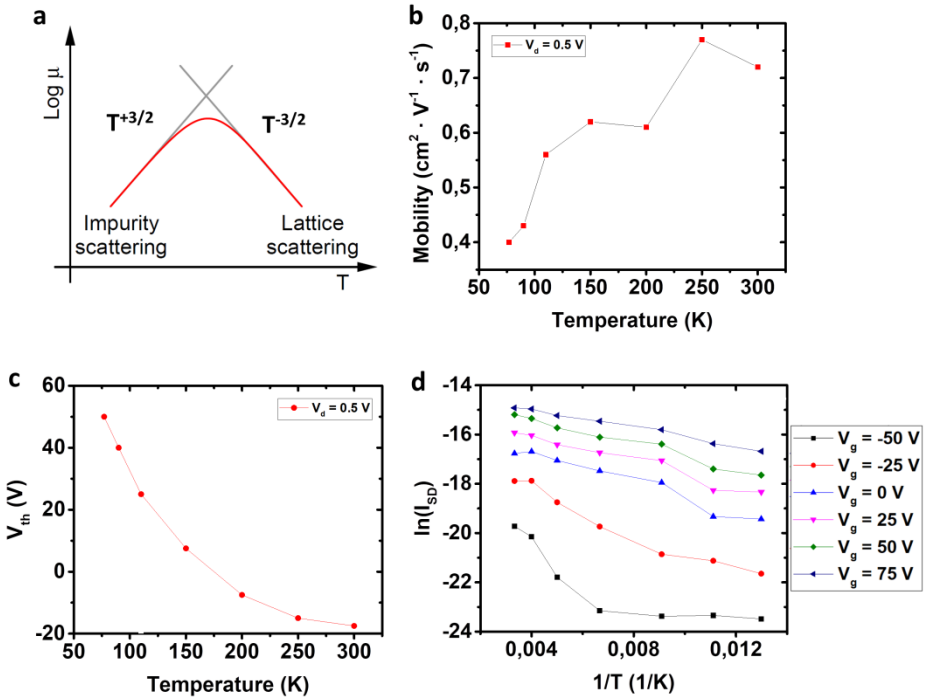

Figure 2.15: a Temperature dependence of mobility taking into account different regimes: impurity and lattice scattering. Adapted from [16] **b** Calculated mobility as a function of temperature in a fabricated device. Mobility increases when the temperature increases. **c** Threshold voltage value as a function of temperature of the same device in b. V_{th} was obtained from the curve of Figure 2.14b. A clear dependence on temperature is observed. **d** Arrhenius plot of the drain current as a function of the inverse of temperature.

2.3.1.2.1 Optoelectronic Properties

As MoS_2 is a semiconductor, electrical properties depend strongly on the light. For that reason, it is important to study how the IV characteristics of MoS_2 FET behave as a function of light excitation. Figures 2.16 and 2.17 show the electrical response under light illumination reported by different authors [17, 18].

Figure 2.16 shows the energy band diagram under different illumination and gate conditions. Figure 2.16a shows the equilibrium

condition, where the device is not illuminated and without drain or gate bias. In this state, the device is characterized by small Schottky barriers at the electrodes due to the Fermi energy alignment between the MoS_2 and the gold contacts. Figure 2.16b shows the situation in which the device is illuminated in the OFF state (V_g lower than V_{th}). The light is absorbed and the electron-hole pairs can be extracted by applying a bias between the source and drain electrodes. In the ON state (V_g higher than V_{th}), thermionic and tunneling currents also contribute to the device current, as Figure 2.16c shows. Measuring in the OFF state results on a reduced dark current. In the other hand, measuring in the ON state results in a more efficient photocurrent extraction and a higher photoresponse [17].

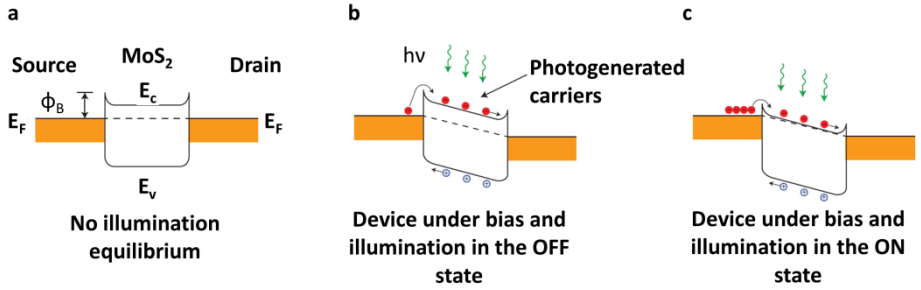

Figure 2.16: a Energy band diagram without illumination. Yellow zones correspond with the gold electrodes. **b** Energy band diagram for $V_g<V_{th}$ under illumination. **c** Energy band diagram for $V_g>V_{th}$ under illumination. Adapted from [17]

The photocurrent (I_{ph}) is defined as the difference between illumination and dark current and can be expressed as:

$$I_{ph} = I_{photo} - I_{dark} \quad \textbf{(2.19)}$$

Figure 2.17a shows how I_{ph} varies as a function of the excitation wavelength for a monolayer MoS_2 FET. There is a clear change of 650 nm, near the monolayer MoS_2 bandgap. This is obvious since the generation needs to satisfy a basic condition, that is, the photon energy must be greater than the band gap of the material, which is 1.8 eV (in the monolayer). Only those photons with enough energy can promote electrons from the valence to the conduction band,

generating the photocurrent when a voltage between source and drain is applied.

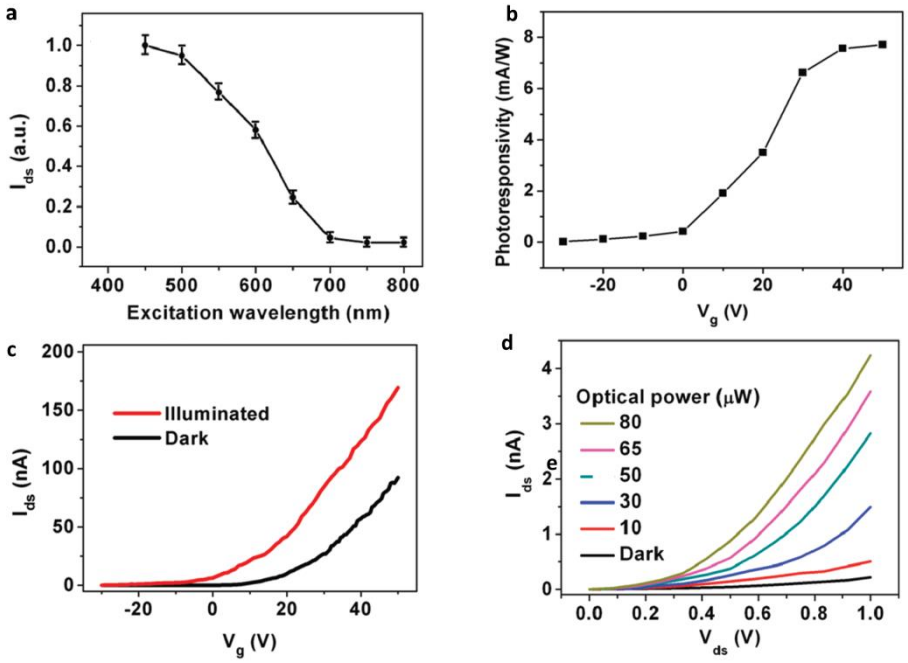

Figure 2.17: a Drain current as a function of different wavelengths. The current is negligible above 700 nm due to the monolayer bandgap at 1.8 eV (680 eV). Adapted from [18] **b** Photoresponsivity as a function of the gate voltage. In the ON state, the photoresponsivity is higher. Adapted from [18] **c** Drain current as a function of gate voltage under light and dark conditions. The current increases in the whole range under illumination, indicating that this mechanism dominates over thermionic or tunneling emission. Adapted from [18] **d** IV characteristic at different light powers. Adapted from [18]

One of the significant parameters to determine the performance of an optoelectronic device is the photoresponsivity (R), which is calculated using the following equation:

$$R = \frac{I_{photo} - I_{dark}}{P \cdot S} \tag{2.20}$$

Where P is the light incident power and S is the effective illuminated area. As Figure 2.17b R depends strongly on the gate voltage. As

mentioned before, measuring in the OFF state (lower voltage values) result in a deficient photocurrent extraction, and thus, a lower value of R. In the other hand, the extraction of the photocurrent in the ON state is more efficient, resulting in a higher value of R.

Figure 2.17c and 2.17d show the IV characteristic under different illumination conditions. It will be shown in greater detail in chapter 5, but it is important to mention how the electrical characterization varies with different light conditions. Figure 2.17c shows how the drain current under illumination is higher than that under dark conditions, dominating over thermionic and tunneling currents in the entire range. Figure 2.17d shows that the photocurrent is power dependent. As different studies show this dependency between photocurrent and incident power is linear [17-19].

2.3.2 Spectroscopic Techniques

2.3.2.1 Instrumentation

μ-Raman and μ-PL measurements were carried out in the free space set up shown in Figure 2.18a. The excitation source was a 488 nm Ar laser (Models Stellar-Pro 488/50 and Melles Griot). The input signals were collected by a Peltier cooled silicon EM-CCD detector (Andor Newton), passing through a 0.5 m diffraction spectrometer with a 1200 lines per mm diffraction grating. The laser beam is guided by a mirror system into an inverted scanning microscope stage shown in Figure 2.18b. This stage allows, in combination with a 10MHz Pulse Generator, to acquire μ-PL and μ-Raman spectroscopy maps with less than 500 nm of spatial resolution. 100 x 100 pixel mapping were obtained with an acquisition time of 1 second per pixel.

A scheme of the free space set up is shown in Figure 2.18c. The laser beam passes through a line filter (Semrock MaxLine Laser Line Filter LL01-488-25). This line filter eliminates higher (and lower) emission lines. The laser beam is guided through a mirror system and it is reflected off a dichroic filter with a cutoff at 488 nm (Semrock RazorEdge Dichroic LPD02-488RU). After that, the reflected beam goes

onto the sample. The emitted light (the result of the interaction between laser and sample), passes through the dichroic filter. Finally, the emitted light passes through a razor edge filter (Semrock RazorEdge LP02-488RU), filtering the small amount of Rayleigh scattering light reflected in the sample

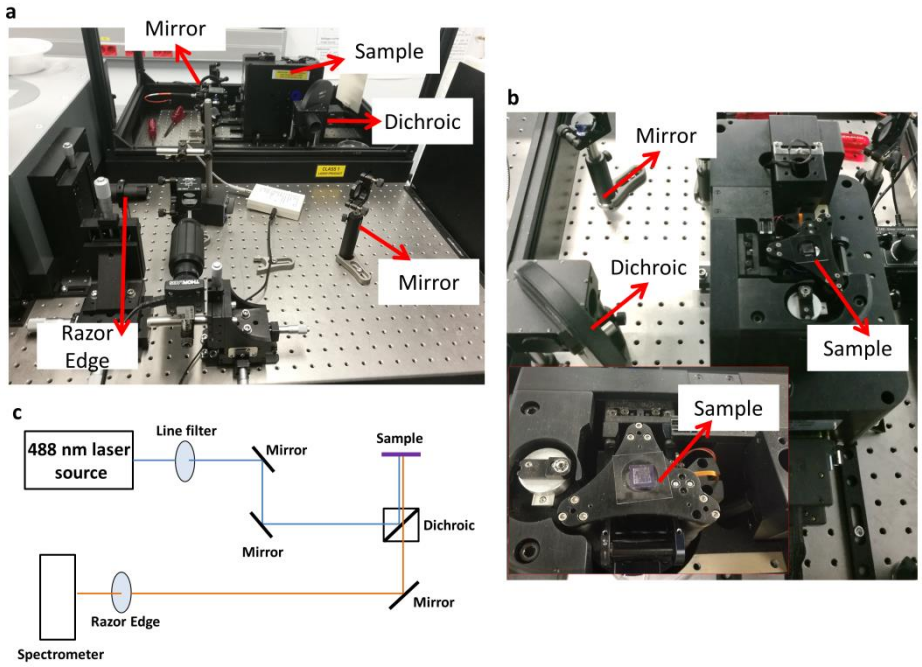

Figure 2.18: a Free space optical setup. **b** Piezo electric scanner used to locate the sample and (if desired) perform spectroscopic maps. **c** Schematic of free space optical setup and its components.

2.3.2.2 µ-Raman Spectroscopy

Raman spectroscopy is an optical characterization technique which is based on the inelastic scattering of light. It is used to observe vibrational, rotational or other frequency modes in a system. When light is scattered by matter, almost all the scattering is an elastic process (known as Rayleigh scattering) and the energy is conserved. However, a small percentage of scattering corresponds to an inelastic scattering process (the scattered light has a different energy from

incident light). When an inelastic scattering event occurs, a photon is released. This photon can have lower (Stokes scattering) or higher (Anti-stokes scattering) energy than the incident one, as the scheme shown in Figure 2.19 shows.

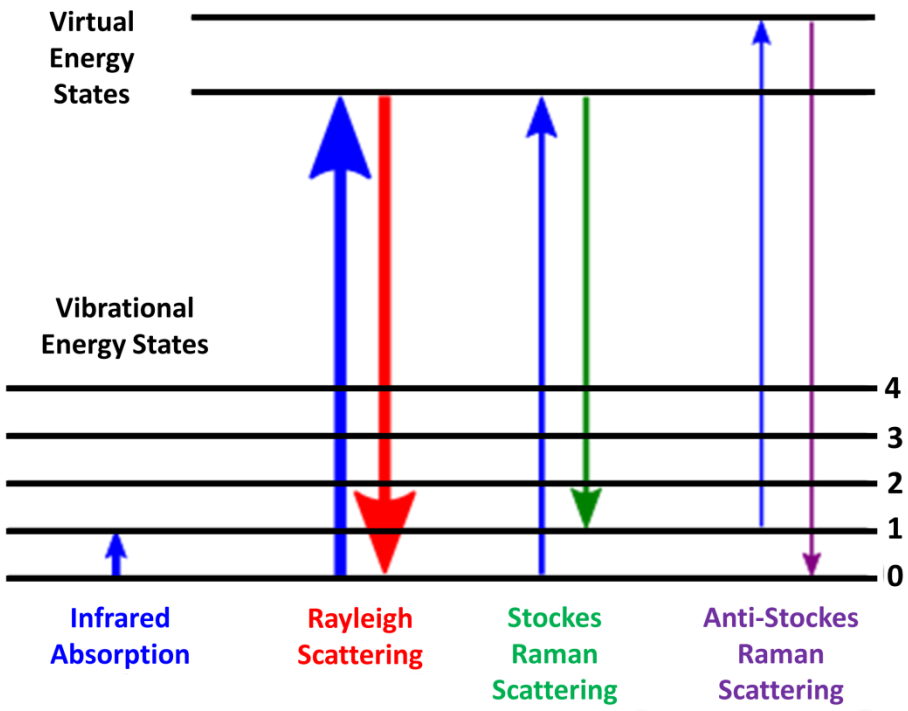

Figure 2.19: illustration of the Raman processes depending on the energy levels.

The Raman shift is expressed in cm^{-1} and it is given by

$$\Delta\omega = 10^7 \cdot \left(\frac{1}{\lambda_{exc}} - \frac{1}{\lambda_{Raman}}\right) \qquad \textbf{(2.21)}$$

where λ_{exc} and λ_{Raman} are the excitation and scattered photon wavelengths respectively, expressed in nm.

The Raman processes are related to phonons near the M and K points of the Brillouin zone. Figure 2.20a shows the phonon dispersion and the density of states (DOS) in a single-layer MoS_2. It has nine phonon branches. There are three acoustic modes. Those that vibrate in-plane (LA and TA) with a linear dispersion near Γ and the out-of-plane acoustic mode (ZA) [20, 21]. There are two optical modes at higher energies, corresponding with the excitation of zero-momentum phonons at the K point. Nonresonant MoS_2 Raman spectra consist of two main peaks: E^1_{2g} and A_{1g}. The in-plane E^1_{2g} mode results from opposite vibration of two S atoms with respects to the Mo atom while the A_{1g} mode is associated with the out of plane vibration of only S atoms in opposite directions (represented in the illustration of Figure 2.20b) [20]. The E^1_{2g} mode is centered around 383 cm^{-1} and the A_{1g} mode around 408 cm^{-1} as seen in Figure 2.20c. It is important to mention that due to the thickness dependency of the DOS, the Raman modes are also dependent as observed in Figure 2.20d [22]. This feature will allow identifying the number of layers as a function of the peak position difference (PPD), A_{1g}-E^1_{2g} (it is a qualitative measurement because Raman strongly depends on the optical parameters such as focus, laser intensity, etc.).

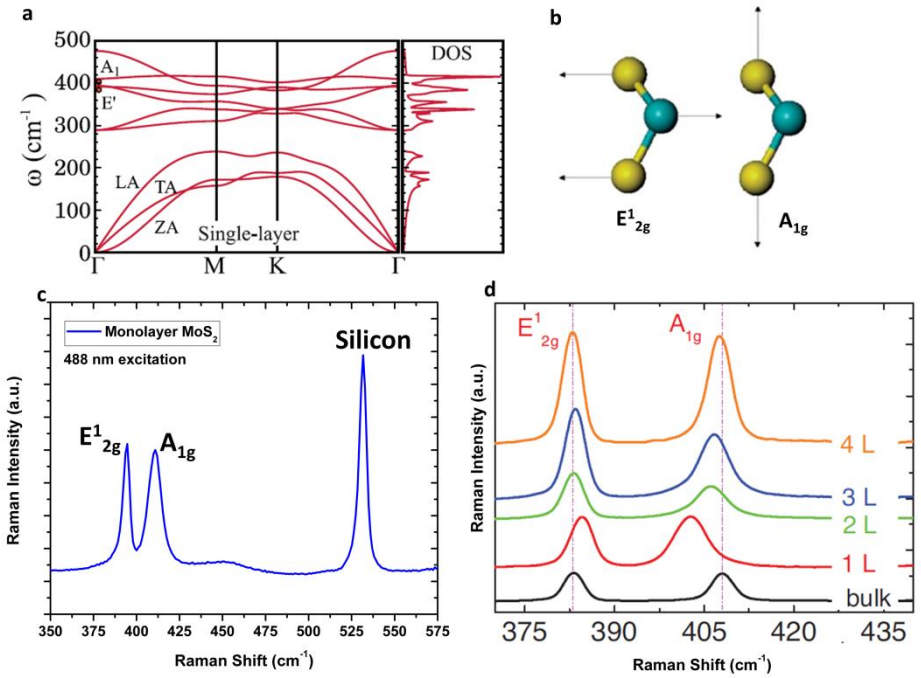

Figure 2.20: a Phonon dispersion and DOS in single layer MoS_2. Adapted from [20]. **b** Illustration showing the vibration of atoms for the two main MoS_2 Raman peaks. Adapted from [21]. **c** Typical Raman spectra for monolayer acquire in an exfoliated MoS_2 flake. The excitation wavelength was 488 nm. Acquisition time was 1 second. Apart from the characteristic peaks, Si peak can be observed at 525 cm^{-1}. **d** Raman spectra depending on the number of layers. The peak difference increases when the material becomes thicker. Adapted from [22].

2.3.2.3 µ-Photoluminescence Spectroscopy

Photoluminescence (PL) spectroscopy is a method that probes the electronic structure of materials. Light is directed onto a sample, where it is absorbed and photoexcitation can occur. The absorption of photons promotes an electron from the ground state to certain higher energy levels. The electron quickly relaxes and returns back to lower energy levels. The relaxation of the electron to lower energy levels can be through a non-radiative process, or by a radiative process by

emitting a photon. Light emission through this radiative process is known as PL. The process involved in MoS_2 PL is described in chapter 1 (section 1.2).

2.3.3 Microscopy Techniques

2.3.3.1 Atomic Force Microscopy

Atomic force microscopy (AFM) is a well-known characterization technique that is based on the interaction of the sample with a tip [23]. In this thesis, morphological and thickness measurements were carried out with an NTEGRA AFM acquired from the company NT-MDT Instruments[13]. All measurements were done in non-contact mode, a non-invasive AFM mode. The AFM lays on a Halcyonics_i4 active isolating system, ideal to eliminate the common noise induced by vibrations. HA_CNC Etalon series AFM tips were bought from NT-MDT Instruments[14]. They have a 1.5 N/m force constant and a resonant frequency of 66 KHz.

Figure 2.21a shows the AFM set up that has been used during this thesis. figure 2.21b corresponds with an AFM image of a MoS_2 flake decored with flowers. These flowers were made via PFEBIE, that will be described in the following chapter. It is possible to observe how the MoS2 flake presents different terraces. The left part of the flake corresponds with a monolayer (ML) of 0.7 nm and the right side corresponds with a 50 layer-thick flake (35 nm).

[13] https://www.ntmdt-si.com/products/modular-afm/ntegra-ii
[14] https://www.ntmdt-tips.com/products/view/ha-cnc

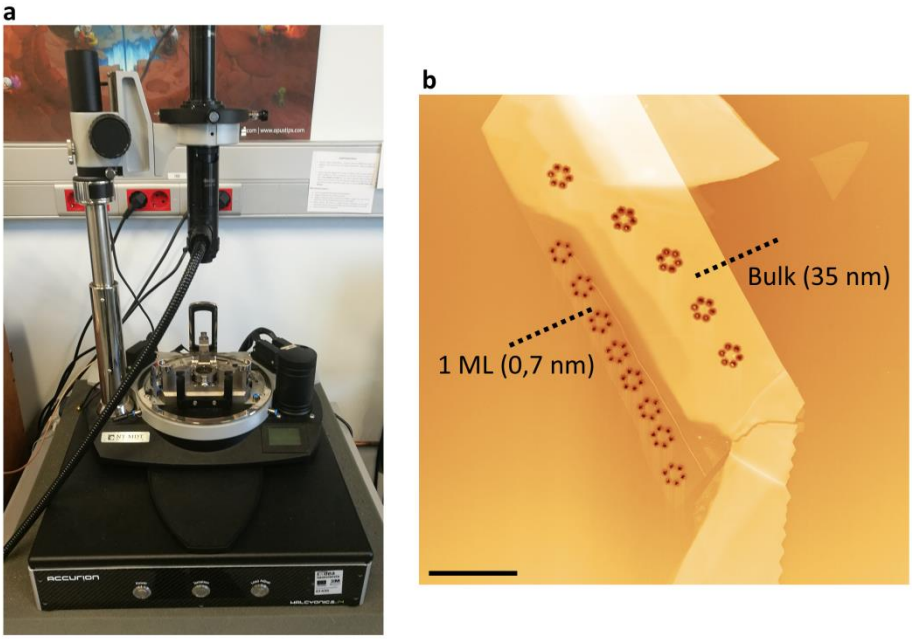

Figure 2.21: a AFM set up used for the characterization of this thesis. **b** AFM image a decored MoS_2 flake. Different terraces can be observed. The left part of the flake presents a monolayer of 0.7 nm, while the right side, corresponds with bulk MoS_2.

2.3.3.2 Scanning Electron Microscopy and Energy Dispersive X-Ray Spectroscopy

Scanning electron microscopy (SEM) is also a very studied characterization technique [24]. It uses an electron beam that interacts with the atoms in the sample producing different signals that contain information about the sample composition and the surface topography. In this thesis an Auriga UHD-SEM acquired from Carl Zeiss is used. The SEM is equipped with a Gas Injection System (described in section 2.2.2), a Focus Ion Beam (FIB) and a Scanning Transmission Electron Microscope (STEM). Although SEM has these features, only GIS was potentially used (apart from SEM images with different detectors such as secondary electrons detector, backscattered electrons detector and in-lens detector). SEM is also equipped with an

Elphy MultiBeam to perform the etching of different structures as described in chapters 4 and 5. Figure 2.22a corresponds with the equipment located in the clean room. Figure 2.22b shows an SEM image of a decored MoS_2 flake.

Energy Dispersive X-Ray Spectroscopy (EDX) is an analytical technique used for the elemental analysis of a sample. It is based on the interaction of a source of X-ray and the sample. The characterization is possible in large part due to the fundamental principle that each element has a unique atomic structure allowing a unique set of peaks on its electromagnetic emission spectrum. EDX measurements shown in chapter 4 were taken into a high definition SEM (EVO-HD bought from the company Carl-Zeiss[15]) equipped with a Peltier cooled EDS detector (Xflash 430 from Bruker), with 30 mm^2 detector area, 133 eV resolution and a working temperature of 40 K.

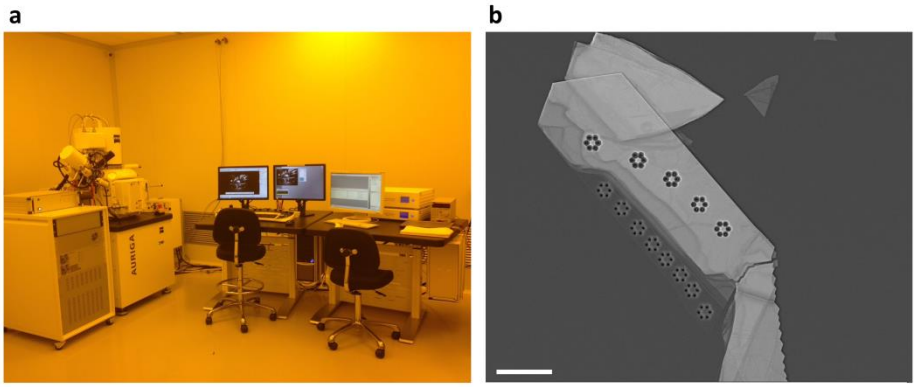

Figure 2.22: a Image of the UHD-SEM used in this thesis. **b** A secondary electron SEM image in the decored MoS_2 flake shown in Figure 2.21. Scale bar is 2 µm.

[15] https://www.zeiss.com/microscopy/int/products/scanning-electron-microscopes/evo.html

Bibliography

[1] K. S. Novoselov *et al.*, "Electric Field Effect in Atomically Thin Carbon Films" *Science,* vol. 306, no. 5696, p. 666, 2004.

[2] A. Castellanos-Gomez *et al.*, "Deterministic transfer of two-dimensional materials by all-dry viscoelastic stamping" *2D Materials,* vol. 1, no. 1, p. 011002, 2014.

[3] M. A. Meitl *et al.*, "Transfer printing by kinetic control of adhesion to an elastomeric stamp" Nature Materials, vol. 5, p. 33-38, 2005.

[4] E. Hecht, *Optics*. Pearson, 2002.

[5] S. M. Sze, *Semiconductor Devices. Physics and Technology*. Wiley, 2004, pp. 428-467.

[6] S. M. Sze, *Semiconductor Devices. Physics and Technology*. Wiley, 2004.

[7] Y. Huang, R. Dong, X. Zhu, and D. Yan, *Photo-responsive polymeric micelles* (Soft matter). 2014.

[8] A. E. Materials. "AZ® 1500 Photoresist."

[9] J. D. Musgraves, "Maskless Projection Lithography" Physics, Claremont University, 2003.

[10] F. https://en.wikipedia.org/wiki/Phenol_formaldehyde_resin, "Phenol formaldehyde resin" ed, 2012.

[11] F. https://en.wikipedia.org/wiki/Photoresist, "Photoresist," ed, 2017.

[12] A. Ortiz-Conde, F. J. García Sánchez, J. J. Liou, A. Cerdeira, M. Estrada, and Y. Yue, "A review of recent MOSFET threshold voltage extraction methods" *Microelectronics Reliability,* vol. 42, no. 4, pp. 583-596, 2002.

[13] N. B. Mansour, I. Najeh, S. Mansouri, and L. El Mir, "Effect of pyrolysis temperature on the properties of carbon/nickel nanocomposites prepared by sol–gel method" Applied Surface Science, vol. 337, pp. 158-165, 2015.

[14] B. Radisavljevic and A. Kis, "Mobility engineering and a metal–insulator transition in monolayer MoS2" Nature Materials, vol. 12, p. 815, 2013.

[15] T.-S. Ko, C.-C. Huang, and D.-Y. Lin, "Optical and Transport Properties of Ni-MoS2" *Applied Sciences,* vol. 6, no. 8, 2016.

[16] G. Acuna, *Far Field and Near Field Terahertz Spectroscopy on Parabolic Quantum Wells*. 2019.

[17] O. Lopez-Sanchez, D. Lembke, M. Kayci, A. Radenovic, and A. Kis, "Ultrasensitive photodetectors based on monolayer MoS2" Nature Nanotechnology, vol. 8, p. 497, 2013.

[18] Z. Yin *et al.*, "Single-Layer MoS2 Phototransistors" *ACS Nano,* vol. 6, no. 1, pp. 74-80, 2012.

[19] L. Jiao *et al.*, "Layer-dependent photoresponse of 2D MoS2 films prepared by pulsed laser deposition" *Journal of Materials Chemistry C,* vol. 7, no. 9, pp. 2522-2529, 2019.

[20] A. Molina-Sánchez, K. Hummer, and L. Wirtz, "Vibrational and optical properties of MoS2: From monolayer to bulk" Surface Sicence Reports, vol. 70, no. 4, pp. 554-586, 2015.

[21] L. Su, Y. Zhang, Y. Yu, and L. Cao, "Dependence of coupling of quasi 2-D MoS2 with substrates on substrate types, probed by temperature dependent Raman scattering" *Nanoscale,* vol. 6, no. 9, pp. 4920-4927, 2014.

[22] H. Li *et al.*, "From Bulk to Monolayer MoS2: Evolution of Raman Scattering" *Advanced Functional Materials,* vol. 22, no. 7, pp. 1385-1390, 2018/09/09 2012.

[23] G. Binnig, C. F. Quate, and C. Gerber, "Atomic Force Microscope" *Physical Review Letters,* vol. 56, no. 9, pp. 930-933, 1986.

[24] K. C. A. S. a. C. W. Oatley, "The scanning electron microscope and its fields of application" *British Journal of Applied Physics,* vol. 6, no. 11, p. 391, 1955.

Chapter 3: Pulsed Focused e-Beam Induced Etching

3.1 Introduction

Transition metal dichalcogenides (TMDCs), in particular, MoS_2, have attracted a lot of attention in the last years because of their outstanding optical and electrical properties. As discussed in chapter 1, the band structure is strongly thickness-dependent[1, 2]. This leads to a drastic change in its optical and electronic properties when changing its thickness from bulk to monolayer.

Although single-layer MoS_2 presents good optoelectronic behavior, it is necessary to locally control it in order to produce specific devices with emerging physical phenomena [3]. Different methods to modify these properties include inducing strain [4], using different substrates [5], or even fabricating TDMCs based heterostructures [6].

It is important to take into account that in this thesis the production method of the flakes is mechanical exfoliation. As discussed previously, this method produces very high-quality flakes [7]. In the other hand, there is a big dispersion in the geometrical factors of the samples. The size, geometry, and thickness of the flakes are difficult to control. For this reason, when fabricating a MoS_2 based device; the performance will vary and it will be difficult to standardize the fabrication method. In addition, when fabricating specific devices (i.e. hetero/homo-junctions, covered in chapter 5) a lot of fabrication steps are necessary. Firstly, standard fabrication is a basic condition. Then, the second process consists of different techniques, like aligning of the flakes, etching with a stencil mask, and so on.

For that reason, the goal of this chapter is to show how a new technique has been implemented to produce nanostructures in situ, without the need of a mask, saving intermediate fabrication steps and reducing the probability of damaging the devices.

Due to the chemical properties of MoS_2, it is difficult to etch it with common acids (nitric acid or sulphuric acid) or bases (KOH and NaOH) at room temperature [8]. For that reason, this chapter will cover a deep study of the chemical dry-etching technique, named Pulsed Focused e-Beam Induced Etching, PFEBIE. It will show the necessary equipment and working conditions. Then, the parameter space under study and the production of specific structures (i.e. dots, rings, holes, etc.) will be discussed. At the end of this chapter, it will be possible to see how the nanopatterning is used to tailor the geometry of the conduction channel of MoS_2 FETs and how it could fix an apparent problem of mechanical exfoliation.

3.1 Equipment and Working Conditions

PFEBIE is based on the combination of a focused electron beam and a constant flow of XeF_2. In order to conduct the assisted etching of the flakes, the samples are introduced in a Carl Zeiss Auriga workstation, comprising an electron and a gas injection system (GIS), as shown in chapter 2. To define the e-beam positions a 16 bit per channel pattern generator (400 MHz Raith multibeam).

The GIS consists of a nozzle system, whereby the etching gas is expelled. The nozzle used for the XeF_2 is placed 500 µm above the sample that is going to be etched. It has a size of 500 µm width and 500 µm height. The base vacuum at the chamber is 10^{-7} mbar and it rises to 10^{-5} when the XeF_2 is flowing. The parameter that guarantees a constant etchant pressure is the gas reservoir temperature, which is set at 10 °C. It prevents the gas to crystallize and it allows obtaining a

constant gas flow. The beam energy and current are 2.5 kV and 0.24 nA respectively. The aperture size is 30 µm.

Flakes are obtained by the mechanical cleavage method [7]. Once they are deposited on the desired substrate they are introduced in a Carl Zeiss Auriga workstation. Figure 3.1 shows the GIS coupled with the sample. Figure 3.1a shows a low magnification SEM image of the entire system. It is possible to observe the nozzle system, composed of 5 needles, each one specifically used for a different material. The one in the middle corresponds with the nozzle specific for the XeF_2 gas ejection. Figure 3.1b shows a zoom over the XeF_2 probe. This Figure shows how the probe is placed too close to the device/flake that is going to be etched.

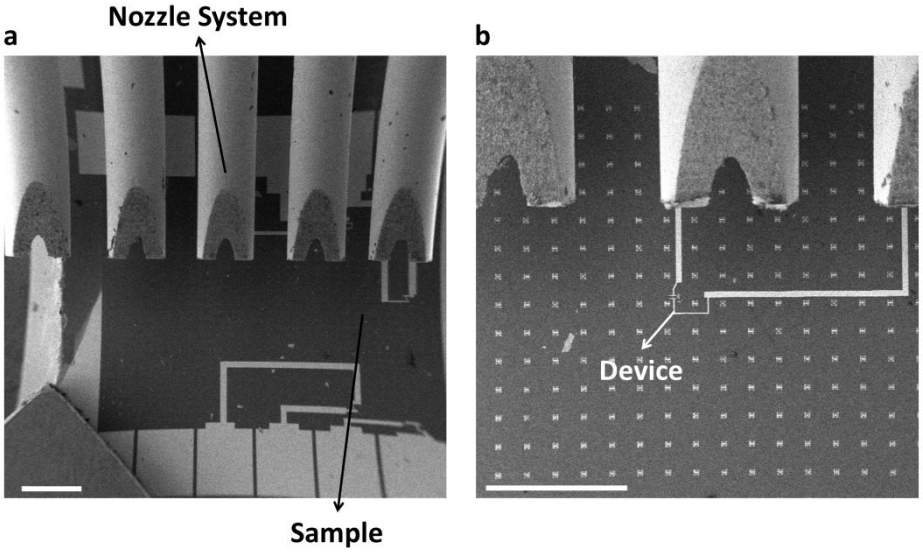

Figure 3.1: a SEM image of the GIS nozzle system close to the sample. Five different probes can be observed. The one in the middle corresponds with XeF_2. **b** Zoom taken in the XeF_2 probe. It is placed Scale bars are 500 µm.

3.3 Pulsed Focused e-Beam Induced Etching Parameter Space

Due to its highly oxidizing properties, XeF_2 is used in industry as an etching gas for Si. Previous works have shown that XeF_2 reactively etches MoS_2 at high-pressure conditions [8]. XeF_2 has also been used to modify the properties of graphene [9, 10].

The goal of this thesis is producing structures in situ, without the need of intermediate steps, as previously discussed. The etching is possible because the e-beam dissociates the gas mixture present in the sample surface. Xenon is a volatile compound that flies away. Due to the high chemical selectivity of fluorine with MoS_2 [11, 12], it will etch the flakes. There is a competition between different processes. First, the primary e-beam directly etches a very small portion of the flake. In the other hand, the secondary electrons could also take part in the etching mechanism. Depending on the energy of the beam, the pear of secondary electrons will be more prominent or not, affecting the etching. This second case corresponds with the diffusion limit, where the fluorine (F^- or F^{2-}) is repelled by the negatively charged secondary electrons. The more prominent the secondary electron pear, the higher will be the diffusion.

It is also possible to have spontaneously dissociated fluorine. In this case, the fluorine will migrate to the areas with lower chemical potential (the ones that are not filled with gas), etching spontaneously the MoS_2 surface.

This section will cover the parameter space of the technique. For that reason, different arrays of dots or rings will be fabricated. The study of the spot shape and size when varying the parameters will give information on the proper framework to use when designing more complex structures.

Figure 3.2 shows a scheme of the complete etching sequence. It is possible to observe that the etchant gas is flowing in the chamber while the e-beam is turned on and off. There are an important amount of parameters that are necessary to consider and will be cover in this section: the dwell time; the loop wait time; the number of loops and the number of layers of the exfoliated MoS_2 flake.

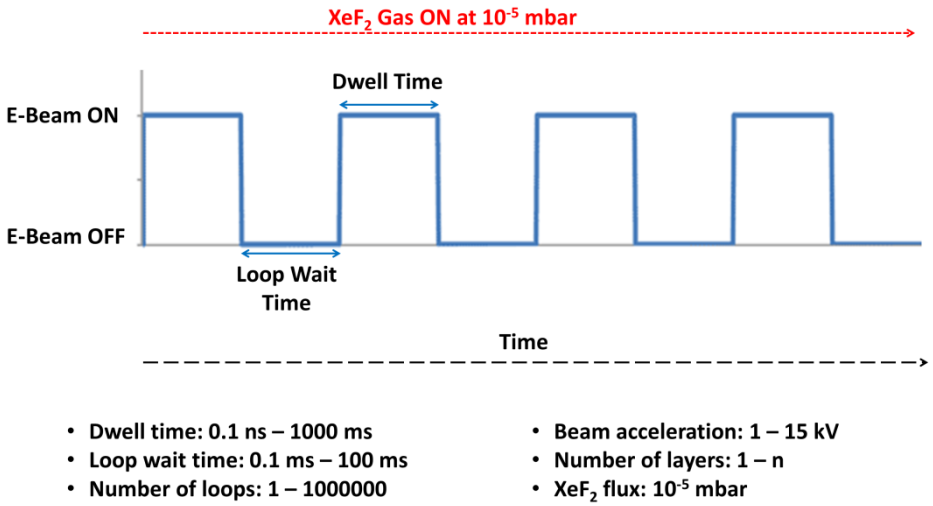

Figure 3.2: Scheme of the etching sequence. The XeF_2 gas is constantly flowing in the chamber at a pressure of $2.5x10^{-5}$ mbar while the e-beam is turned on and off. The lower part of the figure shows a summary of the parameter space, which will be covered in the following subsections.

3.3.1 Probe Distance

Firstly, the distance dependence was studied. 3x3 arrays of dots were fabricated at two different distances between the XeF_2 probe and the MoS_2 flake. It is important to mention that the rest of the variable parameters were maintained. Figure 3.3a shows the etching of a MoS_2 flake in a 3x3 array and at a probe-sample distance of 250 µm. It is possible to observe a hole-type geometry. Figure 3.3b shows an identical array at a distance of 500 µm. In this case, the geometry of the array has changed. A MoS_2 dot is observed in the central region.

This phenomenon can be explained in terms of the interacting electrons. For a smaller distance, the MoS_2 is etched mainly by the primary electrons, thus creating a hole-like shape. In the other hand, for higher distances, the secondary electrons create a central pillar in each etched structure. As Figure 3.3c shows, for higher nozzle-sample distances; the XeF_2 will be dissociated by the secondary electrons. In this case, the etching will be dominated by the diffusion of the fluorine, while the central region will be protected.

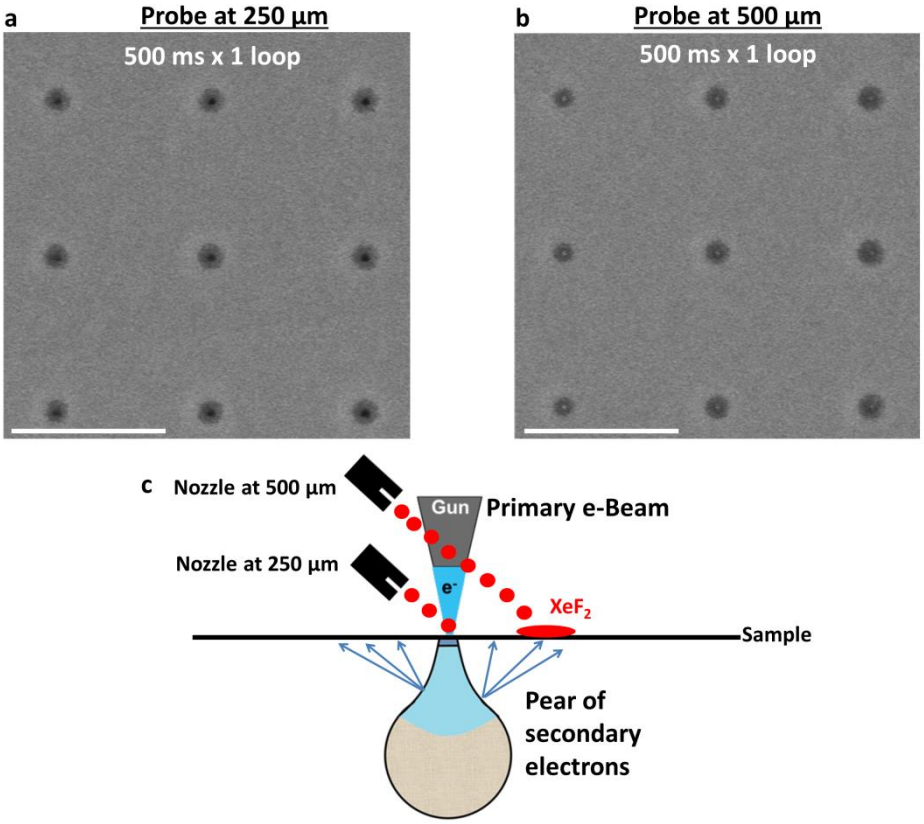

Figure 3.3: a 3x3 array of MoS_2 dots at a distance of 250 µm. A central hole is observed in all the etched structures. At this distance, MoS_2 will be etched by the primary electrons. **b** An identical array at a distance of 500 µm. A central MoS_2. pillar is observed. In this case, the etching is dominated by the diffusion limit. **c** Scheme of the etching mechanism and the interacting electrons in the etching process. Scale bars are 500 nm.

There is also an important effect in astigmatism depending on the nozzle distance. Astigmatism affects drastically on the etching shape and quality. The nearer the nozzle is, the higher astigmatism. For that reason, it is important to reach a compromise in the nozzle-sample distance and the astigmatism correction. Due to that, the distance that is used to etch the MoS_2 was set at 500 µm.

3.3.2 Dwell Time

This subsection will study the effect of the dwell time. For this reason, the number of loops will be constant. Figure 3.4a shows a 10x10 array of dots. The number of loops was set at 1. Each row of the array corresponds with different dwell time, starting at 100 ms. The last row corresponds with 1 s of dwell time. It is possible to observe that the size of the central pillar increases when increasing the dwell time, as shown in Figure 3.4b. The etched ring also increases. The pillar and etched ring diameter scale with the dose, which is proportional to the dwell time.

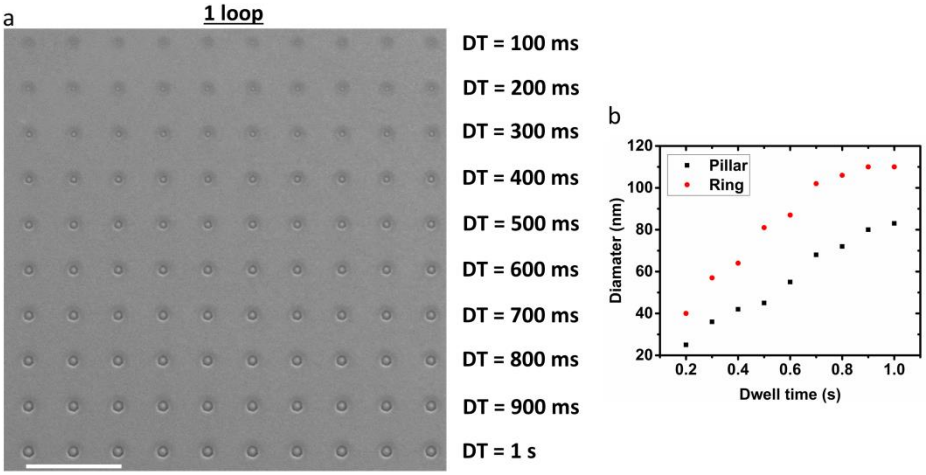

Figure 3.4: a Dwell time (DT) variation at a fixed number of loops. As dwell time is increased, the size of the inner pillar and the etched ring increase Scale bar is 1 µm. **b** Diameter of the interior and exterior etched regions as a function of the DT.

This observation could be explained again by the competition between primary and secondary electrons. For shorter dwell times, the etching is governed by the primary electron beam. As a consequence, there is practically no central pillar. For longer dwell times, the mechanism is governed by the diffusion limit and the secondary electrons are responsible for the etching. For that reason, at longer DTs more secondary electrons participate, molecules have more time to interact with them and the central pillar and the etching ring are larger.

3.3.3 Number of Loops

Distinct from the previous subsection, the dwell time will be fixed while the number of loops will vary. Figure 3.5 shows two experiments where the dwell time is fixed at 100 and 500 ms and the number of loops is modified in each row. Figure 3.5a corresponds with the experiment at 100 ms of dwell time. For this duty cycle (100 ms of dwell time and 50 ms of waiting time) the etchant replenishes the whole MoS_2 surface in between cycles, and the primary beam etches a bit of the central dot in each cycle. This phenomenon is more pronounced when the number of loops is higher, and the central pillar completely disappears. If the dwell time is longer, as shown in Figure 3.5b, the diameter of the etched region increases, while the central pillar remains almost constant. As the DT is higher, the beam is ON longer time. The repulsion is more pronounce and the central pillar is protected, while the etched ring widens by increasing the number of loops. Figure 3.5c shows the diameter of the central pillar and the etched rings for both dwell times. It is possible to observe how for a DT of 100 ms, the diameter of the etched ring increases with the number of loops, while the central pillar disappears. In the other hand, for a DT of 500 ms, the central pillar is almost constant, while the etched ring increases with the number of loops.

Figure 3.5 also shows that the structures have an unmistakable hexagonal geometry. There are six preferential in-plane etch directions related to the MoS_2 atomic structure that leads to the

formation of six etching fronts. In this diffusion regime, the etching is no longer isotropic and this leads to the formation of these hexagonal-shaped structures with a central pillar of MoS_2. The anisotropic etching can be explained with the fact that the zig-zag edges in the MoS_2 lattice are more easily etched than the armchair edges, as previously reported [13, 14].

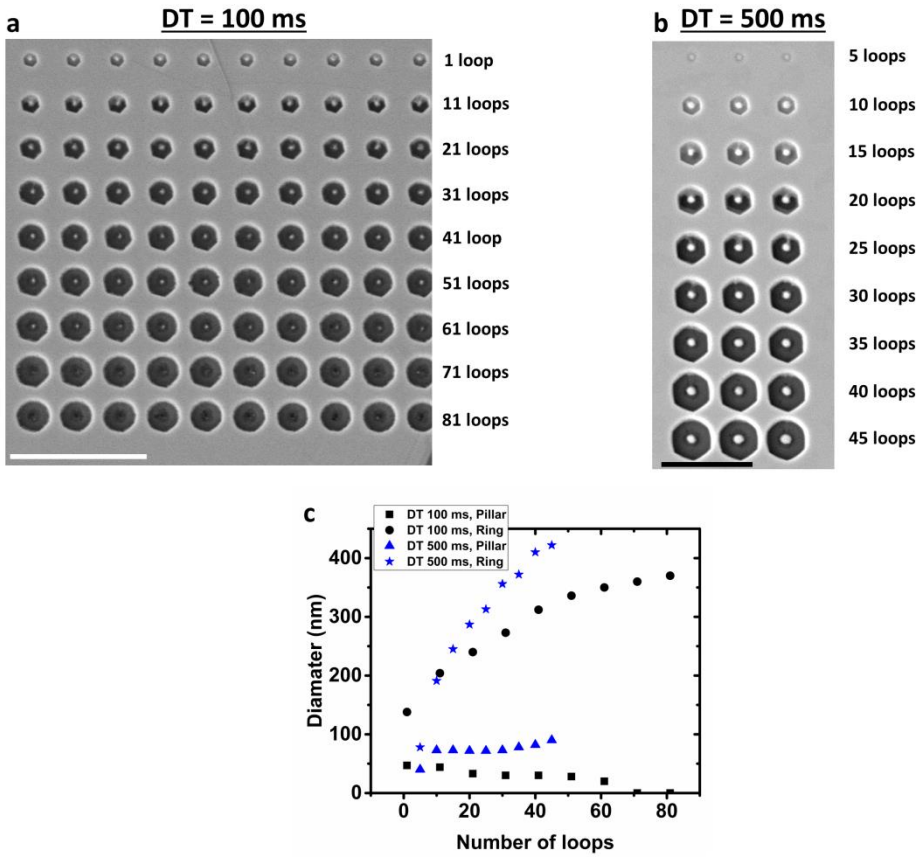

Figure 3.5: a Variation of the number of loops at a dwell time of 100 ms. As the number of loops increases, the diameter of the etched ring also increases, while the central pillar decreases. **b** Variation of the number of loops at a longer dwell time. In this case, the diameter of the etched region increases with the number of loops, while the central dot remains mainly constant. Scale bars are 1 µm.

3.3.4 Fly Time and Patterning Strategy

Sometimes there are some artifacts that can affect the etching of MoS_2 structures. For this reason, this subsection will cover which could be the best strategy to perform correct tailoring of MoS_2 flakes.

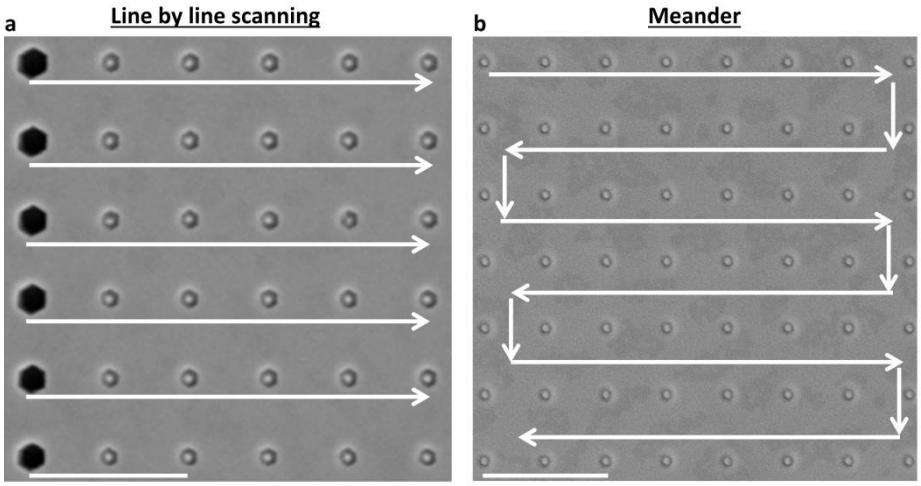

Figure 3.6: a Example of a line by line scanning. The first structure of each row clearly differs from the rest of the MoS2 pillars. This is explained by the fly time, attributed to diffusion effects. In the beginning, there is more fluorine at the surface, increasing the etching in the whole structure. **b** Meander-like scanning. The fly-time effect is clearly reduced and all the structures are identical. Scale bars are 1 µm.

Figure 3.6 shows two different patterning strategies. The arrows of this Figure indicates the direction of the scanning Figure 3.6a corresponds with a line by line scanning, while Figure 3.6b coincides with a meander-like scanning. Figure 3.6a clearly shows that the first feature of each row is totally different. Instead of having a pillar-like shape, the central region is completely etched. When a line-by-line scanning is made, the beam is turned off at the end of each scanning row. This allows the molecules to fill the whole surface. For that reason, at the beginning of the next row, the amount of etchant gas is

higher, and the etching rate is also higher. This effect is more pronounced when the scanning is longer because the time that the beam takes to go to the first point of the following row is higher and the amount of gas is larger.

In the other hand, when a meander strategy is chosen (defined by the arrows shown in Figure 3.6b), the beam is always turned. For that reason, the total amount of XeF2 is constant and the etching rate is uniform, as shown in Figure 3.6b.

3.3.5 MoS_2 Flake Thickness

As mentioned before, exfoliation produces flakes with different thicknesses. For this reason, it is important to study how the thickness can affect the etching mechanism. This section will cover how the etching mechanism changes with thickness for the same tailoring conditions.

Figure 3.7 shows an example of how the flake thickness can affect the etching. The left hexagonal array corresponds with patterning in a thin region of the flake (4 layers, as shown in the inset of figure 3.6). The right MoS_2 array coincides with a patterning under the same conditions, in a thicker region of the same flake (around 25 layers, as shown in the inset of Figure 3.7). It is possible to observe that, the thickness plays an important role. The geometry of each dot clearly depends on the MoS_2 thickness. The accumulated charge could play an important role. In the thinner region of the flake shown in Figure 3.7 there is not accumulated charge taking place and the repulsion between molecules and electrons is negligible. Accordingly, the total exposed volume will be etched, including slightly the substrate, as seen in the central regions of the left array of Figure 3.7. In the other hand, the right hexagonal array shows that the central pillar is present in all the regions. The thicker part of the MoS_2 flake accumulates negative charge, of the incoming electrons. For that reason, the

molecules are repelled from the central region and thus, creating the central pillar.

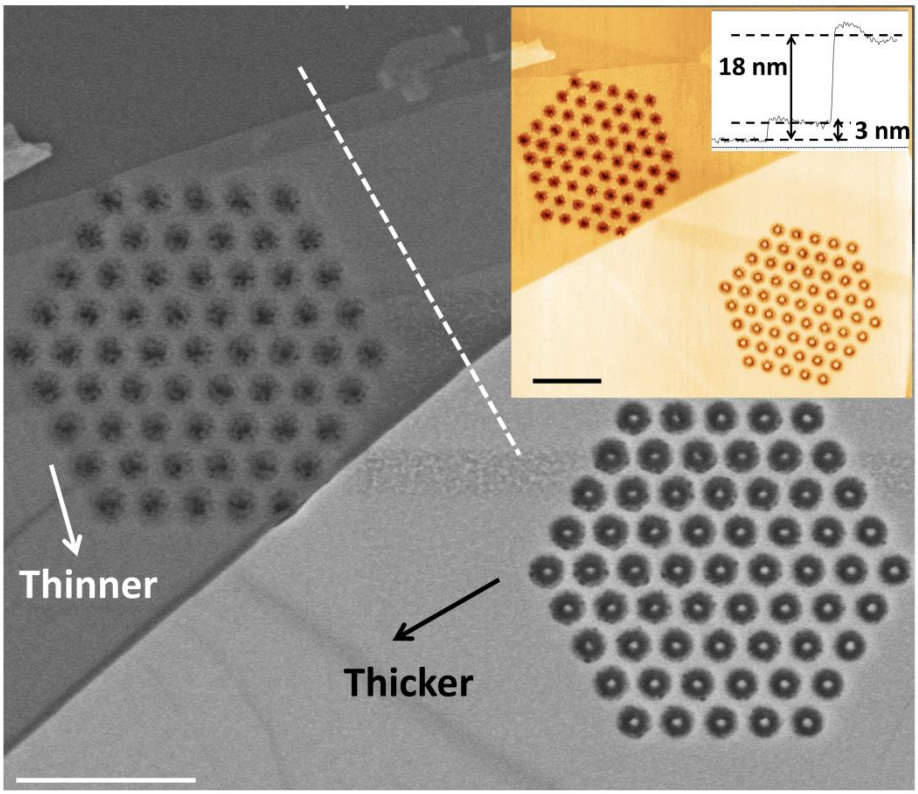

Figure 3.7: Two different arrays in the same MoS_2 flake, with different thicknesses. The left hexagonal array corresponds with a thinner part of the flake (less than 10 layers). The right hexagonal array corresponds with a thicker region (more than 10 layers). For thinner regions, the distribution of secondary electrons is reduced and the pillar will be etched. The inset shows an AFM image of the same arrays, showing the height profile (taken in the dashed line region). The thinner part has a height of 3 nm (4 layers), while the thicker part is 18 nm height (25 layers). The Scale bars are 1 μm.

With that in mind, it is important to take into account that, flakes with different thickness, can affect the etching process. It would be great if large area and uniform flakes could be obtained, but the exfoliation process is not the best production method for this porpoise. This

change in thickness affects the electric performance of the devices due to the misalignment of the band structure. Following sections will show how PFEBIE could be used to modify different thickness FETs, and how one of the exfoliation problems can be solved.

3.3.6 Dose Plateaus

As the whole section has demonstrated, there are different parameters that can affect the tailoring mechanism. Nonetheless, there is a dose plateau in which, for a given set of parameters (beam kV, beam current, thickness, etc.), geometries are the same for a given dose regardless of the duty cycle as shown in Figure 3.8.

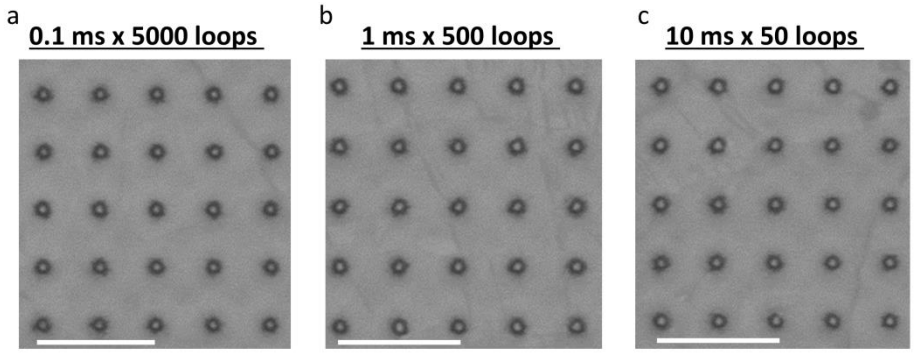

Figure 3.8: Three arrays with different duty cycles, at a constant dose. There is a dose plateau for a given set of parameters (thickness, beam kV and beam current), regardless of the different duty cycles. Scale bar is 1 µm.

3.4 Fabrication of different geometries

As explained in the introduction of this chapter, there is a big effort in producing specific electronic devices. For this reason, PFEBIE could be used to modify the geometry of MoS_2 devices and induce new physical phenomena. This section will show different MoS_2 geometries,

fabricated with PFEBIE. Figure 3.9 shows three examples of geometry tailoring, all of them from a previously fabricated MoS_2 FET. Figures 3.9a and 3.9b correspond with two exotic structures in which additional physical phenomena could appear, like changes in the MoS_2 phase and magnetic properties when reducing the size to tens of nm. Recent studies show that MoS_2 ribbons are potential candidates for spintronics or magnetic devices [15-18]. Figure 3.9a shows a MoS_2 zig-zag ribbon structure. Other technological applications are related to biological operations. MoS_2 devices can be used as biological sensors or for bioimaging operations [19-21]. This biotechnology is possible to achieve by using MoS_2 dots and tuning the photoluminescence of the devices. Figure 2.9b shows a MoS_2 dot of 40 nm surrounded by two MoS_2 wires. Future work could cover a deep characterization of these devices collaborating in an interdisciplinary atmosphere.

Figures 3.9c and 3.9d shows another example of tailoring a MoS_2 FET, which is also present in chapter 4. Figure 3.9c corresponds with a MoS_2 FET with three different thicknesses (due to the exfoliation mechanism). This thickness variation affects the electric performance of the device because the density of states is not uniform along with the material. For this reason, PFEBIE was used to alter the geometry, as shown in Figure 3.9d. After the patterning, the device has only one thickness, simplifying the device performance, an fixing one of the exfoliation problems: random and variable flake thicknesses. This particular example along with other structures will cover chapter 4 which will focus on using PFEBIE to alter the conduction channel of MoS_2 FET and study the consequences that this method has over the optoelectronic properties.

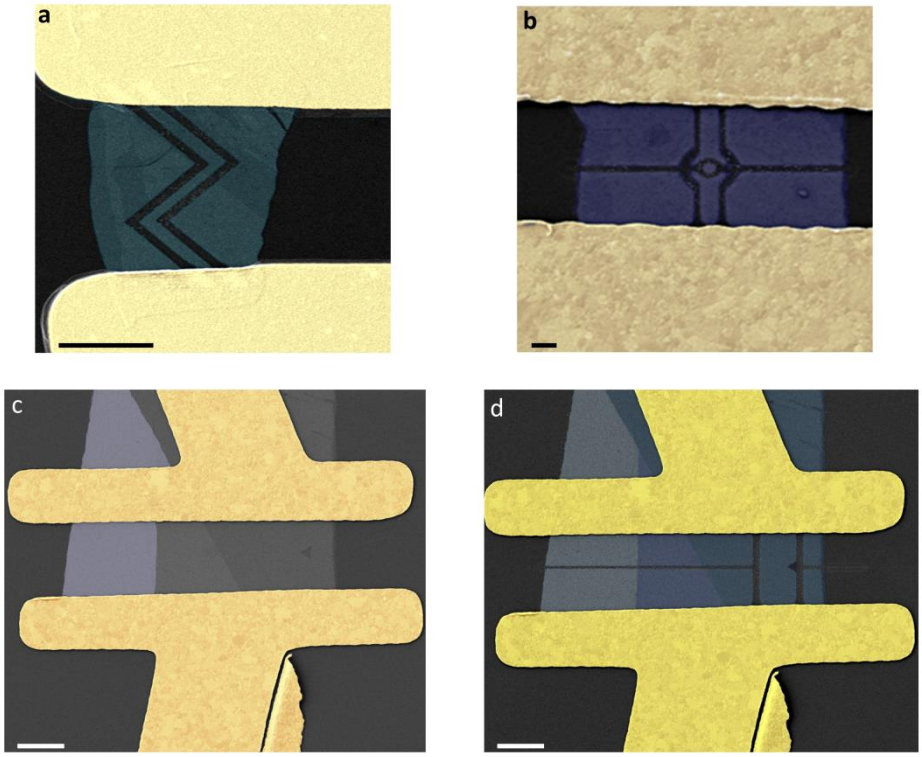

Figure 3.9: False-color SEM images of different geometries fabricated from a MoS_2 FET. PFEBIE conditions were: 2.5 kV of beam energy,0.24 nA of beam current, 30 µm aperture, 250 loops, DT of 500 ns. **a** Zig-zag wired structure. Scale bar is 2 µm. **b** A MoS_2 dot of 40 nm surrounded by two MoS_2 wires. Scale bar is 50 nm. **c and d** Example of how PFEBIE can be used to fix the thickness variation problem of mechanical exfoliation. In this case, the thicker regions of the FET were etched and only one region remains unaltered. Scale bars are 2 µm.

3.6 Comparison with other Techniques

Coburn and Winters established the bases of beam-based etching [22], where the chemical reactions enhanced by radiation were studied. PFEBIE is based on this kind of method. Nonetheless, it presents an advantage, related to the fabrication time. In the case of the

fabrication of the devices shown in section 3.4 and in chapters 4 and 5, the dwell time is more than two orders of magnitude lower than in previous studies [23]. For this reason, PFEBIE allows the tailoring of several devices in less than 1 hour of the e-beam round. Typically, it allows tailoring a device in less than 2 minutes.

It is true that interacting ion beam methods also allow the fabrication of these structures. In the other hand, PFEBIE is a much accessible technique due to the cost of the required equipment. Most of the clean rooms are equipped with an SEM. In addition, the coupling of a Gas Injection System (GIS) like the one is described in chapter 2 is relatively cheaper compared with the ion beam systems. For that reason, PFEBIE is as an alternative and a cheaper tool for prototype production.

It is also important to emphasize that the beam energy of PFEBIE is much lower than the used in ion beam etching. In our case, the beam energy is 2.5 KeV, while the beam energy used in ion beam etching is in the order of is 30 KeV [23]; more than 10 times higher than ours. This change in the energy could produce changes in the atomic structure and in the chemical composition of the sample. The comparison with the ion beam want to remark that PFEBIE is based on a chemical method, while interacting ion beam etching is more similar to sputtering, that could increase the physical damage probability or distortion of the lattice.

In the case of lithography-based methods, it is true that they allow characterization before/after material tailoring. Nonetheless, it is important to take in mind that, everybody working in a clean room, knows how difficult several fabrication steps are. They present a huge amount of different phases that can alter or simply destroy the device, decreasing the fabrication yield. Accordingly, PFEBIE is a straightforward fabrication method that clearly simplifies the whole fabrication procedure.

3.6 Conclusions

This chapter has presented a nanopatterning method that allows modifying MoS_2 flakes. First of all, a study of the parameter space was carried out, searching which are the best fabrication conditions. After exploring this space, a dose plateau was found, in which the obtained geometries did not vary regardless of the duty cycle.

Secondly, MoS_2 areas were fabricated with high accuracy. Accordingly, the etching parameters were optimized to improve the device fabrication time. The dwell time is 500 ns and the number of loops was set at 250. The last part of this chapter provides a comparison between different beam-based fabrication methods, in which the fabrication time and the damage of the devices are higher than in PFEBIE. A comparison with other clean room techniques was also mentioned, emphasizing in the tedious sequence that it is necessary to follow. With that, PFEBIE has been demonstrated to be a useful nanopatterning technique that can save intermediate fabrication steps and decrease the damage of the samples.

Bibliography

[1] K. F. Mak, C. Lee, J. Hone, J. Shan, and T. F. Heinz, "Atomically Thin MoS2: A New Direct-Gap Semiconductor" *Physical Review Letters,* vol. 105, no. 13, p. 136805, 2010.

[2] A. Splendiani *et al.*, "Emerging Photoluminescence in Monolayer MoS2" *Nano Letters,* vol. 10, no. 4, pp. 1271-1275, 2010.

[3] M. G. Stanford, P. D. Rack, and D. Jariwala, "Emerging nanofabrication and quantum confinement techniques for 2D materials beyond graphene" vol. 2, no. 1, p. 20, 2018.

[4] A. Castellanos-Gomez *et al.*, "Local Strain Engineering in Atomically Thin MoS2" *Nano Letters,* vol. 13, no. 11, pp. 5361-5366, 2013.

[5] M. Buscema, G. A. Steele, H. S. J. van der Zant, and A. Castellanos-Gomez, "The effect of the substrate on the Raman and photoluminescence emission of single-layer MoS2" *Nano Research,* vol. 7, no. 4, pp. 561-571, 2014.

[6] R. Frisenda, A. J. Molina-Mendoza, T. Mueller, A. Castellanos-Gomez, and H. S. J. van der Zant, "Atomically thin p–n junctions based on two-dimensional materials" *Chemical Society Reviews,* vol. 47, no. 9, pp. 3339-3358, 2018.

[7] K. S. Novoselov *et al.*, "Two-dimensional atomic crystals" *Proceedings of the National Academy of Sciences of the United States of America,* vol. 102, no. 30, p. 10451, 2005.

[8] Y. Huang *et al.*, "An innovative way of etching MoS2: Characterization and mechanistic investigation" *Nano Research,* vol. 6, no. 3, pp. 200-207, 2013.

[9] M. A. Ribas, A. K. Singh, P. B. Sorokin, and B. I. Yakobson, "Patterning nanoroads and quantum dots on fluorinated graphene" Nano Res., vol. 4, no. 1, pp. 143-152, 2011.

[10] F. Withers, M. Dubois, and A. K. Savchenko, "Electron properties of fluorinated single-layer graphene transistors" *Physical Review B,* vol. 82, no. 7, p. 073403, 2010.

[11] C.-S. Kim, S.-H. Ahn, and D.-Y. Jang, "Review: Developments in micro/nanoscale fabrication by focused ion beams" *Vacuum,* vol. 86, no. 8, pp. 1014-1035, 2012.

[12] D. Xia, J. Notte, L. Stern, and B. Goetze, "Enhancement of XeF2-assisted gallium ion beam etching of silicon layer and endpoint detection from backside in circuit editing" *Journal of Vacuum Science & Technology B,* vol. 33, no. 6, p. 06F501, 2018/05/08 2015.

[13] J. Wu *et al.*, "Layer Thinning and Etching of Mechanically Exfoliated MoS2 Nanosheets by Thermal Annealing in Air" *Small,* vol. 9, no. 19, pp. 3314-3319, 2019/05/05 2013.

[14] M. Yamamoto, T. L. Einstein, M. S. Fuhrer, and W. G. Cullen, "Anisotropic Etching of Atomically Thin MoS2" *The Journal of Physical Chemistry C,* vol. 117, no. 48, pp. 25643-25649, 2013.

[15] C.-H. Lee, J. Lin, and C.-K. Yang, "Armchair MoS2 nanoribbons turned into half metals through deposition of transition-metal and Si atomic chains" Scientific Reports, vol. 8, no. 1, p. 13307, 2018.

[16] H. Pan and Y.-W. Zhang, "Edge-dependent structural, electronic and magnetic properties of MoS2 nanoribbons" *Journal of Materials Chemistry,* vol. 22, no. 15, pp. 7280-7290, 2012.

[17] H. Pan and Y.-W. Zhang, "Tuning the Electronic and Magnetic Properties of MoS2 Nanoribbons by Strain Engineering" *The Journal of Physical Chemistry C,* vol. 116, no. 21, pp. 11752-11757, 2012.

[18] H. Simchi, M. Esmaeilzadeh, H. Mazidabadi, and M. Norouzi, "*Tunable spin transport using zigzag MoS2 nanoribbon"*. Arxiv, 2014.

[19] N. S. Arul and V. D. Nithya, "Molybdenum disulfide quantum dots: synthesis and applications" *RSC Advances,* vol. 6, no. 70, pp. 65670-65682, 2016.

[20] W. Dai *et al.*, "Tunable Fabrication of Molybdenum Disulfide Quantum Dots for Intracellular MicroRNA Detection and Multiphoton Bioimaging" *Small,* vol. 11, no. 33, pp. 4158-4164, 2019/05/05 2015.

[21] H. Lin, C. Wang, J. Wu, Z. Xu, Y. Huang, and C. Zhang, "Colloidal synthesis of MoS2 quantum dots: size-dependent tunable photoluminescence and bioimaging" *New Journal of Chemistry,* vol. 39, no. 11, pp. 8492-8497, 2015.

[22] J. W. Coburn and H. F. Winters, "Ion‐ and electron‐assisted gas‐surface chemistry—An important effect in plasma

etching" *Journal of Applied Physics,* vol. 50, no. 5, pp. 3189-3196, 2018/05/08 1979.

[23] D. S. Fox *et al.*, "Nanopatterning and Electrical Tuning of MoS2 Layers with a Subnanometer Helium Ion Beam" *Nano Letters,* vol. 15, no. 8, pp. 5307-5313, 2015.

Chapter 4: Tailoring the optoelectronic properties of MoS_2 FETs

4.1 Introduction

As described in chapters 1 and 2, mechanical exfoliation has the advantage of producing very high-quality flakes. In the other hand, exfoliation does not allow producing large area films and the material usually has many thicknesses. Due to the band gap dependence with thickness, the electrical and optical properties strongly depend on the number of layers present in the flake. In addition, it is difficult to tailor the conduction channel once a device has been fabricated, involving many fabrication steps and increasing the damage probability. Accordingly, this chapter is concentrated in the modification of the channel geometry of MoS_2 based FETs with PFEBIE. The consequences that this technique has over the optoelectronic properties of the devices will be described, using the characterization techniques that were described in chapter 2.

4.2 FET channel modification

Figure 4.1 shows an example of a tailored device via PFEBIE. In this case, the initial MoS_2 FET had different thicknesses due to the exfoliation process as shown in Figure 4.1a. This thickness variation could affect electrical properties. Due to the dependency of the density of states with the thickness, the electric behavior of the MoS_2 device will be affected strongly by the alignment of the electrode-MoS_2 bands. The contact area between the flake and the electrodes is different between those zones, making difficult to interpret the transfer characteristics. In addition, optical properties will vary due to

the thickness dependence, and optoelectronic mechanisms such as photocurrent will be impossible to understand. For that reason, PFEBIE was employed to tailor the geometry of the initial device. In this example, the thicker part of the device was etched in a cross-bar section to avoid electrical conductivity. Figure 4.1b shows the tailored device. The thinner part of the device was tailored to allow the current pass through.

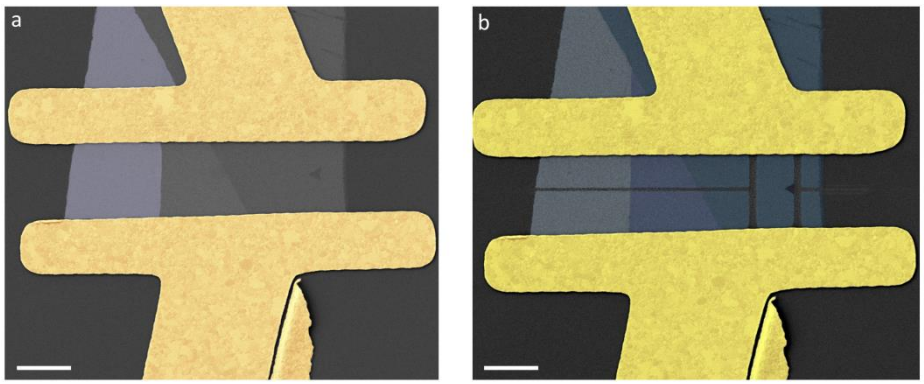

Figure 4.1: a Initial MoS_2 FET. A three-layer device is observed in the SEM image. **b** Tailored device. The thinner part was etched in wire-type geometry. The thicker parts of the device were etched to avoid electrical conductivity. Scale bars are 2 µm

It was possible to observe different geometries in chapter 3. Along with this chapter, PFEBIE will be utilized to fabricate wire-type geometries. This kind of geometry will simplify the analysis of the IV transfer characteristics and the calculation of the FET parameters, such as mobility, where geometrical factors are decisive.

Figure 4.2 shows another example of PFEBIE. The device was again tailored in a wire-type geometry. Figure 4.2a and 4.2b correspond with SEM images of the devices before and after the patterning respectively. In addition to SEM images, AFM was performed to study how much the silicon and the device were etched. Figure 4.2c and 4.2d show AFM characterization of the device shown in Figure 4.2a and 4.2b respectively. The insets represent the height profiles of the sample. Before PFEBIE the device thickness is 2 nm. Taking into account that the monolayer is 0.7 nm thick [1], the device shown in Figure 4.2c corresponds with a 2-3 layer flake. After the patterning, the profile shown in Figure 4.2d indicates that on the area exposed to

the treatment, the SiO_2 is etched approximately 15 nm under the exposure conditions. Moreover, the thickness of the remaining MoS_2 has increased to 5 nm after PFEBIE. This increase in height after PFEBIE will be discussed in the following sub-section.

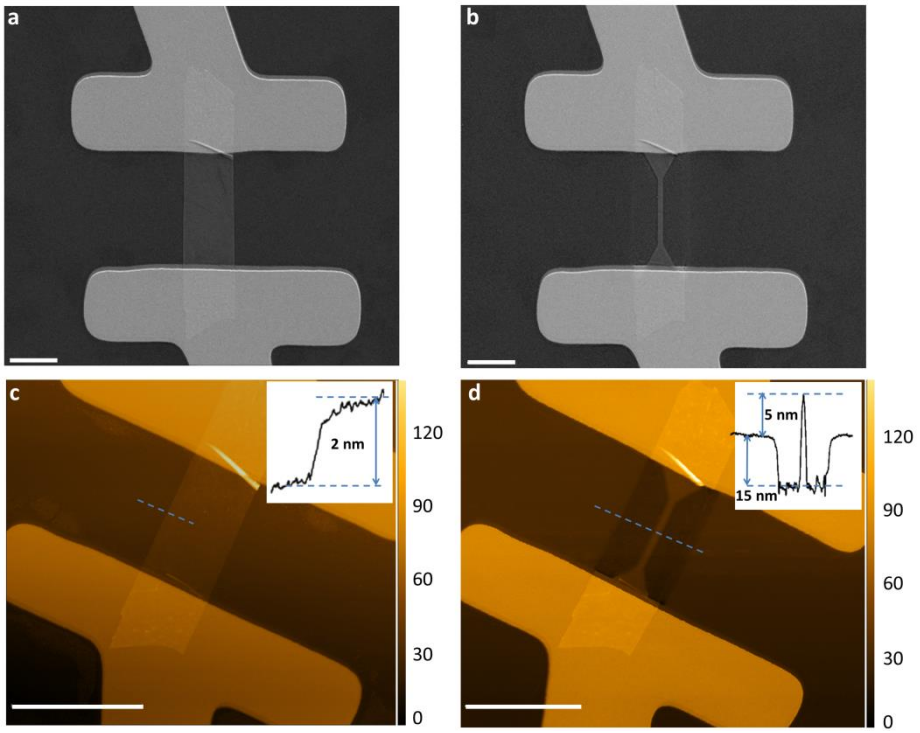

Figure 4.2: a SEM image of the device before the patterning. **b** SEM image of the device after the patterning, showing a 250 nm width channel. Scale bars are 2 µm. **c** AFM image of the device before the patterning. Inset shows a high profile of the flake, corresponding with a 2-3 layer thick MoS_2 flake. **d** AFM image after the patterning showing that the height has increased to 5 nm and the SiO_2 was etched 15 nm. Scale bars are 4 µm.

4.2.2 Energy-Dispersive X-ray Spectroscopy and Backscattered Electrons Characterization

To study the origin of the increase in height shown in Figure 4.2, energy-dispersive X-Ray (EDX) spectroscopy before and after PFEBIE was performed. A variable pressure High-definition SEM (EVO-HD from Carl-Zeiss) was used, equipped with a Peltier cooled EDS detector, with 30 mm^2 detector area, 133 eV resolution and working at a temperature of 40K (Xflash 430 detector from Bruker). The acceleration energy was 3KV on the SEM column to make sure that the signal comes as close to the surface as possible.

There are different signals that need to be analyzed: Lα transition of Mo at 2.293 KeV, Kα transition of S at 2.307 KeV, Kα transition of F at 0.677 KeV and Kα transition of Si at 1.739 KeV.

The problem that it is necessary to face is that the M transition of gold, present in the electrodes defined on the flakes is too close to the Lα molybdenum or sulfur transition. If an EDX spectrum is taken in a MoS_2 FET like the one is shown in Figure 4.2, the signals will be mixed, showing the indicator from gold in the Mo or S maps as Figure 4.3 represents. Figure 4.3b corresponds with the Au transition mapping of a MoS_2 FET. It is possible to observe how this signal is mixed in Figures 4.3c and 4.3d, where the electrodes are identified as Mo and S respectively.

For that reason, Figure 4.4 shows the EDX characterization of an exfoliated MoS_2 flake over a Si-SiO_2 substrate without gold electrodes. Due to the lateral resolution of the equipment, a simple structure was fabricated, as shown in the SEM image of Figure 4.4c.

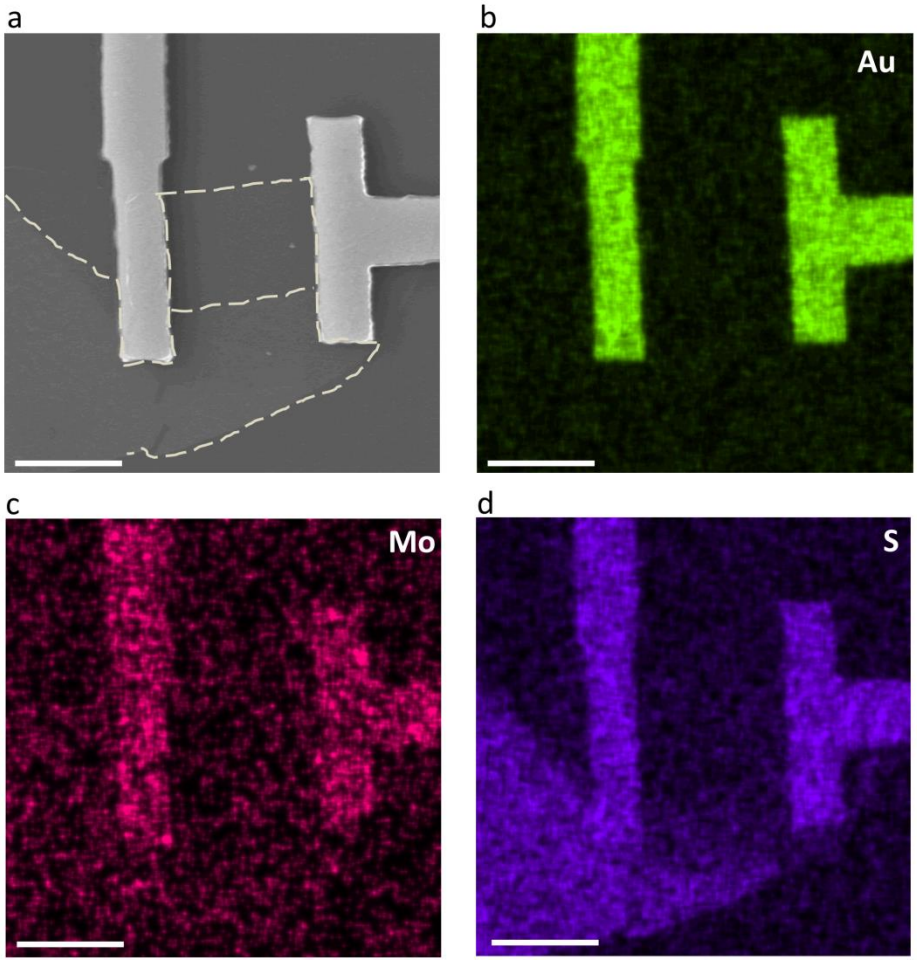

Figure 4.3: a SEM image of a MoS2 FET. The dashed line represents where the MoS_2 flake is. **b** Au M transition mapping of the FET. It is possible to observe only the electrodes. **c** Lα transition of Mo. The flake is not observed. The gold electrodes appear as Mo, as a consequence of the Au M transition shadowing the real signal. **d** Kα transition of S. The thickest part of the MoS_2 flake is detected. Again, the electrodes appear as S, due to the Au signal mixing. Scale bars are 6 µm.

Figure 4.4a shows the EDX spectra before (red) and after (blue) the patterning. Normalization was made taking into account the silicon peak, which supposedly does not vary between steps. The Si, Mo, and S are within error exactly the same after the patterning with no

signatures of additional fluorinated compounds or by-product materials. The inset of Figure 4.4a shows a small variation in the S and Mo intensities between before and after steps. This variation could be attributed to changes in the total amount of MoS_2 material due to the etching process rather than in its chemical composition. There is also a variation in the carbon peak as a consequence of carbon deposition when performing SEM characterization.

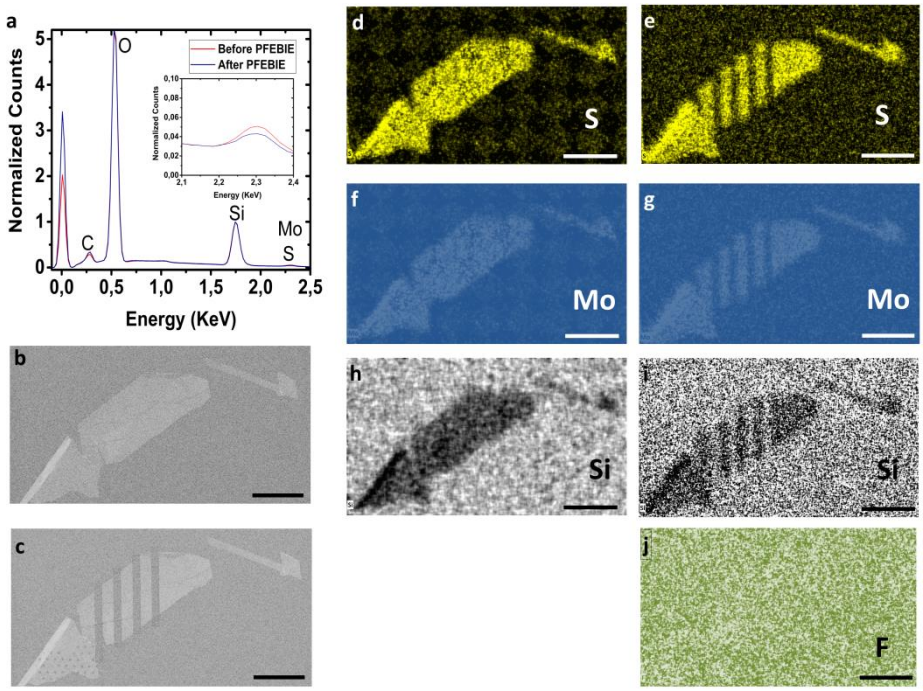

Figure 4.4: a EDX spectra before (red) and after the patterning (blue) showing the characteristic transitions of carbon, oxygen, silicon, molybdenum, and sulfur. **b** SEM image of the initial flake. **c** SEM image after PFEBIE. **d** Kα transition of S before the patterning. **e** Kα transition of S after the patterning. **f** Lα transition of Mo before the patterning. **g** Lα transition of Mo after the patterning. **h** Kα transition of Si before the patterning. **i** Kα transition of Si after the patterning. **j** Fluorine Kα transition after the patterning, showing that there is no presence of reaction by-products. Scale bars are 4 µm.

Figures 4.4d to 4.4j represent the transition mappings of S (Figures 4.4d and 4.4e), Mo (Figures 4.4f and 4.4g), Si (Figures 4.4h and 4.4 i) and F (Figure 4.4j). These transitions happen at the same energy and they are the same between before and after steps. It is important to remark how Figure 4.4j shows that after the patterning there was not fluorine indication, demonstrating that fluorinated compound or reaction by-products do not redeposit during the etching process. EDX characterization reveals that the height increase shown in Figure 4.2d could be attributed to redeposited Mo or S species. In case the material would be redeposited, it would have a similar grain structure than the previous one and it is not possible to observe any change by EDX.

Additional backscattered electrons (BSE) images before and after the patterning were taken in a device similar to the one shown in Figure 4.2. BSE detector also gives information about the composition of the material. Figure 4.5 shows BSE SEM images of a device before and after the patterning. It is possible to observe that the contrast remains equal between before and after steps, indicating that the composition of the devices did not change.

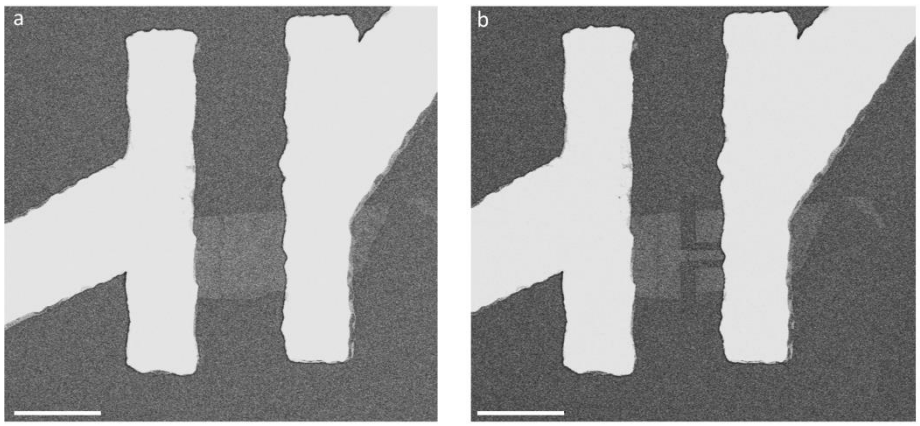

Figure 4.5: a BSE SEM image of a device before PFEBIE. **b** BSE SEM image after the patterning. The contrasts remain equal between steps, indicating that there is no change in composition, within the experimental error. Scale bars are 3 µm.

4.3 Electrical Properties

In this section, the consequences that PFEBIE has over the electrical properties will be discussed.

Figure 4.6 shows optical images of the device under study in this section before and after PFEBIE.

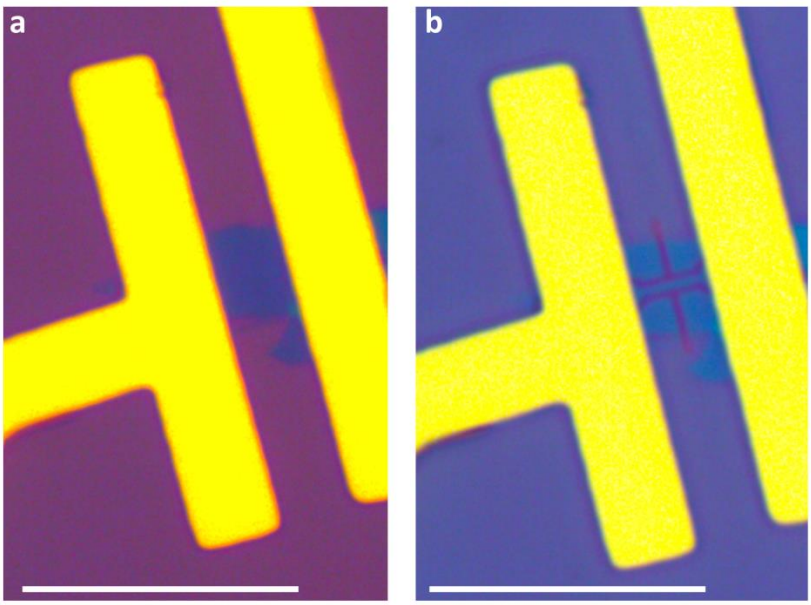

Figure 4.6: a Optical image of a MoS2 device. **b** HDR optical image of the same device after PFEBIE, showing a 250 nm narrowing. Scale bars are 15 µm.

Figure 4.7 shows room temperature characteristics of the device shown in Figure 4.6 before and after the patterning. The blue curve corresponds to the initial device, where n-type doping is observed, with the threshold voltage at -90 V. This initial characterization agrees with the behavior of natural MoS_2, due to the presence of Re impurities which are present in MoS_2 minerals, providing good n-type doping [2]. After PFEBIE the threshold voltage value of 2 V indicates that the device's doping has been reduced, becoming more intrinsic. This change in doping is attributed to the non-exposed regions, where

the current is flowing through. This would be only possible if a XeF_2 fraction spontaneously dissociates when free radicals interact with the surface, causing sulfur etching.

Different studies have reported a semiconductor to metallic phase change in MoS_2 devices under plasma treatment [3]. Due to the metallic character of the 1T MoS_2 phase [4, 5], it would not show any gate response in the electrical characterization shown in Figure 4.7a. In this case, under gate sweeping, the device is still clearly showing a field effect response, displaying the characteristic behavior of the semiconducting 2H phase.

In the initial device, the saturation, ON-OFF states can be clearly identified. Nonetheless, after PFEBIE the saturation state is not clearly observed because it is beyond the gate voltage measuring range. This makes comparison hard between before and after devices. It is important to mention that there is a decrease in the current after the patterning. The initial device is in the μA range, while the patterned device is in the nA regime. This is a consequence of a decrease in the channel width in an order of magnitude after the patterning, which should reduce the current to approximately 10 % its initial value. The initial device's mobility is around 2 $cm^2 \cdot V^{-1} \cdot s^{-1}$, within the typical values for these devices [6, 7]. After PFEBIE, it was reduced to 0.39 $cm^2 \cdot V^{-1} \cdot s^{-1}$. The reduction in mobility is caused by changes in the geometry of the channel and maybe, due to the creation of defects when the etching was done. The ON/OFF ratio of the device before the patterning was 10^5. After PFEBIE, it was not possible to calculate it because the saturation region is not observed.

Electrical measurements were performed in 10 different samples, before and after the patterning. Figure 4.7b shows the threshold voltage value in all samples before and after PFEBE. It is possible to observe that 90 % of the devices suffer a change from n-doped towards intrinsic or even lightly p-doped manifesting a tendency in the electrical behavior. The mechanism is not totally clear, but a possible hypothesis to that tendency is that sulfur vacancies are created when

XeF_2 etches the desired zones due to high chemical selectivity of the gas [8-10]. Some groups have studied the interaction of TMDCs with ion beams, observing the creation of vacancies [11, 12], which supports the hypothesis. It is known that sulfur vacancies are a strong p-dopant due to their acceptor character [2] and charge transfer mechanisms in sulfur deficient MoS_2 [13, 14], making this process a plausible scenario.

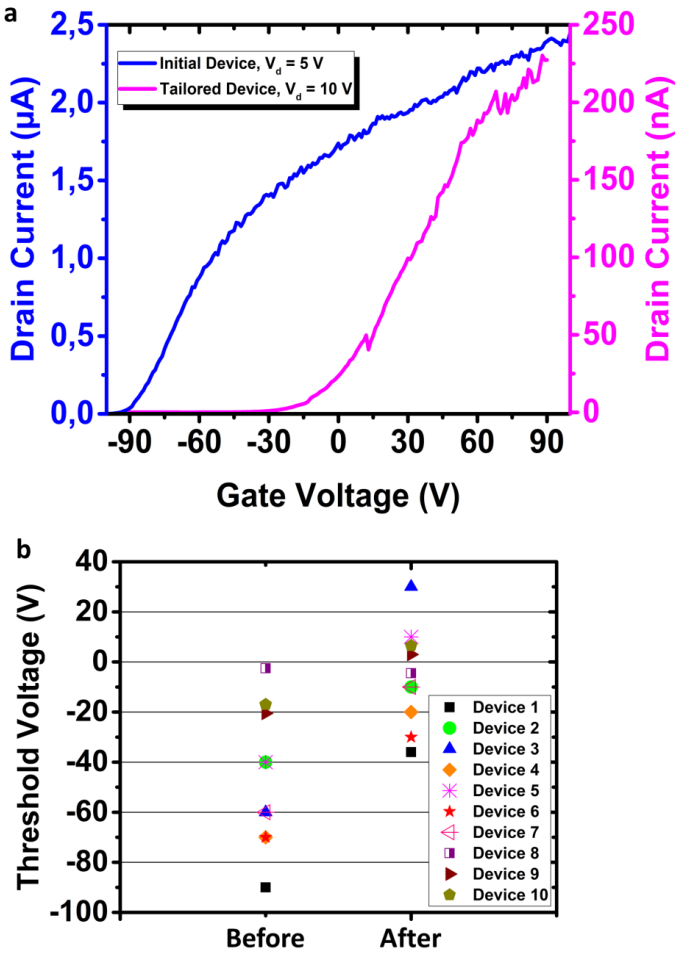

Figure 4.7: a RT transfer characteristics of the MoS_2 FET shown in Figure 4.4 before (blue) and after (pink) PFEBIE. The threshold voltage shifts indicate a variation from n-type doping to intrinsic doping after PFEBIE. V_{th} varies from -90 V to 2 V. **b** V_{th} variation of ten different devices before and after the channel width modification.

Figure 4.7b also shows that before PFEBIE it is present a larger dispersion in the threshold voltage. The mean value of V_{th} before the patterning is V_{th} = -47 ± 30 V. After the patterning it is V_{th} = -7 ± 20 V. This is mostly attributed to differences in shape, number of contacted layers or total area covered by the metallic contacts, all of them parameters impossible to control with accuracy with the exfoliation method. For that reason, it is complex to determine a standard conduction channel in the fabrication procedure. The power of PFEBIE resides on controlling the channel width and its geometry. After the patterning, the channel can be standardized. In this thesis, all the channels in the after devices are 250 nm wide, as Figure 4.8 shows. This clearly reduces the dispersion after the patterning procedure. However, there is diversity in the geometrical factors after the patterning. These factors affect the semiconducting gap and thus the FET characteristics after the patterning still had dispersion.

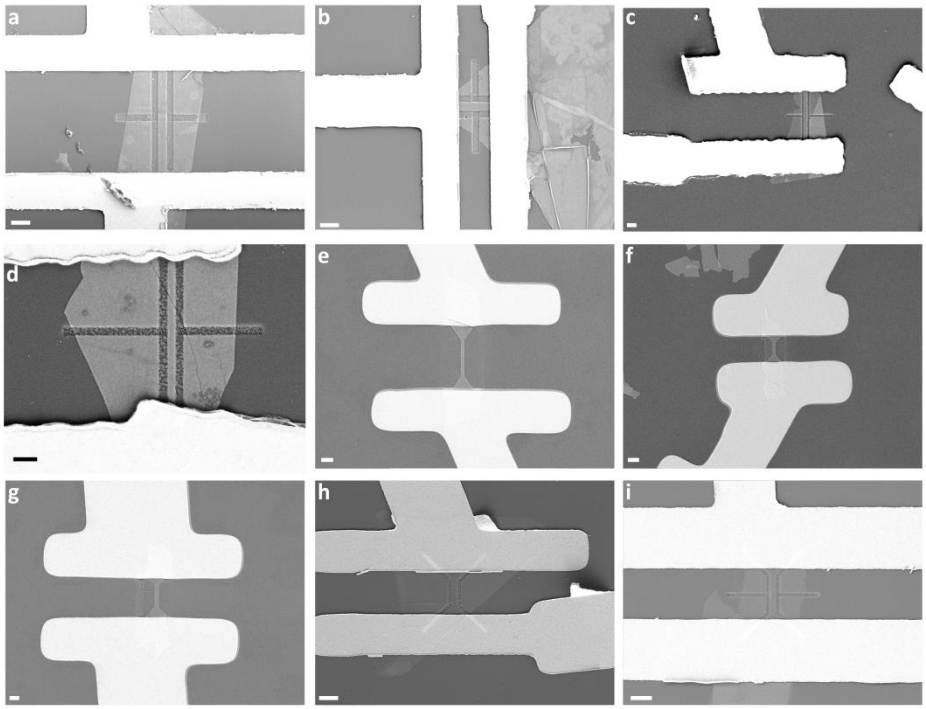

Figure 4.8: SEM images of the devices shown in Figure 4.5b. Scale bars are 500 nm.

With that, PFEBIE has been demonstrated to be an effective technique for modifying the width of MoS_2 based FETs. As a consequence, the doping of the devices has changed, suffering a shift from n-type towards intrinsic or even p-type doping. This change in doping is possibly mediated by a sulfur vacancy mechanism. In subsequent sections, the effect of PFEBIE over the optical properties and the relationship of sulfur content or doping with these properties will be studied.

4.4 Optical Properties

Optical properties, such as PL and Raman, are strongly dependent on the doping level [15-17]. Accordingly, this section will cover the optical characterization of the devices before and after PFEBIE.

4.4.1 Raman characterization

As chapter 2 described, MoS_2 has two characteristic Raman modes, which are thickness dependent. The E^1_{2g} mode corresponds with an in-plane shear mode of Mo and S atoms and it is located approximately at 380 cm^{-1}. The A_{1g} mode corresponds with an out of plane vibration of sulfur atoms and it is located around 410 cm^{-1} [18].

Figure 4.9 shows Raman intensity maps before and after the patterning in the device shown in Figure 4.6. Figures 4.9a and 4.9b show the A_{1g} and E^1_{2g} Raman intensity mappings before PFEBIE respectively. Figures 4.9c and 4.9d shows the same mappings after the patterning, where the 250 nm narrowing is observed. Both peaks are present after the patterning, indicating that the chemical composition of the device has not been substantially altered. The inset of Figures 4.9a and 4.9c shows an optical image of the MoS_2 FET to better discern the mappings. As mentioned before, the channel was patterned in a cross-bar shape to avoid electrical conductivity out of the 250 nm wire.

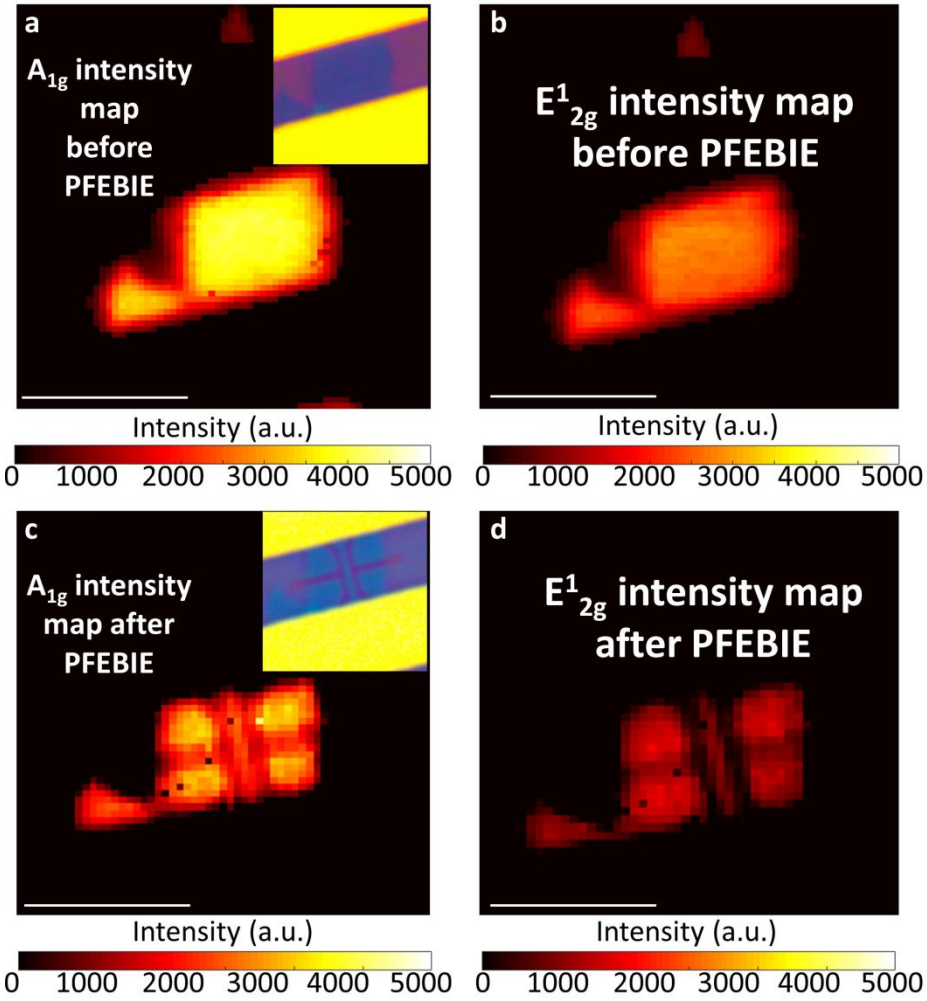

Figure 4.9: a A_{1g} intensity map before PFEBIE. Inset shows an optical image of the device. **b** E^1_{2g} intensity map before PFEBIE. **c** A_{1g} intensity map after PFEBIE. Inset shows an optical image of the device after the patterning. **d** E^1_{2g} intensity map after PFEBIE. The 250 nm narrowing is observed. Both peaks are still present, indicating that the composition did not change substantially. Scale bars are 2 µm.

Figure 4.10 represents the peak position difference (PPD) mapping between the E^1_{2g} and the A_{1g} peaks. Figure 4.10a corresponds with the mapping before the patterning and Figure 4.10b shows the same mapping after PFEBIE. The dashed marks shown in Figure 4.10b indicates where the patterning was done. Due to fitting parameters, it

is difficult to observe the 250 nm narrowing as shown in Figure 4.9. An increase of 2.5 cm^{-1} in average is identified (see spectra of Figure 4.10). This increase is observed in the unexposed regions. This is only possible if XeF_2 spontaneously dissociates in those zones, changing the Raman signal. Previous studies have shown that first-order Raman modes vary as a function of the sulfur content [17], an intrinsic property of defective systems. The increase in PPD supports the hypothesis of sulfur vacancy creation when the etching is done, coexisting with the electrical measurements.

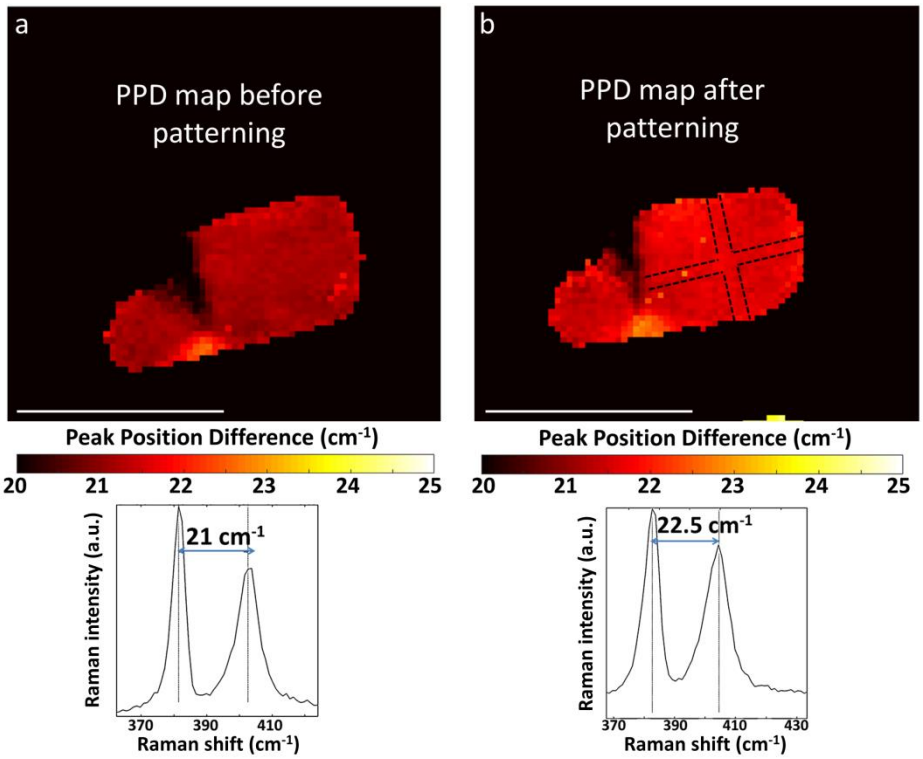

Figure 4.10: a PPD mapping before the patterning. The spectrum below has been taken in a point of the flake. It shows the average value of the PPD **b** PPD mapping after the patterning. Dashed marks represent where the 250 nm patterning was done. An increase of 2.5 cm^{-1} is identified (average taken from different points). The spectrum corresponds to the same point that in a. Scale bars are 2 µm.

Figures 4.11a and 4.11b represent the evolution of the E^1_{2g} full width at half maximum (FWHM) mapping before and after PFEBIE respectively. An increase from 4 cm^{-1} to 6 cm^{-1} is detected. The same behavior is observed for the A_{1g} peak, which is represented in Figure 4.12. In this case, an increase from 7.5 to 9 cm^{-1} is observed. This increase in FWHM indicates defect creation [13, 19], which can also explain the reduction in mobility shown in section 4.3.

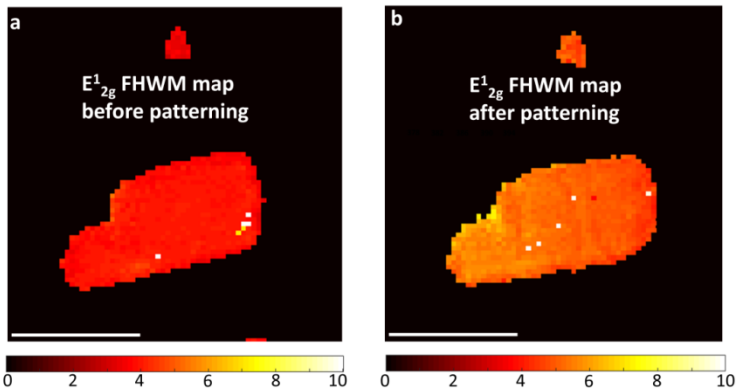

Figure 4.11: a E^1_{2g} FWHM map before the patterning. **b** E^1_{2g} FWHM map after the patterning. The 250 nm narrowing can be intuited in the central region of the flake. Due to fitting parameters, it is not as clear as in Figure 4.7. An increase from 4 to 6 cm^{-1} is observed. Scale bars are 2 µm.

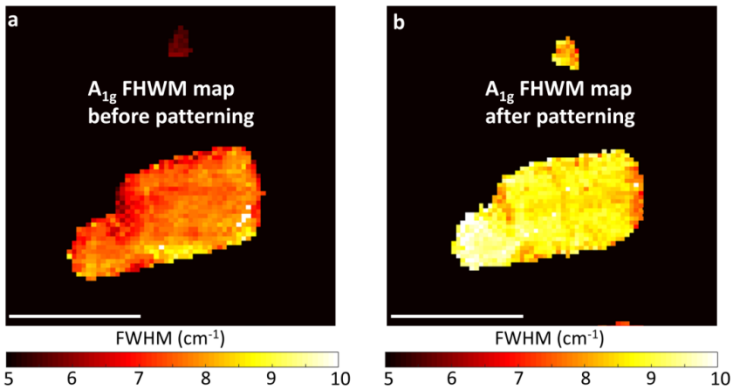

Figure 4.12: a A_{1g} FWHM map before the patterning. **b** A_{1g} FWHM map after the patterning. An increase from 7 to 9.5 cm^{-1} is observed in the entire flake. Scale bars are 2 µm.

4.4.2 PL characterization

As described in chapter 1, PL results on two characteristic features that appear as a consequence of the band splitting due to spin-orbit coupling, the A and B excitonic transitions. Figure 4.13 shows PL maps before and after the etching process. In those maps, the electrodes are observed as darker horizontal bars. The metallic character of the electrodes produces a higher Rayleigh scattering of the laser in those zones, increasing the background signal in those regions. It creates a ghost image of the Au electrodes, coming from a background difference.

Figures 4.13a and 4.13b correspond with the intensity maps of the MoS_2 A and B excitonic transitions respectively before PFEBIE. Figure 4.13c corresponds with a PL spectrum, showing that the B transition occurs at 625 nm and the A transition, at 675 nm. Figures 4.13d and 4.13e display the same features after PFEBIE, where the 250 nm channel is observed. In this case, Figure 4.13f reveals that the excitonic transitions occur at 615 nm and 662 nm for the B and A excitons respectively, this is approximately a 10 nm blue-shift.

The relative intensity of those transitions also changes after PFEBIE. The initial device shows an I_B/I_A ratio of 0.71, where I_B and I_A are the intensity of each transition. After PFEBIE, this ratio is 0.8. This change in the intensity ratio could be attributed to the observed changes in doping, in good agreement with previous studies [14, 20], where doping over MoS_2 devices result in a more intense PL spectrum because of the p-doping effect.

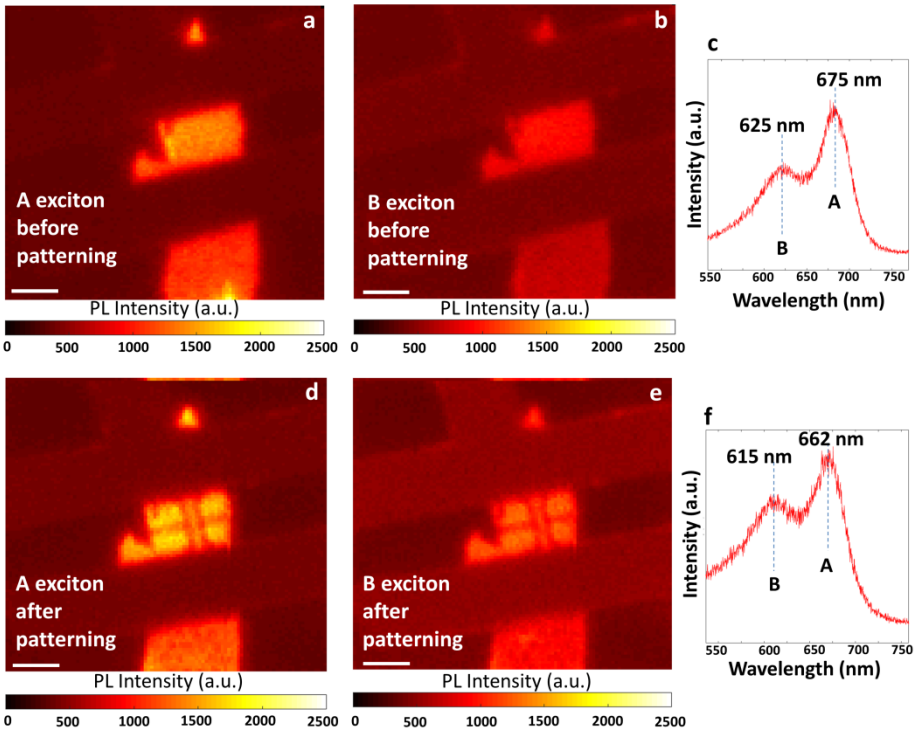

Figure 4.13: PL maps before and after PFEBIE. **a** A exciton PL mapping before PFEBIE. **b** B exciton PL mapping before PFEBIE. **c** PL spectrum acquired before the patterning. **d** A exciton PL mapping after the patterning. **e** B exciton PL mapping after PFEBIE. The 250 nm width narrowing can be clearly observed. **f** PL spectrum after PFEBIE, where a 10 nm blue-shift is detected. Scale bars are 2 µm

4.5 Conclusions

In this chapter, the consequences that PFEBIE has over the optoelectronic properties of MoS_2 devices have been studied. PFEBIE has been demonstrated to be a tool that allows tailoring devices geometries after lithographical fabrication without the need of a stencil mask, saving fabrication steps and contaminants.

The AFM characterization shows a change in height after the patterning. EDX and BSE SEM characterization reveals that after the

patterning the composition of the device is exactly the same. For that reason, the change in height indicates that there might be some redeposited MoS_2 over the surface of the device.

Electrical characterization displays a transition from n-type doping towards intrinsic or even p-type doping after PFEBIE. A study of 10 devices has been carried out, showing that there is a clear tendency in the mechanism. The mechanism underneath is sulfur vacancy creation after the etching process. This hypothesis is supported by Raman and PL spectroscopy. PL suffers a blue-shift of 10 nm after PFEBIE and it also suffer a change in the relative I_B/I_A ratio due to the doping mechanism when sulfur vacancies are created. Raman mappings show a change in FWHM and PPD to higher values after the patterning, a characteristic feature of sulfur vacancy and defects creation.

Thereby, PFEBIE could show the viability of tailor the electric behavior once a device has been electrically characterized. Next chapter will show the possibility of exploiting the doping mechanism to fabricate lateral homo-junctions based on MoS_2, a task tremendously important for next-generation electronics.

Bibliography

[1] C. Lee, H. Yan, L. E. Brus, T. F. Heinz, J. Hone, and S. Ryu, "Anomalous Lattice Vibrations of Single- and Few-Layer MoS2" *ACS Nano,* vol. 4, no. 5, pp. 2695-2700, 2010.

[2] H.-P. Komsa and A. V. Krasheninnikov, "Native defects in bulk and monolayer MoS2 from first principles" *Physical Review B,* vol. 91, no. 12, p. 125304, 2015.

[3] C. H. Sharma, A. P. Surendran, A. Varghese, and M. Thalakulam, "Stable and scalable 1T MoS2 with low temperature-coefficient of resistance" Scientific Reports, vol. 8, no. 1, p. 12463, 2018.

[4] X. Guo, G. Yang, J. Zhang, and X. Xu, "Structural, mechanical and electronic properties of in-plane 1T/2H phase interface of MoS2 heterostructures" *AIP Advances,* vol. 5, no. 9, p. 097174, 2019/03/15 2015.

[5] M. Acerce, D. Voiry, and M. Chhowalla, "Metallic 1T phase MoS2 nanosheets as supercapacitor electrode materials" Nature Nanotechnology, vol. 10, p. 313, 2015.

[6] K. S. Novoselov *et al.*, "Two-dimensional atomic crystals" *Proceedings of the National Academy of Sciences of the United States of America,* vol. 102, no. 30, p. 10451, 2005.

[7] H. Wang *et al.*, "Integrated Circuits Based on Bilayer MoS2 Transistors" *Nano Letters,* vol. 12, no. 9, pp. 4674-4680, 2012.

[8] C.-S. Kim, S.-H. Ahn, and D.-Y. Jang, "Review: Developments in micro/nanoscale fabrication by focused ion beams" *Vacuum,* vol. 86, no. 8, pp. 1014-1035, 2012.

[9] D. Xia, J. Notte, L. Stern, and B. Goetze, "Enhancement of XeF2-assisted gallium ion beam etching of silicon layer and endpoint detection from backside in circuit editing" *Journal of Vacuum Science & Technology B,* vol. 33, no. 6, p. 06F501, 2018/05/08 2015.

[10] M. S. Alias *et al.*, "Enhanced Etching, Surface Damage Recovery, and Submicron Patterning of Hybrid Perovskites

using a Chemically Gas-Assisted Focused-Ion Beam for Subwavelength Grating Photonic Applications" *The Journal of Physical Chemistry Letters,* vol. 7, no. 1, pp. 137-142, 2016.

[11] M. G. Stanford *et al.*, "High Conduction Hopping Behavior Induced in Transition Metal Dichalcogenides by Percolating Defect Networks: Toward Atomically Thin Circuits" *Advanced Functional Materials,* vol. 27, no. 36, p. 1702829, 2018/09/20 2017.

[12] M. G. Stanford *et al.*, "Tungsten Diselenide Patterning and Nanoribbon Formation by Gas-Assisted Focused-Helium-Ion-Beam-Induced Etching" *Small Methods,* vol. 1, no. 4, p. 1600060, 2018/09/20 2017.

[13] A. Nipane, D. Karmakar, N. Kaushik, S. Karande, and S. Lodha, "Few-Layer MoS2 p-Type Devices Enabled by Selective Doping Using Low Energy Phosphorus Implantation" *ACS Nano,* vol. 10, no. 2, pp. 2128-2137, 2016.

[14] D. M. Sim *et al.*, "Controlled Doping of Vacancy-Containing Few-Layer MoS2 via Highly Stable Thiol-Based Molecular Chemisorption" *ACS Nano,* vol. 9, no. 12, pp. 12115-12123, 2015.

[15] B. Chakraborty, A. Bera, D. V. S. Muthu, S. Bhowmick, U. V. Waghmare, and A. K. Sood, "Symmetry-dependent phonon renormalization in monolayer MoS2 transistor" *Physical Review B,* vol. 85, no. 16, p. 161403, 2012.

[16] M. R. Laskar *et al.*, "p-type doping of MoS2 thin films using Nb" *Applied Physics Letters,* vol. 104, no. 9, p. 092104, 2018/05/08 2014.

[17] W. M. Parkin *et al.*, "Raman Shifts in Electron-Irradiated Monolayer MoS2" *ACS Nano,* vol. 10, no. 4, pp. 4134-4142, 2016.

[18] H. Li *et al.*, "From Bulk to Monolayer MoS2: Evolution of Raman Scattering" *Advanced Functional Materials,* vol. 22, no. 7, pp. 1385-1390, 2018/09/09 2012.

[19] N. Kang, H. P. Paudel, M. N. Leuenberger, L. Tetard, and S. I. Khondaker, "Photoluminescence Quenching in Single-Layer MoS2 via Oxygen Plasma Treatment" *The Journal of Physical Chemistry C,* vol. 118, no. 36, pp. 21258-21263, 2014.

[20] S. Mouri, Y. Miyauchi, and K. Matsuda, "Tunable Photoluminescence of Monolayer MoS2 via Chemical Doping" *Nano Letters,* vol. 13, no. 12, pp. 5944-5948, 2013.

Chapter 5: Fabrication of MoS_2 p-n Homo-junctions via PFEBIE

5.1 Introduction

The p-n junction has become a fundamental electrical component since its discovery 80 years ago [1]. It is the basic building block for modern semiconductor devices, including bipolar transistors, diodes, photodiodes, light emitting diodes or solar cells. This kind of devices can be created by joining two semiconductors of a different type: an n-type semiconductor containing an excess of electrons and a p-type semiconductor with an excess of holes. As a result, an intrinsic electric field at the junction interface is created and it can be used to rectify currents.

In bulk, the conventional p-n junction is created by chemically doping two different regions of the crystal forming a 3D junction. If the dimension of the semiconductor is scaled down, by passing from 3D to 2D materials, new possibilities appear (i.e. due to the thickness dependence of the TDMCs bandgap). Figure 5.1 shows an example of the different junctions architectures based on 2D semiconductors. Junctions based on 2D materials can follow two architectures: a vertical junction, in which the materials are stacked together and lateral junctions, in which the materials are joined at the same plane. Farther, it is important to mention that depending on the material composition the junctions can be classified as hetero-junctions, in which the forming materials are different and homo-junctions when the forming material is the same.

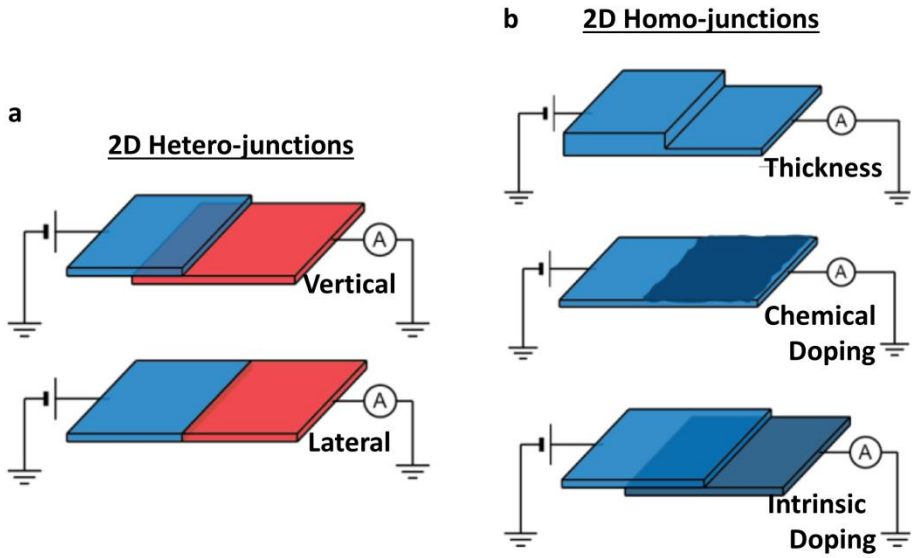

Figure 5.1: a Examples of 2D based hetero-junctions. Different colors represent diverse materials. **b** Different examples of 2D based homo-junctions. In this case, the material is always the same. There could be thickness dependent junctions, chemically altered junctions or even junctions formed by overlapping the material with changes in its intrinsic doping. Images adapted from [2].

In general, the fabrication of these devices is complex. For that reason, Figure 5.2 shows different examples of the convoluted fabrication of p-n junctions, where a lot of intermediate steps are necessary. There are a lot of things to keep in mind when fabricating 2D material based junctions. First of all, it is important to remind that due to the exfoliation process the flakes are irregular and not always is easy to align them. Secondly, despite achieving the transfer process, there are a lot of involved fabrication steps (resist deposition, lithography, wet or dry etching, chemical doping, etc.) that can damage the devices.

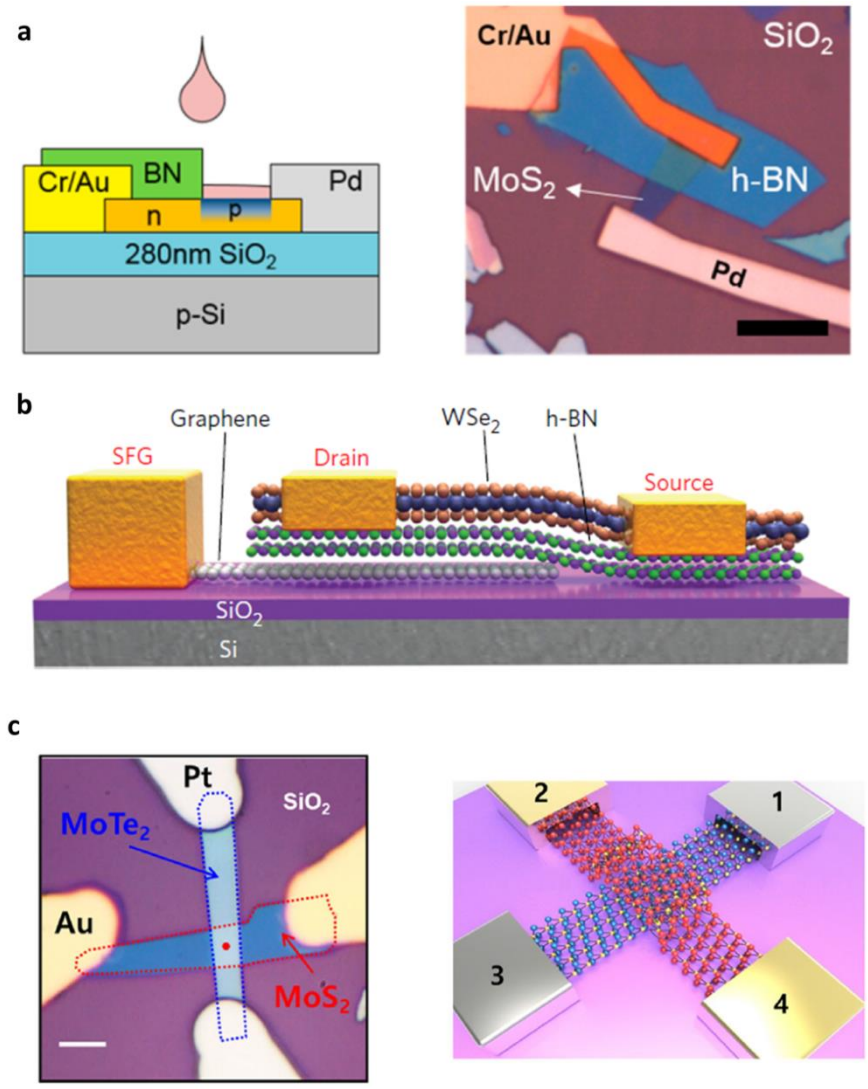

Figure 5.2: a Formation of a MoS2 junction via chemical doping. Successive lithography processes are necessary in order to fabricate the electrodes and aligning the flakes. In addition, chemical doping (represented by the pink drop) is necessary to form the p-n junction. Adapted from [3]. **b** Scheme of another type of hetero-junction. In this case, a graphene semi-floating gate is necessary. In addition, an aligning procedure is necessary to fabricate the Graphene-WSe_2-hBN junction Adapted from [4]. **c** An easier way of fabricating a 2D TDMC based junction. Nonetheless, several fabrication steps are necessary. Adapted from [5].

Due to all these problems, this chapter will show how PFEBIE could be used to easily fabricate MoS_2 lateral homo-junctions. Chapter 4 shows the effect of PFEBIE nano-patterning on the optical and electrical properties of MoS_2 FETs. A change from n-type doping towards intrinsic or even p-type was observed. The change was observed also in the non-exposed regions, a mechanism only possible if a XeF_2 fraction spontaneously dissociates over the remaining MoS_2 channel. Accordingly, this change in the unexposed regions will be exploited to modify the doping of a part of the MoS_2 channel, while the other region will not be modified, and thus creating the p-n homo-junction.

5.2 p-n Channel Fabrication

Previous studies show how it would be possible to selectively change the doping of a MoS_2 channel with different techniques [3, 6]. Again, I would like to remark how difficult and time-consuming is fabricating these structures. Reference [3] corresponds with the illustration shown in Figure 5.2a. The initial device is fabricated by electron beam lithography and evaporation of first, the Cr/Au electrode and second, the Pd electrode. Afterward, exfoliation of h-BN over the MoS_2 flake is necessary to protect a region of the MoS_2 channel. Finally, the unprotected MoS_2 region is doped via $AuCl_3$. In the case of Nipane et al. [6], the fabrication of the device is easier. Even so, they need to cover the MoS_2 device with resist and make an extra lithography process, previous to the doping treatment.

PFEBIE allows fabricating a lateral homo-structure from an n-type transistor in only one step. As described in chapter 4, there is a change in the remaining channel due to the spontaneous dissociation of XeF_2 over the non-exposed regions. For that reason, by selectively etching a part of the MoS_2 channel, it would be possible to conveniently modify the doping of only a region of the entire device. Figure 5.3 shows the fabrication of a p-n homo-junction. Figure 5.3a corresponds with the original device, where supposedly an n-type behavior will be observed

(as subsequent sections will be described). Figure 5.3b represents the tailored device after PFEBIE. In this image, the upper part of the channel will remain n-type, while the doping of the lower part of the MoS_2 channel will move towards p-type. As described in chapter 4, this is possible if there is a change in the remaining lower channel due to the spontaneous dissociation of XeF_2.

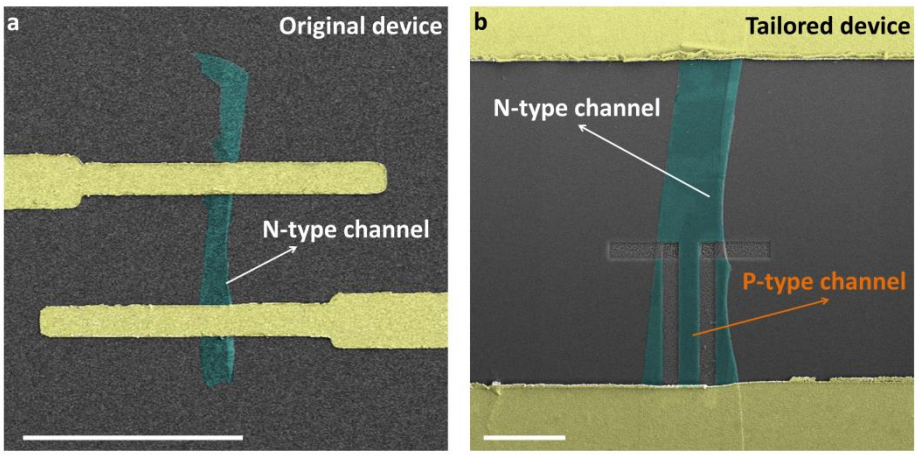

Figure 5.3: a Original device. IV transfer characteristics shown in the electrical characterization section reveal an n-type transistor behavior due to the nature of mineral MoS_2. Scale bar is 20 µm. **b** Tailored device. The upper channel will remain n-type while the doping of the lower channel will move towards p-type. Scale bar is 2 µm

In chapter 4 it was possible to observe that the change in doping after the patterning is not always from n-type to p-type. For this reason, the performance of the tailored device would change as a result of the doping level of the channel (that it is impossible to control due to the exfoliation process).

During this chapter, the geometry of the tailored devices is going to be the same. Figure 5.4 shows two more examples of the fabrication of this kind of structures, demonstrating again the reproducibility of PFEBIE.

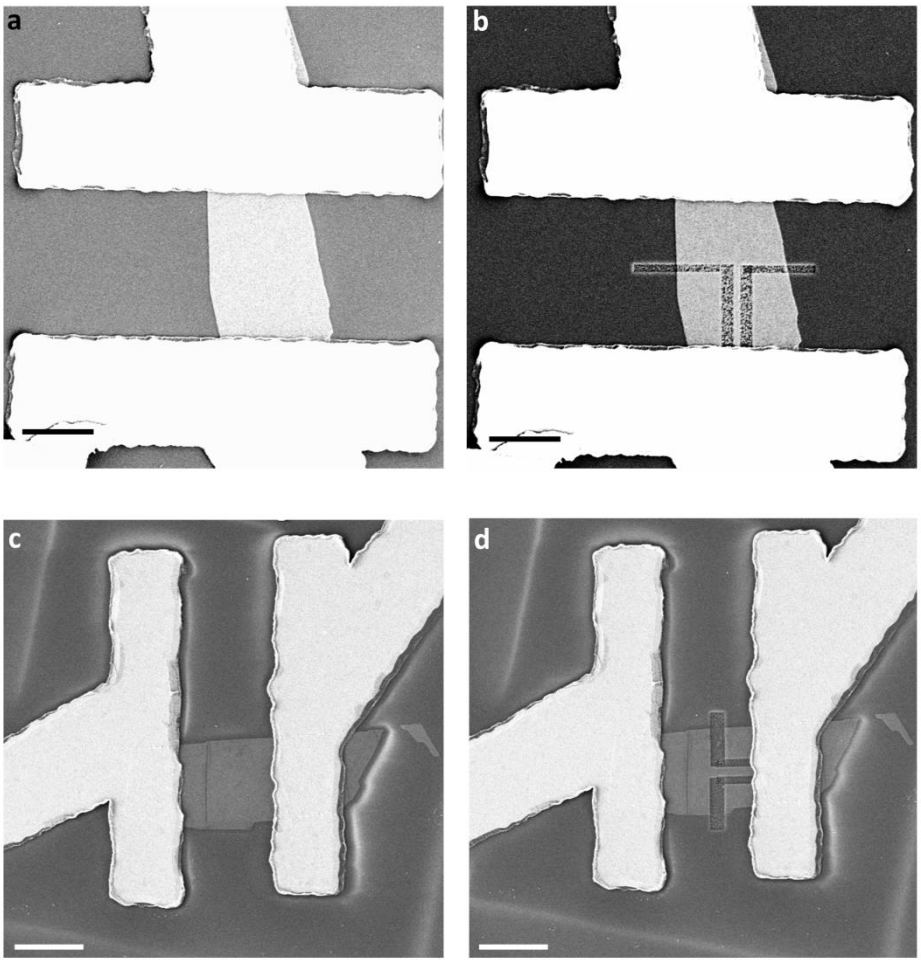

Figure 5.4: Examples of two devices before and after the patterning. **a** Initial device. **b** Same device than the shown in a, after the patterning. Again, the same structure than Figure 5.3b is observed. The upper part will present the same doping, while the lower channel will change its doping. **c** Another example of an initial MoS_2 device. **d** Tailored device. The same doping mechanism is expected. The white shadow around the device in c and d is a consequence of SEM observation. Scale bars are 2 µm.

5.2.1 Raman Spectroscopy

Although it is not the main scope of this chapter, Raman spectroscopy was performed in a tailored MoS_2 device like shown in Figures 5.3 and 5.4. Figure 5.5 represents the Raman mappings of the device shown in Figure 5.5a. Figure 5.5b represents the mapping that corresponds with the silicon peak at 520 cm^{-1}. The dashed line represents where the narrowing was done. As expected, the signal is more intense in the silicon regions and in those zones where the device was etched. In this device, the etched region is wider than the remaining channel. For that reason, is not possible to observe the tailored channel as shown in Figure 4.7. Figures 5.5c and 5.5d represent the E^1_{2g} and the A_{1g} peak mapping respectively of the device after the patterning. As reported in chapter 4, both peaks are still present, indicating that the device has not been chemically altered.

Optical properties such as Raman, PL or electroluminescence (EL) depend strongly on the electrical parameters [7, 8]. Future work could cover the study of these properties as a function of electrical characterization. The cryostat will be crucial for that porpoise. The optical window of the cryostat allows performing optoelectronic measurements. For this reason, it is necessary to implement the optical set up shown in Figure 2.11e. In the optical path, it is necessary to connect a fiber coupler to the spectrometer. This fiber coupler will allow collecting the Raman signal, generated from the interaction of the laser source and the sample. At the same time, electrical characterization will be possible to perform and a complete study will be achieved. This point would be crucial in further studies of the MoS_2 p-n homo-junctions, where the optical properties play a very important role [9-11].

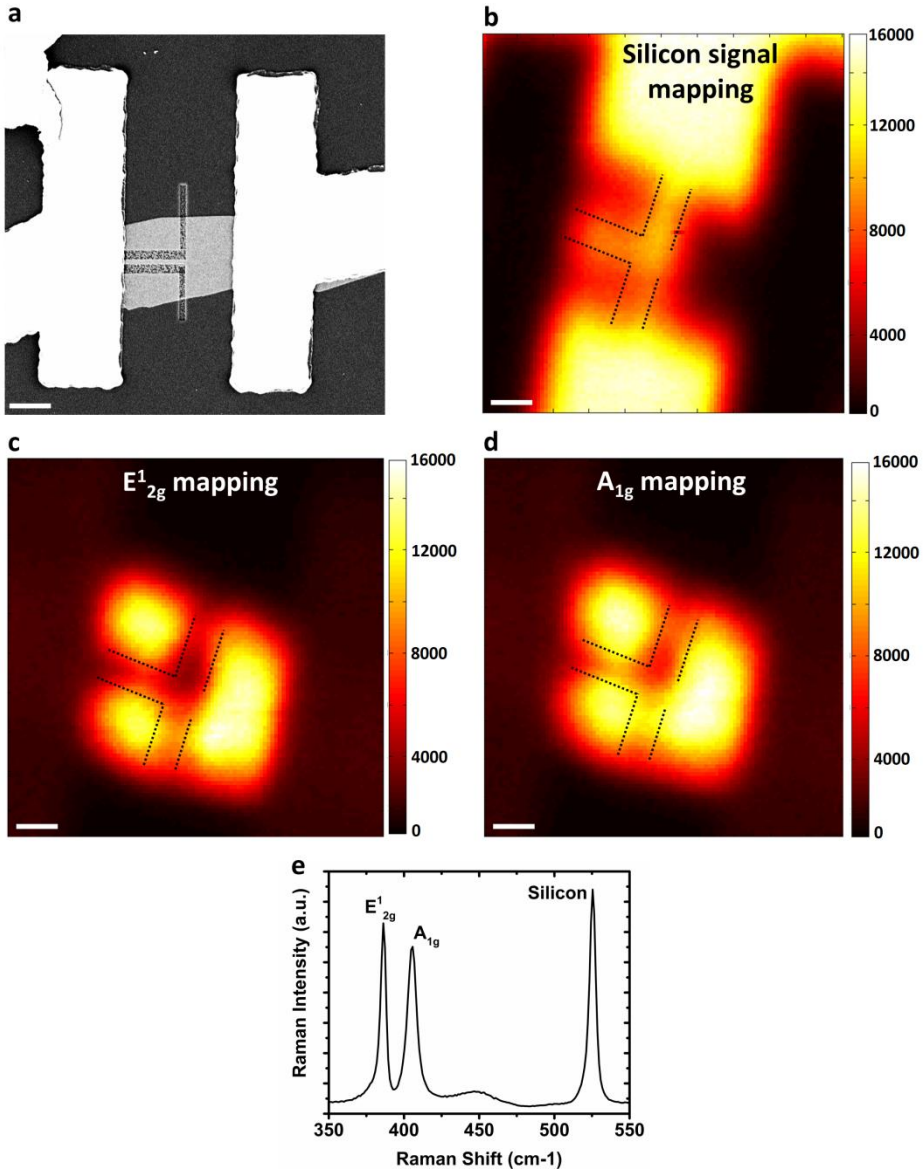

Figure 5.5: a SEM image of the MoS2 lateral homo-junction. **b** Raman mapping at 520 cm-1 (silicon signal). The scissoring is observed. **c** E^1_{2g} Raman mapping after the patterning. **d** A_{1g} Raman mapping after the patterning. Both, E^1_{2g} and A_{1g} peaks indicate that the device has not been chemically altered. **e** Raman spectrum of the MoS_2 lateral homo-junction.E^1_{2g} peak is localized at 385 cm^{-1}. The A_{1g} peak is localized at 407 cm^{-1}. Silicon peak can be observed at 425 cm^{-1}. Scale bars are 2 µm.

5.3 Electrical Properties

This section will cover the study of the electrical properties on the MoS_2 lateral homo-junctions.

5.3.1 RT Characterization

Figure 5.6 shows the electric characterization of the device shown in Figure 5.3, carried out at ambient conditions. As previously reported, the intention is creating a lateral homo-junction by tailoring half of the conduction channel. Due to the creation of sulfur vacancies (as discussed in chapter 4), a change in the doping will occur. For this reason, one region of the device will remain equal, since the tailored part will change its doping, creating a lateral homo-junction.

Figure 5.6a corresponds with the electric characterization of the device at different gate voltage biases, before the patterning. Figure 5.6b corresponds with the RT transfer characterization of the FET Mos_2 device before PFEBIE. V_{th} is -10 V [12], indicating an n-type doping. The calculated mobility is 3.7 $cm^2 \cdot V^{-1} \cdot s^{-1}$, within the standard values previously reported [13].

After the nano-patterning, the device shown in Figure 5.3b was electrically characterized again. In this case, measurements under illumination were performed in the setup shown in Figure 2.12.

Figure 5.6c shows the RT characteristic of the MoS_2 device after PFEBIE under darkness (blue line) and illumination (red line) conditions. A change in the IV characteristic is noticed. After PFEBIE, a diode-type behavior is recognized. Under darkness conditions, the direct state is observed at 60 V. Essentially, there is no current flowing in the reverse direction until -90 V, which is the breakdown voltage. An increase in the direct region is observed under white light illumination. The characteristic voltages are one order of magnitude higher than in previous reports [14]. This could be attributed to the etching process,

compared with pristine devices. The etching parameters were aggressive enough to ensure the formation of the new channel. 500 loops with a dwell time of 500 ns were used. In the next sections, the parameters will be reduced with the intention of creating the channel with a minor quantity of defects.

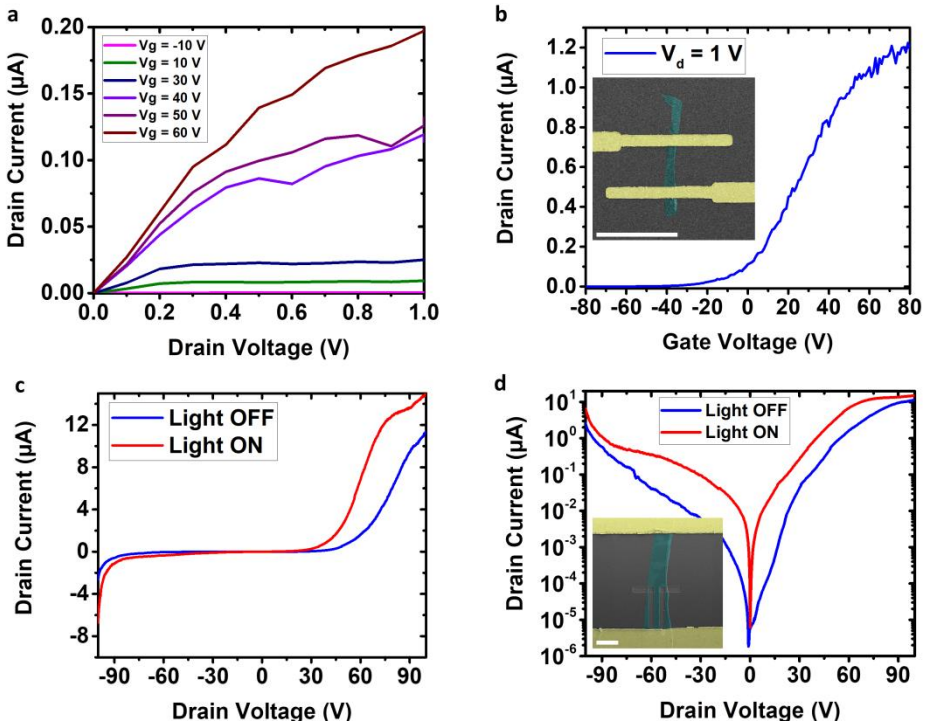

Figure 5.6: a Source-drain IV curves before PFEBIE. Electric characterization corresponds with the device shown in Figure 5.3a. **b** Id vs Vg curve before the patterning in the same device. **c** Id vs Vd characterization after PFEBIE under dark and illumination conditions. A diode-type behavior is observed, clearly identifying the direct and the avalanche states. These regions depend on the illumination state. **d** Same curve represented in logarithm scale.

There are two important parameters to characterize the performance of a diode: the current rectification ratio and the ideality factor [14, 15]. The first one is defined as the ratio of reverse and forward states at the same source-drain bias. This factor strongly depends on the value of the gate voltage [15], going from 1 to 10^3 depending on the

gate bias. The ideality factor can be obtained from the Shockley equation[16]. In an ideal diode, the ideality factor is one, with a slope of 60 mV per decade of current change. Figure 5.6d represent the logarithm plot of the diode at 0 gate voltage. From this curve, the rectification ratio is deduced to be 10 for a voltage bias of 60 V. The ideality factor is too high, more than in conventional diodes. This could explain the high voltage values at the forward and reverse states and the low slopes in the logarithmic plot of Figure 5.6d.

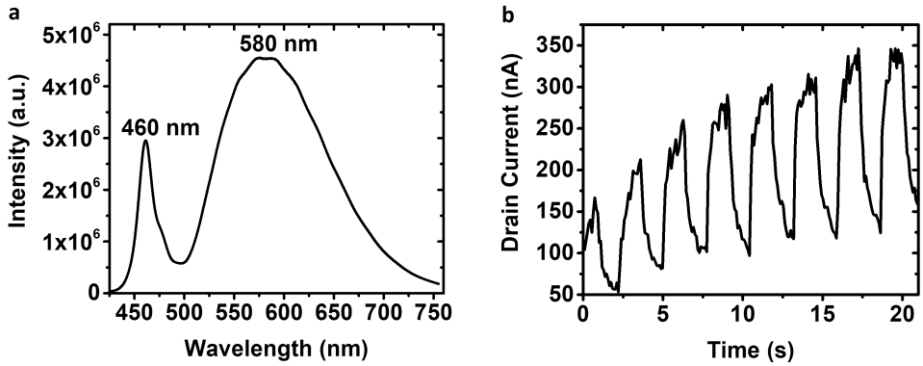

Figure 5.7: a Spectrum of the excitation source. **b** Photoresponse as a function of time.

Figure 5.7 shows the characterization of the MoS_2 homo-junction at RT conditions under white illumination. Figure 5.7a corresponds with the spectrum of the white LED, with two strong features at 460 and 580 nm. Figure 5.7b shows the photoresponse as a function of time, with an illumination period of 2.5 seconds. The drain current varies by illuminating the sample with a change in the current of 2-3 times the dark current. The rising time (τ_{rise}) is lower than 0.1 seconds, while the decay time is much higher, in the order of seconds. The photoresponse increases a little bit due to trapped charges in the oxide interface, a mechanism known as photo gaining.

It is important to compare the photoresponse of the device before and after the patterning. It is also crucial to perform electrical measurements at different wavelengths to study the photocurrent of the device. For that reason, we fabricate more samples and we

characterize them at cryogenic conditions, as the following sub-section will show.

5.3.2 Cryogenic Characterization

Optoelectronic characterization is performed in the set up shown in Figure 2.11. A SuperChrome laser source was used. It allows tuning the wavelength in the visible range of the spectrum, from 400 nm to 800 nm. Transfer characteristics of the device shown in Figures 5.4a and 5.4b were studied in the cryostat before and after PFEBIE under different illumination conditions.

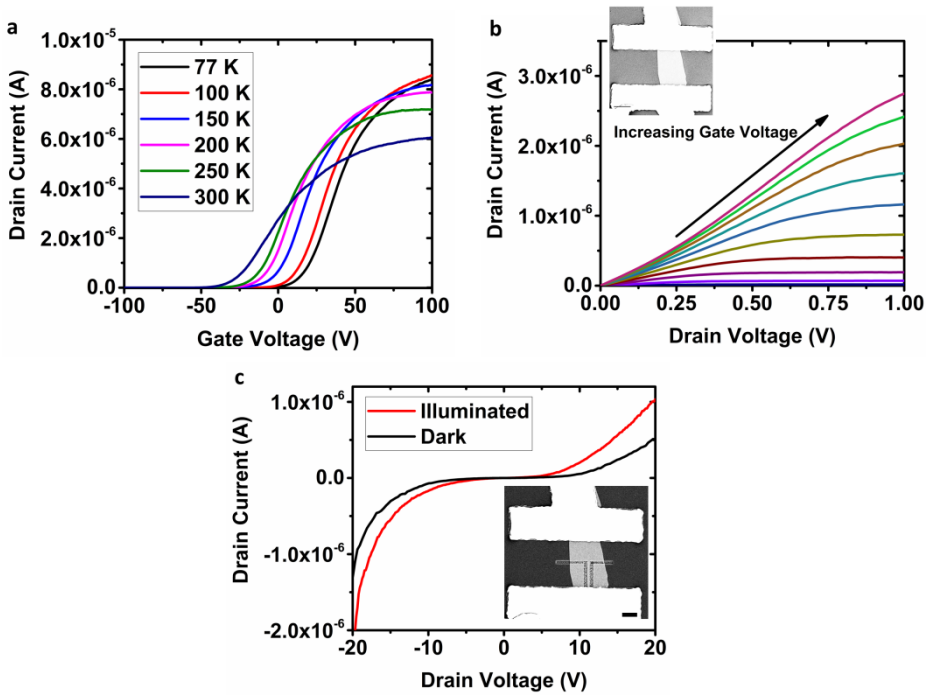

Figure 5.8: Transfer characteristics. **a** Drain current as a function of the gate voltage curve at different temperatures of the original device. **b** Drain current as a function of drain voltage curve at different gate bias. **c** Drain current as a function of drain voltage curve of the MoS_2 tailored homo-junction. It is possible to observe how the electric behavior has changed after the patterning. A diode-type behavior is observed, with a rectification ratio of 2 for a drain voltage of 10 V.

Figure 5.8 shows the electrical characterization of both, the initial FET and the tailored MoS_2 homo-junction. Figure 5.8a corresponds with the drain current as a function of the gate voltage transfer characteristics at different temperatures. The threshold voltage varies with temperature, a characteristic feature in this kind of devices[17]. Figure 5.8b displays the drain current vs drain voltage curve at different gate voltages, with the characteristic behavior of MoS_2 FETs. After this characterization, PFEBIE was used to alter the geometry of the conduction channel, as shown in the inset of Figure 5.8c. Figure 5.8c corresponds with the electric characterization after PFEBIE at 77K. It shows that the behavior has totally changed after the patterning. A diode type behavior is observed, with the forward and reverse states at lower voltages compared with previous devices. The performance of the device clearly depends if the device is illuminated or not. In this device, the forward state appears at 10 V in the dark state and at 5 V under illumination. The same behavior is observed in the reverse state, with the reverse voltage at -15 V under dark conditions and at -10 V under illumination (in the same order than in previous studies [6, 18]). Compared with the device shown in Figure 5.6 the forward and reverse voltages appear at lower values. As mentioned before, the number of loops was reduced to 250 loops. By decreasing the number of loops per point, the formation of defects or vacancies should be reduced, a feature that can influence these voltages.

Figure 5.9 coincides with the optoelectronic characterization of the original and tailored device. Figure 5.9a shows the photoresponse at different wavelengths in the original MoS_2 FET. The change is higher at lower wavelengths, thus is, higher energies. This is coherent taking into account the value of the MoS_2 bandgap and it agrees with previous studies [19]. For wavelengths higher than the bandgap the generated current under illumination is negligible.

Figure 5.9b corresponds with the photoresponse of the MoS2 homo-junction. As mentioned before, the generated current under illumination is higher if the wavelength is lower due to the value of the

MoS_2 bandgap. At 700 nm, the generated photocurrent is negligible. A diode has two figures of merit, one is the rectification and the other one is the generated current under light illumination. It is true that the rectification is very low, but the generated photocurrent is higher than the measured for the initial device. This makes sense since the performance of a diode under illumination should be better

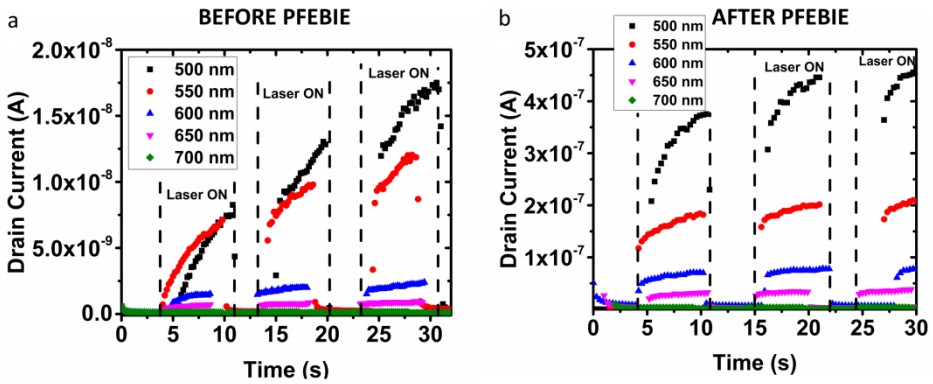

Figure 5.9: Electrical characterization of the device after PFEBIE. **a** Drain current vs drain voltage transfer characteristics. Inset corresponds with an SEM image of the tailored device. **b** Photoresponse at different excitation wavelengths.

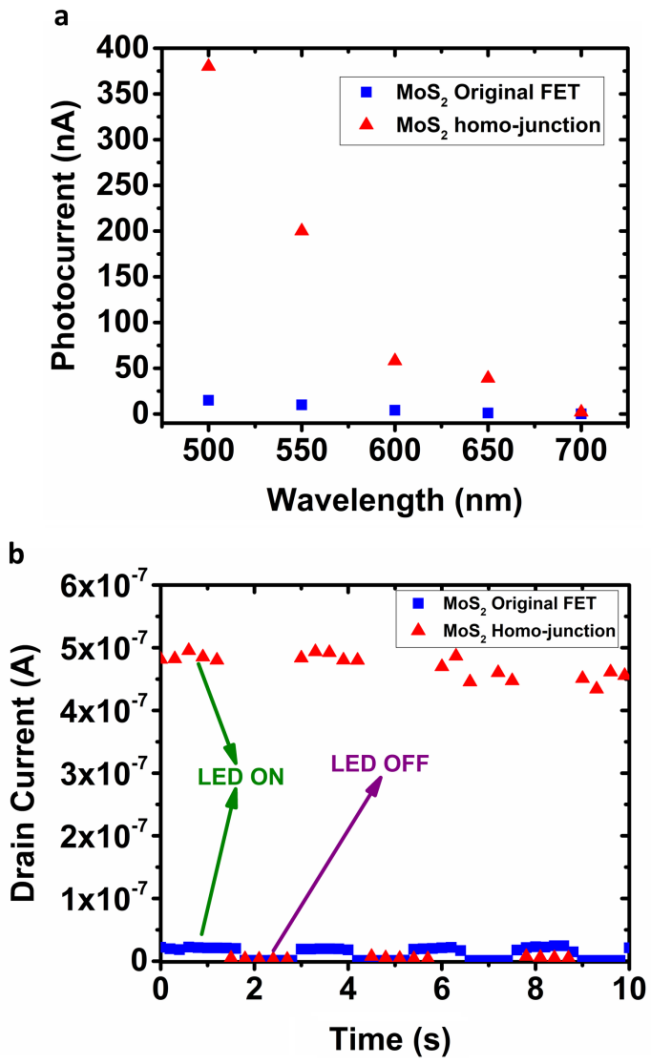

Figure 5.10: a Photocurrent as a function of the excitation wavelength for both, original MoS_2 FET and MoS_2 homo-junction. A clear tendency is identified. This photocurrent is higher if the excitation wavelength is lower. At 700 nm of excitation, the generated photocurrent is negligible because the generated current is practically zero. The generated current is higher for the MoS_2 tailored homo-junction. **b** Comparison of the photoresponse under the white LED illumination.

Figure 5.10a shows the generated photocurrent for both, the original and the tailored devices. The same trend is observed for both devices: the photocurrent decreases when the wavelength increases, as

previously reported [19]. A big difference between the initial device and the MoS_2 homo-junction is observed. The generated photocurrent is two orders of magnitude higher for the tailored device, except for wavelengths above the MoS_2 bandgap.

Figure 5.10b shows a comparison of the photoresponse under white light illumination. The spectrum of the LED is shown in Figure 5.7a. The obtained values are quite similar to the 500 nm excitation wavelength. This could be explained because the LED spectrum has a narrow peak at 460 nm. Figure 5.10b shows that, again, the generated current of the tailored device is higher. The photoresponsivity (R) is defined as the generated current as a function of the incident light power. In the case of the original MoS_2, FET R is $5x10^{-6}$ A/W. This value increases in the MoS_2 tailored homo-junction until $3x10^{-4}$ A/W, two orders of magnitude higher than in the original device. This increase in photoresponsivity is a direct consequence of the increase in the generated current after the tailoring, and it agrees with the photocurrent measurements shown in Figures 5.9 and 5.10.

5.3 Conclusions

In this chapter, PFEBIE has been proved to be a technique that allows fabricating MoS_2 based homo-junctions from MoS_2 FETs. The scissoring of half a channel induces a change in doping in one part of the device, while the other part remains as before the etching process. This change in the channel allows assembling a lateral homo-junction.

Raman spectroscopy shows that after the patterning the chemical composition remains intact.

Electrical characterization of the devices before and after the patterning confirms that PFEBIE could fabricate lateral homo-junctions. Before PFEBIE, the device behaves as a FET. After the patterning, electrical characterization shows a diode-type behavior, with the forward and reverse states at high values. These high values

are related to the creation of defects when the etching was done. The fabricated MoS_2 homo-junctions present a relatively low rectification ratio and a high ideality factor.

An optoelectronic study at cryogenic conditions was performed before and after the patterning. The photocurrent was observed to decrease when increasing the excitation wavelength due to the MoS_2 bandgap value. A comparison between before and after steps was carried out. Photocurrent in the MoS_2 lateral homo-junction was found to be higher than in the pristine device, which is in good agreement with a diode-type behavior. A study under white light illumination was also performed. The same tendency was observed, with a higher generated current in the tailored device.

Bibliography

[1] M. Riordan and L. Hoddeson, "The origins of the pn junction" *IEEE Spectrum,* vol. 34, no. 6, pp. 46-51, 1997.

[2] R. Frisenda, A. J. Molina-Mendoza, T. Mueller, A. Castellanos-Gomez, and H. S. J. van der Zant, "Atomically thin p–n junctions based on two-dimensional materials" *Chemical Society Reviews,* vol. 47, no. 9, pp. 3339-3358, 2018.

[3] M. S. Choi *et al.*, "Lateral MoS2 p–n Junction Formed by Chemical Doping for Use in High-Performance Optoelectronics" *ACS Nano,* vol. 8, no. 9, pp. 9332-9340, 2014.

[4] D. Li *et al.*, "Two-dimensional non-volatile programmable p–n junctions" Nature Nanotechnology, vol. 12, p. 901, 2017.

[5] J. Y. Lim *et al.*, "Van der Waals junction field effect transistors with both n- and p-channel transition metal dichalcogenides" npj 2D Materials and Applications, vol. 2, no. 1, p. 37, 2018.

[6] A. Nipane, D. Karmakar, N. Kaushik, S. Karande, and S. Lodha, "Few-Layer MoS2 p-Type Devices Enabled by Selective Doping Using Low Energy Phosphorus Implantation" *ACS Nano,* vol. 10, no. 2, pp. 2128-2137, 2016.

[7] B. Chakraborty, A. Bera, D. V. S. Muthu, S. Bhowmick, U. V. Waghmare, and A. K. Sood, "Symmetry-dependent phonon renormalization in monolayer MoS2 transistor," *Physical Review B,* vol. 85, no. 16, p. 161403, 2012.

[8] K. T. Nguyen, D. Abdula, C.-L. Tsai, and M. Shim, "Temperature and Gate Voltage Dependent Raman Spectra of Single-Layer Graphene" *ACS Nano,* vol. 5, no. 6, pp. 5273-5279, 2011.

[9] F. Withers *et al.*, "Light-emitting diodes by band-structure engineering in van der Waals heterostructures" Nature Materials, vol. 14, p. 301, 2015.

[10] M. Sun, D. Xie, Y. Sun, W. Li, C. Teng, and J. Xu, "Lateral multilayer/monolayer MoS2 heterojunction for high performance photodetector applications" Scientific Reports, vol. 7, no. 1, p. 4505, 2017.

[11] M.-L. Tsai *et al.*, "Monolayer MoS2 Heterojunction Solar Cells" *ACS Nano,* vol. 8, no. 8, pp. 8317-8322, 2014.

[12] A. Ortiz-Conde, F. J. García Sánchez, J. J. Liou, A. Cerdeira, M. Estrada, and Y. Yue, "A review of recent MOSFET threshold

voltage extraction methods" *Microelectronics Reliability,* vol. 42, no. 4, pp. 583-596, 2002.

[13] H. Wang *et al.*, "Integrated Circuits Based on Bilayer MoS2 Transistors" *Nano Letters,* vol. 12, no. 9, pp. 4674-4680, 2012.

[14] F. Liu *et al.*, "Van der Waals p–n Junction Based on an Organic–Inorganic Heterostructure" *Advanced Functional Materials,* vol. 25, no. 36, pp. 5865-5871, 2019/04/11 2015.

[15] J.-Y. Wu, Y. T. Chun, S. Li, T. Zhang, and D. Chu, "Electrical Rectifying and Photosensing Property of Schottky Diode Based on MoS2" *ACS Applied Materials & Interfaces,* vol. 10, no. 29, pp. 24613-24619, 2018.

[16] S. M. Sze, *Semiconductor Devices. Physics and Technology*. Wiley, 2004, pp. 428-467.

[17] Y. Sun *et al.*, "Temperature-dependent transport and hysteretic behaviors induced by interfacial states in MoS2 field-effect transistors with lead-zirconate-titanate ferroelectric gating" *Nanotechnology,* vol. 28, no. 4, p. 045204, 2016.

[18] S. Sutar, P. Agnihotri, E. Comfort, T. Taniguchi, K. Watanabe, and J. Ung Lee, "Reconfigurable p-n junction diodes and the photovoltaic effect in exfoliated MoS2 films" *Applied Physics Letters,* vol. 104, no. 12, p. 122104, 2019/06/06 2014.

[19] Z. Yin *et al.*, "Single-Layer MoS2 Phototransistors" *ACS Nano,* vol. 6, no. 1, pp. 74-80, 2012.

Conclusiones Generales

Los resultados obtenidos en esta tesis muestran la posibilidad de alterar las propiedades optoelectrónicas de dispositivos basados en disulfuro de molibdeno (MoS_2). Para ello, se ha desarrollado un método de fabricación que está basado en la interacción entre un haz de electrones y un gas atacante, que en el caso de dicha tesis es difloruro de xenon (XeF_2). Dicho método se llama Ataque Inducido por Haz de Electrones Pulsado y Focalizado (PFEBIE, en inglés).

En primer lugar, se ha optimizado la fabricación de transistores de efecto campo. Para ello, se ha desarrollado un método de litografía óptica llamado litografía correlativa de haz directo. Con esta tecnología, se pueden fabricar una gran cantidad de dispositivos en un periodo corto de tiempo. Además, el éxito de fabricación de los dispositivos es extremadamente alto.

En segundo lugar, se han estudiado cuáles son los parámetros experimentales que influyen en PFEBIE. Se ha repasado el espacio de parámetros y estudiado cómo influye cada uno de ellos, dejando constante el resto. Una vez estudiados y entendidos, se ha optimizado la fabricación de las estructuras con unos parámetros que reducen el tiempo de fabricación. Gracias al estudio de dicha técnica, se pueden fabricar grandes áreas. También es posible la fabricación de dispositivos concepto, así como alterar la geometría de dispositivos previamente fabricados y caracterizados. Con PFEBIE, se ha demostrado que un posible problema de la exfoliación mecánica (como es la variabilidad de los grosores) puede ser solucionado.

Además, en comparación con otros métodos de fabricación similares, se ha comprobado que la energía utilizada es mucho menor, disminuyendo las probabilidades de dañar la muestra. También se ha visto que los tiempos de fabricación son mucho menores. Con la

técnica propuesta en esta tésis, se puede fabricar un dispositivo cada 2 minutos.

Posteriormente, se ha investigado cuales son las consecuencias que tiene esta técnica de haz directo, PFEBIE, sobre las propiedades optoelectrónicas de transistores de efectos campo basados en MoS_2. Se ha visto, mediante caracterización eléctrica, que hay un cambio en el dopaje; yendo de dopaje tipo n hacia intrínseco o incluso tipo p. Este dopaje se ha visto en la mayoría de dispositivos fabricados y alterados con esta técnica. La hipótesis de este cambio en dopaje es la formación de vacantes de azufre cuando se realiza el ataque. Medidas espectroscópicas como Raman y fotoluminiscencia han corroborado esta hipótesis. Los parámetros Raman, como pueden ser la anchura a media altura o la diferencia de picos, varían acorde a un proceso de formación de vacantes de azufre. El cambio en fotoluminiscencia también coincide con bibliografía previa en la que se estudia cambios en el dopaje.

Por último, se ha aprovechado este cambio de dopaje para fabricar nuevos dispositivos. Se ha atacado sólo una parte del dispositivo, mientras que la otra permanece sin alterar. De este modo, la intención es poder fabricar uniones laterales que se comporten como diodos. Después de realizar la fabricación, las muestras se caracterizaron mediante medidas eléctricas en condiciones criogénicas, mostrando que el comportamiento cambia completamente. Después del ataque el dispositivo se comporta satisfactoriamente como un diodo, con una mejora en la detección de luz a distintas longitudes de onda en la parte visible del espectro electromagnético.

General Conclusions

The obtained results in this thesis show the possibility of tailoring the optoelectronic properties of MoS_2 devices. For this reason, a fabrication method has been developed. This method is based on the interaction of an electron beam and an etchant gas (XeF_2). This method is called Pulsed Focused Electron Beam Induced Etching (PFEBIE).

Firstly, the fabrication of field effect transistors has been optimized. For this porpoise, an optical lithography method has been developed. Optical correlative lithography, that allows fabricating a lot of devices in a short period of time. In addition, the fabrication yield is very high.

Secondly, the experimental parameters of PFEBIE have been studied. The parameter space of PFEBIE has been explored. Once they have been understood, the fabrication of structures was optimized, decreasing the fabrication time. Thanks to this study, it is possible to fabricate large areas. It is also possible to fabricate new proof of concept devices, as well as alter the geometry of previously fabricated and characterized MoS_2 devices. PFEBIE has also demonstrated that an apparent problem of the exfoliation (variability in the number of layers) is fixed.

In addition, a comparison between different methods was done. The used energy is much lower, decreasing the possibility of damaging the sample. The fabrication times are also much shorter. PFEBIE allows fabricating a device every 2 minutes.

Later, the consequences that PFEBIE has over the optoelectronic properties of MoS_2 FET were investigated. A change in doping, from n-type towards intrinsic or even p-type has been observed by carrying out electric characterization. This doping is present in the majority of the devices. The hypothesis of this change is the formation of sulfur

vacancies when the etching was done. Spectroscopic techniques such as Raman and photoluminescence corroborated the hypothesis. The full width at half maximum and the peak position difference varied according to a sulfur vacancy formation process. The change in photoluminescence also coincides with previous studies related to changes in doping.

Finally, the change in doping has been used to fabricate new devices. Only one region of the devices was etched, while the other part remains in the same conditions. Accordingly, the intention is to fabricate lateral homo-junctions based on MoS_2. After the tailoring, samples were characterized by electrical measurements at cryogenic conditions. The performance of the devices totally changed after the patterning, showing a diode-type behavior and increasing the photodetection under different wavelengths in the visible range of the spectrum.

Future Work

A lot of different opportunities have arisen during this thesis. A deeper study on the optical properties of the devices after PFEBIE will be carried out after this thesis. For example, the electroluminescence of the MoS_2 lateral homo-junctions will be studied. One of the first objectives will be to assemble the convenient experimental set-up and implement it to the cryostat and the spectrometer. Then more samples will be studied with an emphasis in the electro-optical properties.

PFEBIE is going to be exploited to fabricate more complex systems and circuits as an alternative to conventional silicon-based electronics. This resides on the fabrication of MOSFET and JFET circuits made by an array of 2D devices and tailoring them with PFEBIE. Another possibility is to exploit PFEBIE for fabricating two-dimensional photonic crystals based on MoS_2. This is related to the large refractive index that MoS_2 presents. With that in mind, it is necessary to fabricate a cavity on the substrate and then, exfoliate flakes on top of it. After that, different MoS_2 lattices can be fabricated with PFEBIE. In addition to these lattices, different defects can be introduced to trap light or even to guide it like in studied light guides.

Appendix A: Transport Measurements on Tailored Devices

This appendix will show the electric characterization of some of the devices presented in Chapter 4. As mentioned in this Chapter, a change in the threshold voltage was observed due to a change in the doping. This transition has been explained as a consequence of the creation of sulfur vacancies when the etching was done.

Figure A.1 corresponds with the device number 6 of Figure 4.7b. Figure A.1 shows the transfer characteristics of the device before and after the patterning.

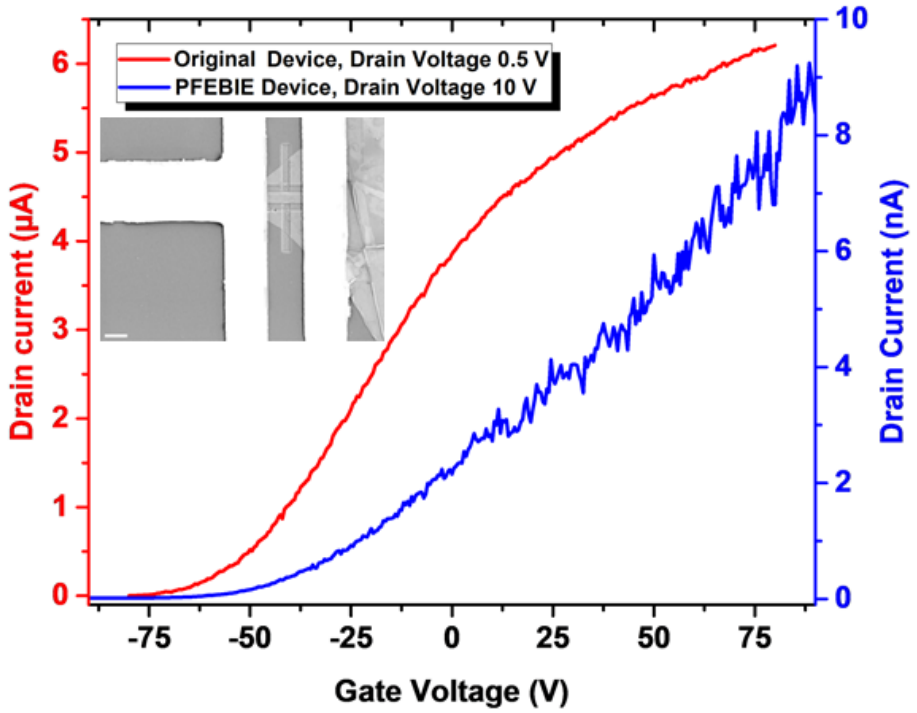

Figure A.1: RT transfer characteristics of the MoS_2 FET number 6, shown in Figure 4.7b before (red) and after (blue) PFEBIE. V_{th} varies from -70 V to -30 V.

The mobility of the original device is 18.2 cm2 V -1 s -1. After PFEBIE, this saturation region is not observed. Despite of this, the mobility can be approximately calculated in the expected linear region, resulting in 6.4 x10-3 cm2 V -1 s -1. It was dramatically reduced, maybe due to the creation of defects when the etching was performed. The intrinsic device shows a ON/OFF ratio of 10^5. The ON/OFF ratio after PFEBIE is unknown because the saturation region is above the gate voltage measuring range.

Figures A.2 and A.3 correspond with the electric characterization of two different devices before and after PFEBIE. Figure A.2 represent the transfer characteristic of the device number 4, shown in Figure 4.7b. As in the majority of the cases, the threshold voltage suffers a variation to less negative values. V_{th} goes from -70 V to -20 V, indicating a change in the doping.

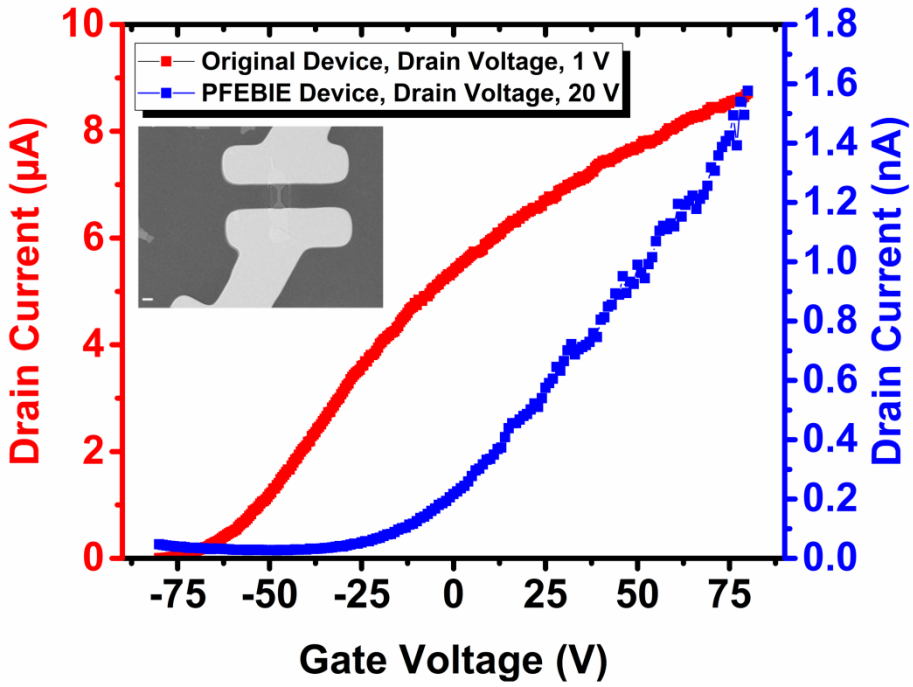

Figure A.2: RT transfer characteristics of the MoS_2 FET number 4, shown in Figure 4.7b. The red curve corresponds with the original device, while the blue curve corresponds with the tailored device. V_{th} varies from -70 V to -20 V.

Figure A.3 corresponds with the electric characterization of a device that has not been presented in this thesis. The same behavior is also observed, with V_{th} going from -100 V to 0 V.

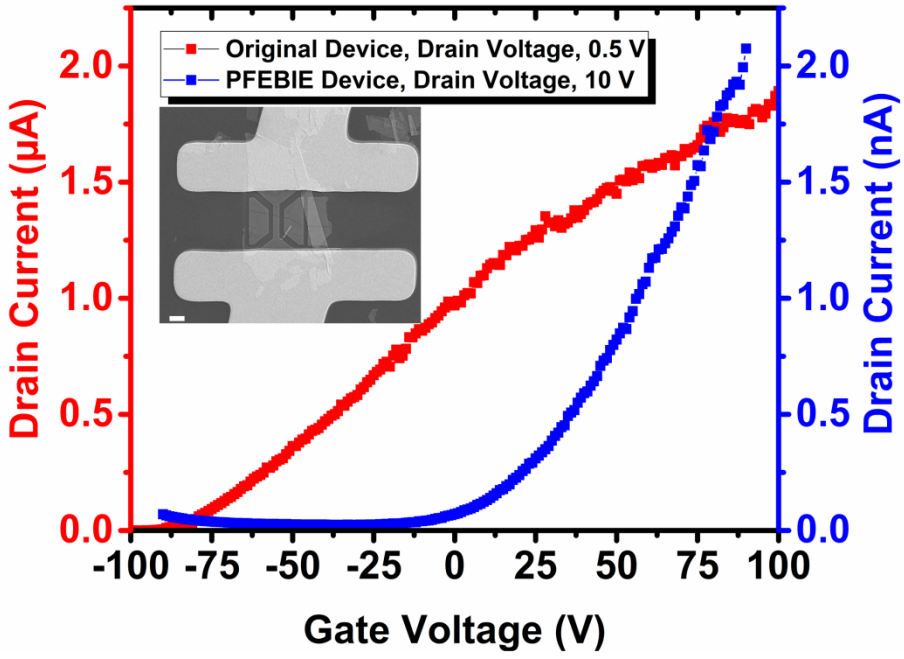

Figure A.3: RT transfer characteristics of a MoS_2 FET before (red) and after (blue) PFEBIE. As described in chapter 4, a change in the doping is observed. V_{th} varies from -100 V to 0 V.